Mass and momentum transfer upon flow through solid sponges

zur Erlangung des akademischen Grades eines
DOKTORS DER INGENIEURWISSENSCHAFTEN (Dr.-Ing.)

der Fakultät für Chemieingenieurwesen und Verfahrenstechnik der
Universität Fridericiana Karlsruhe (TH)

genehmigte
DISSERTATION

von
Dipl.-Ing. Gerardo Incera Garrido
aus Mexiko Stadt, Mexiko

Referent: Prof. Dr. Bettina Kraushaar-Czarnetzki
Korreferent: Prof. Dr.-Ing. Michael Türk
Tag der mündlichen Prüfung: 14 November 2008

Die vorliegende Arbeit entstand in den Jahren 2005 bis 2008 am Institut für Chemische Verfahrenstechnik der Universität Karlsruhe (TH).

Mein besonderer Dank gilt Frau Prof. Dr. Bettina Kraushaar und Frau Dr.-Ing. Florina Corina Patcas für die Überlassung des Themas und für die Betreuung der Arbeit. Ihre ständige Bereitschaft zur Diskussion sowie die wertvollen Ratschläge und Anmerkungen haben mir beim Erreichen meines Zieles ständig weitergeholfen und motiviert. Die gewährte wissenschaftliche Freiheit von beiden Seiten bei der Gestaltung und zeitlichen Einteilung meiner Arbeit haben wesentlich zum Erfolg beigetragen.

Herrn Prof. Dr.-Ing. Michael Türk danke ich sehr für die freundliche Übernahme des Korreferats, die ständige wissenschaftliche Unterstützung im thermodynamischen Teil meiner Arbeit und die kritische Durchsicht des Manuskripts.

Herrn Dr.-Ing. Andreas Reitzmann gilt mein Dank für die viele ideenbringende Diskussionen, zu denen er jederzeit bereit war.

Meinen herzlichen Dank möchte ich allen studentischen Mitarbeitern aussprechen, die durch ihre tatkräftige und engagierte Mitarbeit im Rahmen ihrer Diplom- und Studienarbeiten oder wissenschaftliche Hilfskraft wesentliche Beiträge zum Gelingen dieser Arbeit leisteten. In zeitlicher Reihenfolge waren dies: Carrie Street, Beatriz González, Tristan Gund, Sebastian Lang, Gabriela Todorov und Helen Sutejda.

Alle Mitarbeitern am Institut für Chemische Verfahrenstechnik danke ich für die gute Zusammenarbeit und für die stets angenehme und freundschaftliche Arbeitsatmosphäre. Besonders bei Oliver Richter, Thomas Thömmes, Anika Ritter, Jens Freiding und Gerrit Waters bedanke ich mich herzlich für die nicht nur wissenschaftliche sondern auch menschliche Unterstützung über diese, für mich sehr wertvollen Jahren.

Ich will mich auch sehr bei allen Kollegen der Forschergruppe FOR 583 für die vielen Diskussionen zum Thema Schwämmen, sowie für die Hilfe bei Messungen oder Datenvergleiche, die mir sehr viel weitergeholfen haben, bedanken.

Dr. Thomas Hahn möchte ich auch an dieser Stelle sehr danken, denn dank seinem wichtigen Hinweis bezüglich eines Anlagenproblems, konnte ich meine Arbeit viel schneller und effektiver durchführen.

Zu Letzt danke ich meine Freunde in Karlsruhe, Patrick, Hermann, Joachim, Tristan, Franz, Nicolás, Rodrigo, Yonathan, Helmut und Tatiana, die für mich in den acht Jahren in Deutschland wie eine Familie waren und immer sein werden. Ihre währende Unterstützung und Freundschaft haben mich sowohl in meiner Arbeit, als auch als Mensch sehr weitergeholfen.

Para mi Madre y mi Padre

Contents

1 Introduction

1.1 Background

Open cell ceramic and metallic sponges are highly porous monolithic reticulated materials having fascinating properties. They exhibit a continuous open cell structure formed by interconnected struts. Struts and cells build two continuous (solid and void) phases which penetrate each other. The mostly used geometric characteristic for foams and sponges is the number of pores per linear inch (PPI value). In the literature, the term “foam” is more often used to describe open celled sponges as well. However, foams are by definition materials formed by trapping gas bubbles in a liquid or solid, having usually a closed cell structure. The term “sponge” is unambiguous and describes appropriately the structures analyzed in this work. Closed cell foams have only one continuous phase, namely the solid. The void fraction of closed cell foams is dispersed among the solid structure leading to considerably different properties in comparison to the sponges. Cell size, morphology and interconnectivity are the main factors influencing the potential application of porous ceramics. Closed cell foams are used for thermal insulation, while open cell sponges are required for processes involving fluid transport like filters or catalysts. The various routes for processing macroporous ceramics can be classified into three methods [1]:

- Sacrificial template method (Figure 1.1 – A)
- Direct foaming (Figure 1.1 – B)
- Replication technique (Figure 1.1 – C and D)

The process route has a decisive influence on the properties of the porous material. The selection of one of the routes depends on the application aimed at.

The sacrificial template technique consists of the preparation of a two phase composite from a continuous ceramic precursor and a dispersed sacrificial phase that is homogeneously distributed in the precursor matrix and is then extracted to create a porous material being the negative replica of the sacrificial template. Even though this method is very flexible, yielding porosities and pore sizes raging from 20 % to 90 % and 1 – 700 µm, respectively, the main drawback of this method is the difficult removal of the sacrificial phase by pyrolysis, evaporation or sublimation at slow rates in order to avoid the collapse of the cellular structure.

In direct foaming methods, air or a gas formed by in situ reaction is incorporated into a ceramic suspension, which is subsequently set in order to keep the structure of the air bubbles and achieving by this a porous material. The porosity is proportional to the amount of gas incorporated into the liquid medium. Due to their high gas-liquid interfacial area, liquid foams are thermodynamically unstable, increasing often the size of the incorporated bubbles, leading to undesired inhomogeneities in the structure. The most critical issue upon using this method is the stabilization of the air bubbles in the suspension. Foams prepared by this method exhibit average pore sizes between 10 µm and 1.2 mm. A detailed description of this method has been given by Studart et al. [1].

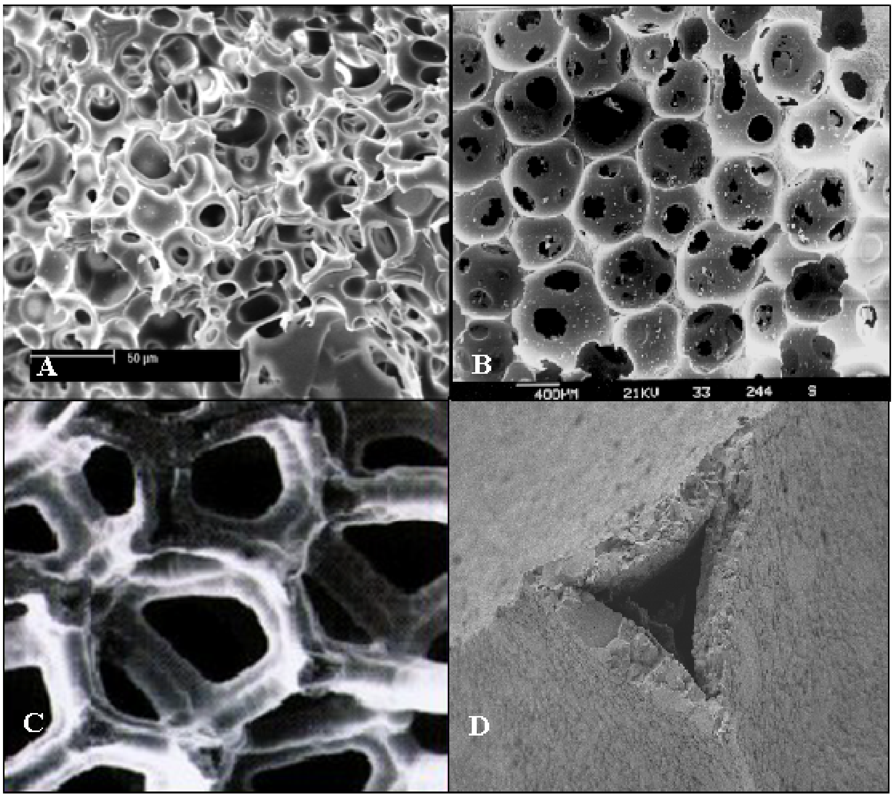

Figure 1.1: Porous structure of foams and sponges manufactured via different methods; sacrificial template (A), direct foaming (B) and replication (C); hollow strut of a replica sponge (D).

The simplest and most flexible method for the production of macroporous ceramics is the replication method. It was invented in 1961 and patented in 1963 by Schwarzwalder and Somers [2]. The principal steps in the process of the invention are the immersion of an open cell sponge in a ceramic slurry, the removal of excess slurry from the sponge, the evaporation of the volatile slurry contents and at last the sintering of the ceramic coating at temperatures from 1100°C to 1700°C, depending on the material. The organic sponge template can be natural or synthetic. The replication technique is the most popular method for the manufacturing of macroporous ceramics and is extensively used in industry for the production of ceramic filters for molten metals in foundry casting processes [3,4,5]. The polymeric sponge typically used is highly porous polyurethane. This precursor can be soaked into ceramic suspensions with a great variety in chemical composition [1,6], as long as the ceramic can be dispersed into a suspension. A disadvantage of this method is the hollow structure of the struts from the pyrolysis of the polymeric sponge, leading to a lower mechanical strength. Nevertheless, the high interconnectivity of the pores achieved by this method enhances the permeability of fluids through the structure making sponges from the replication method especially suitable for high throughput processes. Sponges obtained with the replication technique can reach total porosities between 40 and 95 % and a wide range of pore sizes between 200 µm and 3 mm.

These open cell structures have gained great interest in the last decade due to their potential applications in various processes. Their properties such as low pressure drop, high surface area enhancing mass transport, as well as the radial mixing in the tortuous structure, improving heat transfer in highly endothermic and exothermic reactions, make them attractive in many research fields. They have already been tested in various applications such as waste and exhaust gas purification [7,8,9], methane and propane combustion [10,11], carbon dioxide reforming [12], partial oxidation of hydrocarbons at short contact times [13,14], preferential oxidation of carbon monoxide in hydrogen (PROX) [15,16,17] and Fischer-Tropsch-synthesis [18]. Most of these applications involve high flow rates and/or high reaction rates, typically controlled by external mass and heat transfer. The large amount of reports on the application of ceramic sponges in important reactions can be divided in two important categories: reports using sponges due to their high permeability at high flow rates, allowing short contact times during consecutive reactions, yielding higher selectivities towards desired intermediates, and reports that deal with heat transfer limitations. A typical and important example dealing with both problems is the steam reforming of natural gas and light hydrocarbons to synthesis gas. This diffusion limited reaction operating at temperatures up to 1000°C is strongly endothermic. The necessary heat transfer into the reaction zone is achieved by a bundle of pipes having small diameters, which are filled with catalyst pellets. To overcome the high pressure drop, the pellet size is increased, lowering the effectiveness of the reactor. Twigg and Richardson [19] report on beneficial effects of foam catalysts having comparable size and surface area to conventional catalyst supports showing increased heat transfer (10 %) and lower pressure drop (25 %). The authors conclude: "It is clear that ceramic foam supports are superior for reactions with high activity and low effectiveness factors". The production of CO free hydrogen for fuel cell gas has gained great importance in recent years, since reducing the dependence on fossil fuels and reducing pollution and greenhouse gas emissions have necessarily become major challenges for future energy supply worldwide. In situ generation of hydrogen from liquid sources at ambient conditions is preferred for mobile fuel cell systems. Methanol and ethanol have been suggested for the on-board catalytic production of hydrogen [20]. A structure comparison for the production of hydrogen for fuel cells from Ru based catalysts has been reported by Liguras et al. [21]. Herein, a series of Ru catalysts supported on cordierite monoliths (automotive catalyst), ceramic sponges (ZrO_2-Al_2O_3) and γ-Al_2O_3-pellets were prepared and tested for the production of H_2 by steam reforming of ethanol. Having similar geometrical surfaces and at comparable space velocities, the sponges displayed the best performance (highest activity, high H_2- and

CO_2-selectivity with the lowest yield of undesired byproducts such as methane, acetaldehyde and CO), making them the preferred candidates for this process.

Even though ceramic sponges show advantageous properties that could be exploited in industrial applications, there is still no full scale use of these structures. In the automotive industry, ceramic sponge catalysts have not yet replaced traditional catalysts. The main factors hindering the introduction of sponge-based auto catalysts are [22]:

a. Cordierite honeycomb monolith technology is a well established technique since the mid 1970’s, whereas the first attempts for introducing sponge based auto catalysts having high activities did not come until the early 1980’s.

b. The manufacturing process of sponges is still under development, since the strength and durability as well as the provision of an outer solid skin enabling canning procedure need improvement.

c. Sponges with comparable dimensions as a honeycomb structure have a higher pressure drop.

Furthermore, in order to introduce ceramic sponges as a mass produced catalyst in the process chemical industry, where they show advantageous performance as described above, the cost of manufacturing sponge pieces must be in the range of conventional catalyst pellets. Until now, the costs are higher mostly due to the not fully developed automation of the manufacturing process. The loading into the reactor also is still problematic, since avoiding fluid bypassing without hindering heat transfer to the wall is difficult to achieve. As described previously, a solid outer skin could partially solve the problem and some manufacturers are already producing sponge pieces with a continuous protective ceramic outer skin [23].

Before reticulated porous ceramics can replace some traditional catalysts and other large-scale used structures in the industry, development of knowledge is needed. Mass (and heat) transfer as well as the permeability of open cell sponges are extremely important features which have to be studied consistently in order to correlate the morphological characteristics of different sponges to their momentum, heat and mass transfer properties, allowing for industrial implementation and reactor modelling.

The pressure drop in sponges with different geometric properties has been studied by various authors [24 - 30]. Even though the permeabilities reported follow in all cases, as expected, the Forchheimer equation for flow through porous materials, the variation in the values for the pressure drop vary widely depending on the author. This even holds for sponges with apparently similar PPI values. Due to the reticulated nature of these materials, considerable variations in the sponge structure can arise depending on the manufacturer, the polymeric precursor used and the ceramic or metallic slip applied. For these reasons, no general mathematical relation between the momentum transfer and the hydrodynamic properties of sponges has been given, yet.

Convective and radiative heat transfer coefficients of sponges with a great variety of pore densities and materials have been reported by various authors mostly on the basis of dimensionless (Nusselt, Reynolds and Prandtl) numbers [26,27,31 - 33]. Most of the authors found a strong dependence of experimental Nusselt numbers on sponge geometry at constant hydrodynamic conditions, with Nu increasing with the diameter of the pores. Since different sponge geometries result in different Nu-Re-relations, no general correlation between heat transfer- and hydrodynamic properties of these geometric similar structures has yet been achieved.

1.2 Scope and Outline of this Work

Mass transfer studies until now are rather scarce and incomplete. Richardson et al. [34] reported the mass and heat transfer properties of one ceramic sponge with a cell density of 30-PPI. Since no variation in the geometric properties of the structure was done by the authors, no general statement about the influence of the sponge geometry on the mass or heat transfer coefficients can be given. Tronconi and co-workers [35] studied mass transfer properties of four sponges (three metallic and one ceramic) as well, proposing a first correlation for the prediction of mass transfer coefficients in open celled sponges. Nevertheless, the pore density and Reynolds range varied merely between 8 - 15 PPI and 15 - 200 respectively, and making a general conclusion from the measurement of 4 sponges from different materials is rather adventurous. It is therefore an important objective to develop a suitable method for measuring and correlating mass transfer and pressure drop properties of these porous geometric structures to their hydrodynamic behaviour.

The first and most important goal of this thesis was to analyze mass transfer phenomena from the gas phase to the outer surface of porous ceramic sponges having different porosities and pore densities in a wide hydrodynamic range. To achieve this aim, the oxidation of carbon monoxide was chosen as a tool reaction in the temperature regime, where external mass transfer is the rate limiting mechanism. The first step was to develop a highly active catalytic system suitable for washcoating on the sponge carrier, without significant changes in the support’s geometric features. Previous investigations in this institute (Chemical Process Engineering, CVT) showed that dispersed platinum on tin dioxide has a considerable activity for this reaction as a result of the synergy between Pt and SnO_2, reaching mass transfer control at moderate temperatures [36]. Two different preparation methods for the deposition of Pt on SnO_2 coated sponges, one from an aqueous solution and one from a supercritical solution in CO_2 are evaluated and discussed in Chapter 2, with respect to the achieved dispersion of the noble metal on the metal oxide, the resulting activity towards CO oxidation and the optimum preparation method.

Before mass transfer and pressure drop of sponges were analyzed, a detailed morphological characterization of all structures used had to be performed. Chapter 3 deals with three adequate methods for measuring the main structural parameters of sponges: strut and total porosity, mean pore and strut diameters and geometric surface area. This chapter emphasizes the stringent importance of the knowledge of these geometric features and their deviations for the study of fluid flow through sponges. The morphological characterization is also performed on known structured catalysts, honeycomb monoliths and bead packings in order to validate the experimental mass transfer analysis method and for performance comparison of all structures.

Finally, the results of a careful study of mass transfer and pressure drop in various ceramic (and one metallic) sponges are presented in Chapter 4. Sponges with three different porosities and four pore densities are evaluated in a plug flow system with external recycle, allowing for the variation of fluid velocity in the reactor tube in a wide hydrodynamic range, at constant gas hourly space velocity (GHSV). For method validation and structure comparison, mass transfer and permeability of well studied structures, a honeycomb monolith and beads with different diameters, are analyzed using the same experimental method. Taking into account the morphology, a dimensionless analysis is performed, yielding a general relation between the mass transfer and the hydrodynamic properties of sponges with different geometric features. By using the Colburn analogy between mass and heat transfer [37]:

$$\frac{\mathrm{Sh}}{\mathrm{Re}\cdot\mathrm{Sc}^{1/3}}=\frac{\mathrm{Nu}}{\mathrm{Re}\cdot\mathrm{Pr}^{1/3}}, \tag{1.1}$$

the dimensionless mass transfer coefficients from this work are compared to the mass and heat transfer data from the literature quoted above. Furthermore, the applicability of the Lévêque analogy [38,39] (eq. 1.2) between mass (and heat) transfer and pressure drop is verified and a correlation is given for the prediction of mass transfer coefficients of sponges from experimentally more accessible pressure drop measurements.

$$\frac{\mathrm{Nu}}{\mathrm{Pr}^{1/3}}=\frac{\mathrm{Sh}}{\mathrm{Sc}^{1/3}}=0.404\cdot\left(2x_f\cdot\mathrm{Hg}\cdot\frac{D_h}{L}\right)^{1/3} \tag{1.2}$$

References

[1] A. R. Studart, U. T. Gonzenbach, E. Tervoort, L. J. Gauckler, *Processing routes to macroporous ceramics: a review*, J. Am. Ceram. Soc. 89 (2006) 1771-1789.

[2] K. Schwartzwalder, A.V. Somers, *Method of making porous ceramic articles,* US Patent 3090094 (1963).

[3] E. Wiese, *Filtration von großen und schweren GJL und GJS Metallgussteilen,* Informationsschrift, Foseco GmbH, www.foseco.de

[4] M. V. Twigg, J. T. Richardson, *Theory and application of ceramic foam catalysts*, Chem. Eng. Res. Des., IChemE Trans. A 80 (2002) 183-189.

[5] L. J. Gauckler, M. M. Waeber, C. Conti, M. Jacob-Duliere, *Ceramic foam for molten-metal filtration*, J. Metals 37 (1985) 47 – 50.

[6] J. Saggio-Woyansky, C. E. Scott, W.P. Minnear, *Processing of porous ceramics*, Am. Ceram. Soc. Bull. 71 (1992) 1674 – 1682.

[7] A. N. Pestryakov, E. N. Yurchenko, A. E. Feofilov, *Foam-metal catalysts for purification of waste gases and neutralization of automotive emissions*, Catal. Today 29 (1996) 67 – 70.

[8] D. Fino, N. Russo, G. Saracco, V. Specchia, *Multifunctional filter for treatment of the flue gases from municipal waste incinerators*, Ind. Eng. Chem. Res. 44 (2005) 9542 – 9548.

[9] B. A. A. L. van Setten, C. G. M. Spitters, J. Bremmer, A. M. M. Mulders, M. Makkee, J. A. Moulijn, *Stability of catalytic foam diesel-soot filters based on* Cs_2O*,* MoO_3*, and* Cs_2SO_4 *molten-salt catalysts,* Appl. Catal. B: Environmental 42 (2003) 337 – 347.

[10] I. Cerri, G. Sarraco, V. Specchia, *Methane combustion over low-emission catalytic foam burners*. Catal. Today 60 (2000) 21 – 32.

[11] A. Schlegel, S. Buser, P. Benz, H. Bockhorn, F. Mauss, NO_x *formation in lean premixed noncatalytic and catalytically stabilized combustion of propane*, Twenty-Fifth Symposium on Combustion/The Combustion Institute (1994) 1019 – 1026.

[12] J. T. Richardson, M. Garrait, J.-K. Hung, *Carbon dioxide reforming with Rh and Pt-Re catalysts dispersed on ceramic foam supports,* Appl. Catal. A: General 255 (2003) 69 – 82.

[13] K. A. Williams, L. D. Schmidt, *Catalytic autoignition of higher alkane partial oxidation on Rh-coated foams*, Appl. Catal. A: General 299 (2006) 30 – 45.

[14] G. J. Panuccio, K. A. Williams, L. D. Schmidt, *Contributions of heterogeneous and homogeneous chemistry in the catalytic partial oxidation of octane isomers and mixtures on rhodium coated foams*, Chem. Eng. Sci. 61 (2006) 4207 – 4219.

[15] A. Sirijaruphan, J. G. Goodwin Jr., R. W. Rice, D. Wei, K. R. Butcher, G. W. Roberts, J. J. Spivey, *Metal foam supported Pt catalysts for the selective oxidation of CO in hydrogen*, Appl. Catal. A: General 281 (2005) 1 – 9.

[16] A. Jhalani, L. D. Schmidt, *Preferential CO oxidation in the presence of* H_2*,* H_2O *and* CO_2 *at short contact-times*, Catal. Lett. 104 (2005) 3 – 4.

[17] A. Wörner, C. Friedrich, R. Tamme, *Development of a novel Ru-based catalyst system fort he selective oxidation of CO in hydrogen rich gas mixtures*, Appl. Catal. A: General 245 (2003) 1 – 14.

[18] Y.-h. Chin, J. Hu, C. Cao, Y. Gao, Y. Wang, *Preparation of a novel structured catalyst based on aligned carbon nanotube arrays for a microchannel Fischer-Tropsch synthesis reactor*, Catal. Today 110 (2005) 47 – 52.

[19] M.V. Twigg, J.T. Richardson, *Preparation and properties of ceramic foam catalyst supports*, in: G. Poncelet, J. Martens, B. Delmon, P.A. Jacobs, P. Grange (Eds.), “Preparation of catalysts IV: Scientific Bases for the Preparation of Heterogeneous Catalysts”, Elsevier, Amsterdam (1995) 345 – 359.

[20] F. Scheffler et al., *Heterogeneously catalyzed processes with porous cellular ceramic monoliths*, in M. Scheffler and P. Colombo (Eds.), “Cellular Ceramics; Structure, Manufacturing, Properties and Applications”, Wiley, Weinheim (2005) 454 – 483.

[21] D. K. Liguras, K. Goundani, X. E. Verykios, *Production of hydrogen for fuel cell by catalytic partial oxidation of ethanol over structured Ru catalysts*, Int. J. Hydrogen Energy 29 (2004) 419 – 427.

[22] M. Twigg, J. T. Richardson, *Fundamentals and applications of structured ceramic foam catalysts*, Ind. Eng. Chem. Res. 46 (2007) 4166 – 4177.

[23] www.vesuvius.com

[24] J.G. Fourie, J.P Du Plessis, *Pressure drop modelling in cellular metallic foams*, Chem. Eng. Sci. 57 (2002) 2781 – 2789.

[25] J. T. Richardson, Y. Peng, D. Remue, *Properties of ceramic foam catalyst supports: pressure drop*, Appl. Catal. A: General 204 (2000) 19-32.

[26] S. Decker, F. Durst, D. Trimis, S. Nemoda, V. Stamatov, M. Steven, M. Becker, T. Fendt, B. Hoffschmidt, O. Reutter, *Thermisch beaufschlagte Porenkörper und deren Durchströmungs- und Wärmeübertragungseigenschaften*, Abschlussbericht DFG Projekt DU 101/55-1 (2002).

[27] A. Schlegel, P. Benz, S. Buser, *Wärmeübertragung und Druckabfall in keramischen Schaumstrukturen bei erzwungener Strömung*, Wärme- und Stoffübertragung 28 (1993) 259 – 266.

[28] L. Giani, G. Groppi, E. Tronconi, *Mass-transfer characterization of metallic foams as supports for structured catalysts*, Ind. Eng. Chem. Res. 44 (2005) 4993-5002.

[29] E. A. Moreira, M. D. M. Innocentini, J. R. Coury, *Permeability of ceramic foams to compressible and incompressible flow*, J. Eur. Ceram. Soc. 24 (2004) 3209 – 3218.

[30] M. Lacroix, P. Nguyen, D. Schweich, C. P. Huu, S. Savin-Poncet, D. Edouard, *Pressure drop measurements and modelling on SiC foams*, Chem. Eng. Sci. 62 (2007) 3259 – 3267.

[31] Y. Peng, J. T. Richardson, *Properties of ceramic foam catalyst supports: one-dimensional and two-dimensional heat transfer correlations*, Appl. Catal. A: General 266 (2004) 235 – 244.

[32] L. B. Younis, R. Viskanta, *Experimental determination of the volumetric heat transfer coefficient between stream of air and ceramic foam*, Int. J. Heat Mass Transfer 36 (1993) 1425-1434.

[33] T. J. Lu, H. A. Stone, M. F. Ashby, *Heat transfer in open-cell metal foams*, Acta Mater. 46 (1998) 3619 – 3635.

[34] J. T. Richardson, D. Remue, J. K. Hung, *Properties of ceramic foam catalyst supports: mass and heat transfer*, Appl. Catal. A: General 250 (2003) 319-329.

[35] G. Groppi, L. Giani, E. Tronconi, *Generalized correlation for gas/solid mass-transfer coefficients in metallic and ceramic foams*, Ind. Eng. Chem. Res. 46 (2007) 3955 – 3958.

[36] K. Grass, H.-G. Lintz, *The kinetic of carbon monoxide oxidation on tin (IV) oxide supported Pt catalysts*, J. Catal. 172 (1997) 446 – 452.

[37] T. H. Chilton, A. P. Colburn, *Mass transfer (absorption) coefficients: prediction from data on heat transfer and fluid friction*, Ind. Eng. Chem. 26 (1934) 1183 – 1187.

[38] A. Lévêque, *Les lois de la transmission de chaleur par convection*, Ann. Mines 13 (1928) pp. 201 – 299, 305 – 362, 381 – 415.

[39] H. Martin, *The generalized Lévêque equation and its practical use for the prediction of heat and mass transfer rates from pressure drop*, Chem. Eng. Sci. 57 (2002) 3217 – 3223.

2 Preparation of sponge-supported Pt/SnO_2 catalysts and their performance in the oxidation of CO

2.1 Introduction

The oxidation of carbon monoxide on platinum metals has been a favoured test reaction in fundamental surface science and kinetic studies and has been widely investigated for more than a century. Starting with Langmuir in 1921 [1] a multitude of studies under vacuum conditions has revealed mechanistic details and fundamental knowledge [2].

A second group of investigations at total pressures about one bar, mainly on supported catalysts, aimed at the quantitative description of the reacting system as a function of temperature, concentration and catalyst structure.

In both domains, roughly the same reaction pattern is shown [3-5]. In an oxidative atmosphere, the reaction is first order with respect to carbon monoxide and attains zero or negative order (depending on the temperature) as soon as CO is in excess.

On the other hand, the catalytic oxidation of carbon monoxide also represents an important step downstream to, e. g. reforming and combustion processes. In the context of fuel cell technology, in particular, CO removal gained increasing importance since the catalysts of the low-temperature fuel cells are extremely sensitive to poisoning by CO. In this application, the concentration of carbon monoxide needs to be reduced from about 1 % to below 10 ppm in the presence of excess hydrogen. The preferential oxidation of CO (PROX) to CO_2 with a minimum H_2 consumption is a good option for this purpose. However, it must be carried out at low to moderate temperatures to avoid the occurrence of the reverse water-gas-shift-reaction from CO_2 and H_2 to CO and H_2O which is favoured at higher temperatures [6]. Highly active catalysts are needed to reach this goal.

2.1.1 Conventional preparation

For increased activity towards the oxidation of carbon monoxide, catalysts with two components, a noble metal and a metal oxide, have shown a better overall performance than catalysts with one component, only. The choice of metal oxide support is of extreme importance for catalyst optimization. The use of an oxide featuring various oxidation states as a second component together with a noble metal has shown to improve the catalytic activity for CO oxidation, displaying zero order kinetics with respect to CO at low temperatures and/or higher CO concentrations [7,8,9]. An increased activity for CO oxidation at room temperature and below has been observed for palladium on zirconia, silicon oxide and titanium dioxide [10,11], as well as for gold supported on iron oxide, cobalt oxide and tin dioxide among others [9,12,13].

Nevertheless, the activity of oxide supported metal catalysts depends significantly on the size, morphology and dispersion of the noble metal.

One promising combination of noble metal and metal oxide that has been studied since the 1980’s is Pt on SnO_2 [7,14-17]. Even if the metal content, the SnO_2 structure and the Brunauer-Emmett-Teller (BET) surface area vary greatly depending on the author, all catalysts have one thing in common: they are active at conditions where neither Pt nor SnO_2 alone catalyze the CO oxidation. The high activity is ascribed to a synergistic mechanism in which Pt provides the adsorption sites for CO, while oxygen adsorbs dissociatively on SnO_2 [7,18]. The reaction between the adsorbed species occurs at the Pt/SnO_2 phase boundary line (Figure 2.1). If this bifunctional mechanism holds, it should be of great importance for a high catalytic activity to realize a large boundary line, i. e. to achieve highly dispersed platinum nanoparticles on the tin dioxide phase.

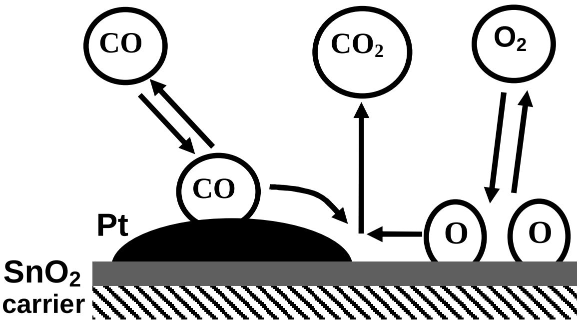

Figure 2.1: CO oxidation mechanism on Pt/SnO_2.

Previous studies at the Institute for Chemical Process Engineering of the University of Karlsruhe, based on a patent by Wright and Sampson [14] for the preparation of Pt/SnO_2 catalysts for CO oxidation at room temperature, show high activity in CO oxidation at moderate temperatures. At higher CO concentrations up to 2 %, zero order kinetics with respect to CO are observed in an oxidative atmosphere due to the bifunctional mechanism of the catalyst, in contrast to the negative kinetics observed on Pt- or Pt-alumina catalysts. The reaction rate increases with the number of platinum elements adjacent to tin dioxide elements, that is the extension of the Pt/SnO_2 borderline or Pt dispersion, consistent with the proposed mechanism shown in Figure 2.1. The experimental method consists of the preparation of a SnO_2-sol from metallic tin with a considerable BET-area of 200 m^2/g, washcoating of the alumina support, and subsequently impregnating the SnO_2-coated precursor with an aqueous platinum-tetramine-nitrate solution. This procedure was used to coat plane leaflets, allowing a homogeneous distribution of Pt on SnO_2 during drying and calcining. The applicability of this method is less obvious in case of complex geometric structures like tortuous pore networks, where impregnation with liquids tends to yield maldistributions under the effects of gravity, surface tension and capillary forces. This led to the initiative of trying an alternative method for the deposition of the noble metal on SnO_2-coated sponges, with which these disadvantageous effects could be avoided.

2.1.2 The supercritical route: thermodynamics of supercritical mixtures

A new promising method for the deposition of various metal nanoparticles onto the surface of porous solid supports is the supercritical fluid incorporation. This process involves the dissolution of an organometallic precursor in a supercritical fluid (SCF) and the exposure of a substrate to the solution. After adsorption on the substrate, the organometallic precursor can be converted into its metallic form thermally or chemically by reduction with hydrogen or with an alcohol [19]. Using a SCF as the solution medium for synthesising supported metal nanoparticles has many advantages related to the unique properties of SCFs. Their thermophysical properties are between those of gases and liquids: they offer low viscosity (η), high diffusion rates (D_{AB}) and the absence of surface tension (Table 2.1). Furthermore, these properties are tuneable by adjusting pressure and temperature, since density (ρ) and viscosity change drastically near the critical point. Densities can reach or even exceed those of liquids, making some SCFs extremely good solvents for a wide range of organometallic compounds. One of the most promising supercritical fluids for many engineering purposes is carbon dioxide. It exhibits low critical temperature and pressure values (T_c = 31 °C; p_c = 7.38 MPa), low toxicity and is chemically inert. These properties have led to the use of sc-CO_2 in various extractive processes such as the decaffeination of coffee, in chemical reactions, chromatography, drying and synthesis of nanostructured materials [20-23].

Table 2.1: Thermo-physical properties of gases, supercritical fluids and liquids [24].

	Gas: 0.1 MPa, 12 – 27 °C	**SCF**	**Liquid** : 12 – 27 °C
ρ [kg/m^3]	60-200	200-500	600-1600
D_{AB} [cm^2/s]	0.1-0.4	$0.7\cdot10^{-3}$	$(0.2\text{-}2)\cdot10^{-5}$
η [Pa s]	$(1\text{-}3)\cdot10^{-5}$	$(1\text{-}3)\cdot10^{-5}$	$(0.2\text{-}3)\cdot10^{-3}$

Supercritical incorporation not only enables the deposition of Pt nanoparticles in narrow size distributions, it also allows for the homogeneous distribution of the metal on a complex geometry without the influence of surface tension or gravity. In this work, supercritical deposition was applied to produce dispersed platinum particles on SnO_2-coated α-Al_2O_3 sponges. The deposition method is based on a patent by Watkins [25] and involves the chemical reduction of organometallic compounds in SCFs with H_2. This technology was first termed Chemical Fluid Deposition, but will be referred to herein as Supercritical Fluid Reactive Deposition (SFRD). The organic platinum complex chosen was dimethyl-(1,5-cyclooctadien)-platinum ($Pt(COD)Me_2$), due to its facilitated decomposition with H_2, the high Pt-content (58.5 %) and the low toxicity of its organic ligands [20]. In order to carry out a technical process with supercritical fluids like SFRD, the knowledge of the thermodynamic behaviour of the substances involved is of great importance. The knowledge of solid-liquid-gas (s-l-g) and solid-fluid (s-f) phase behaviour is necessary to have information about the state of the low volatile organometallic substance at a given temperature and pressure, since the properties of the particles from SFRD such as their size and morphology are often strongly influenced by the melting behaviour of the mixtures involved. For the practical applicability of supercritical deposition, the equilibrium solubility of the organometallic in CO_2 should be analyzed over a wide pressure range in order to adjust the conditions for an effective deposition from a solution which contains sufficient precursor for loading the desired amount of the metal.

2.1.2.1 Melting point depression

The s-l-g curve and solubility of the system CO_2/Pt(COD)Me_2 were analyzed in earlier works at the Institute for Technical Thermodynamics and Refrigeration (ITTK) in the University of Karlsruhe (TH). The measurement techniques and experimental procedure can be found elsewhere [26]. In Figure 2.2 the pressure-temperature data for the s-l-g-line of the binary system CO_2/Pt(COD)Me_2 are depicted.

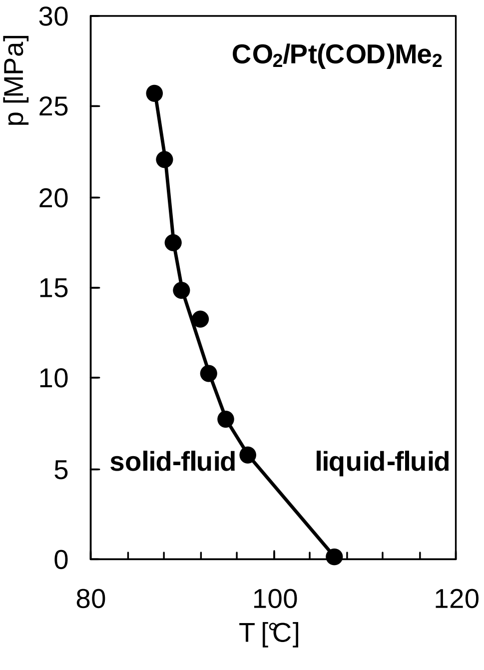

Figure 2.2: s-l-g data for CO_2/Pt(COD)Me_2 [26,27].

This binary system shows the typical behaviour of a highly asymmetric mixture, consisting of compounds being different in size, molecular structure and intermolecular interaction [28]. The high solubility of CO_2 in the liquid Pt(COD)Me_2 causes a melting point depression and a negative *dp/dT* slope of the s-l-g-line in the investigated pressure range. The melting temperature decreases from 107 °C at atmospheric pressure to 87 °C at 25.6 MPa. Hence, solid-fluid equilibrium exists for temperatures between 32 °C and 87 °C in the whole pressure range.

2.1.2.2 Solubility

The second important influencing parameter is the solubility of the organometallic in CO_2. High solubilities are advantageous, since higher metal loadings are achievable during deposition. Just above the critical temperature of the solvent, the density and consequently the solubility, increase strongly with the system pressure. At pressures above two- to threefold of the critical pressure, the influence of pressure on solubility (and density) decreases. Slightly above the critical pressure of CO_2 is the so-called crossover pressure region, where solubility decreases with increasing temperature for a certain pressure range. The influence of the decreasing density in the crossover region is stronger than the increasing vapour pressure of the low volatile substance with increasing temperature. Since high solubilities are desired for SFRD, the crossover pressure region has to be known. For the evaluated system, this region can be avoided at pressures above 15 MPa [27].

Figure 2.3 displays the influence of temperature and CO_2 density on the equilibrium solubility of the system CO_2/Pt(COD)Me_2. The isothermal dependence of solubility on solvent density can be clearly seen. At a constant density, solubility increases due to the associated increase in vapour pressure. The lines depicted in the figure are the result of the empirical correlation between the logarithm of the solubility and the logarithm of the relative fluid density [29]:

$$ln(w_2) = A + B \cdot ln\left(\frac{\rho_{CO_2}}{\rho_{crit}}\right) \tag{2.1}$$

With:

w_2 : equilibrium weight fraction of Pt(COD)Me_2 in CO_2 [$g_{\text{Pt-komplex}}/g_{\text{mixture}}$]

A, B : constants for a specific mixture at constant temperature [-]

ρ_{CO_2} : CO_2 density [g/cm^3]

ρ_{crit} : critical density [g/cm^3]

As can be seen from the figure, the data are satisfactorily correlated with the empirical correlation. The values for the constants *A* and *B* of the mixture analyzed in this work and their accuracy are given in Table 2.2.

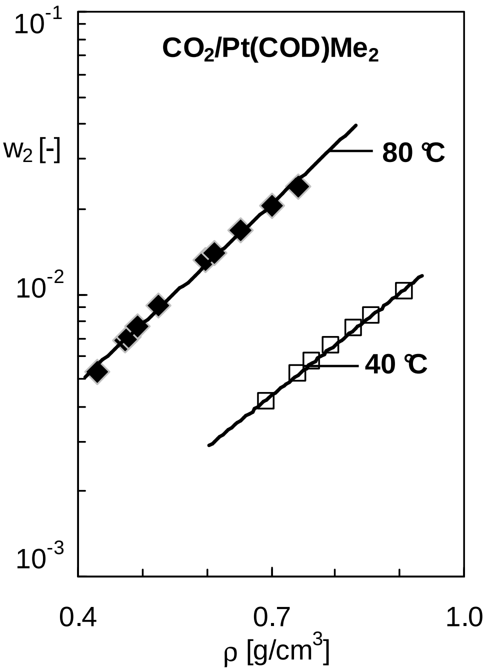

Figure 2.3: Solubility data versus CO_2 density of the system CO_2/Pt(COD)Me_2 [27]. The lines represent the empirical correlation in eq. (2.1). The density of CO_2 is taken from NIST Chemistry WebBook [24].

Table 2.2: Values for constants A and B in eq. (2.1) for the system CO_2/Pt(COD)Me_2.

T [°C]	A	B	$AARD$[1] [%]
40	-6.800	3.341	5.77
80	-5.016	2.793	6.34

[1] $AARD[\%] = \frac{100}{N} \sum_{1}^{N} \frac{\left| w_{exp} - w_{calc} \right|}{w_{exp}}$

On the basis of the previously analyzed thermodynamic behaviour of the present system, the experimental approach for the evaluation of suitable conditions for supercritical deposition of Pt will be discussed in subchapter 2.2.4.

2.2 Experimental

The supports used for the developing of the preparation method for Pt/SnO_2- structured catalysts were 45-PPI α-Al_2O_3 ceramic sponges (Vesuvius Inc.), with a porosity of 80 %. Prior to washcoating, cylindrical bodies (15 mm in diameter and 50 mm in length) were cut to thin cylinders of 3 – 6 mm thickness. After cutting, every sponge piece was washed with distilled water and acetone and calcined at 350 °C.

2.2.1 Preparation of tin dioxide sol

A tin dioxide sol was prepared for the washcoating of the alumina supports with colloidal tin dioxide as described in the specifications below [30]:

1. *Dissolution of metallic tin*: 200 ml distilled water are added to 400 ml concentrated nitric acid (65 %). Then, 200 g of granulated tin are added to the solution while mixing, so slowly so that the mixture never reaches a temperature higher than 20°C (exothermic reaction). To avoid temperature increase, the solution is cooled in an ice-bath. After adding the whole amount of tin, the mixture remains agitated until the colour of the solution is white-grey. The white colour of the solution is caused by the precipitation of the α-stannic acid, more precisely denoted as tin (IV) oxide-hydrate. Under stirring another litre of distilled water is added.
2. *Washing the stannic acid*: the precipitate of stannic acid has to be washed to obtain a stable sol. Firstly, one litre of 1-molar ammonia solution in water is added, and then the solution is agitated during 10 minutes. The solution is then left for 9 h to let the acid precipitate. Subsequently, the solution is centrifuged (15 min. at 1500 rpm) to separate the solid from the remaining liquid. The washing with ammonia solution has to be repeated until the pH of the remaining liquid is approximately 9. Once the pH of 9 is reached, the same procedure is repeated with distilled water instead of ammonia solution. Washing with distilled water has to be repeated until the conductivity of the solution after washing is smaller as 1000 mS/cm. The precipitate has then a white colour and the consistence of a gel.
3. *Bringing the precipitate into a dispersion colloid (sol)*: the precipitate is stabilized and dispersed by adding dropwise under agitation 200 ml of cyclohexylamine. The sol is then diluted with distilled water to reach a concentration of 250 g/L tin dioxide.

The fabricated sol showed good stability (> 10 months), having a conductivity of 2700 mS/cm and a pH of 10. After drying and calcining the sol for 6 hours at 80 °C and 350 °C respectively, the tin dioxide powder had a specific surface area (BET) of 110 - 120 m^2/g.

2.2.2 SnO_2 washcoating of the Al_2O_3 carrier

Sponge pieces were weighed and subsequently submerged in the SnO_2 sol under careful agitation to make sure that the sol reached the whole surface of the sponge and no air was left in the pores. After five minutes, the samples were removed and placed in a ceramic plate. The excess sol was removed carefully by a gentle flow of nitrogen to avoid the accumulation of SnO_2 in the pores between the cells of the structure. The samples were then allowed to dry over a polymeric sponge and rotated every 15 minutes for the first two hours and every 30 minutes during the remaining 6 hours, to ensure a homogeneous distribution of the tin dioxide layer along the loaded pieces. After drying for one night at room temperature, the samples were dried and calcined in air according to the following temperature program:

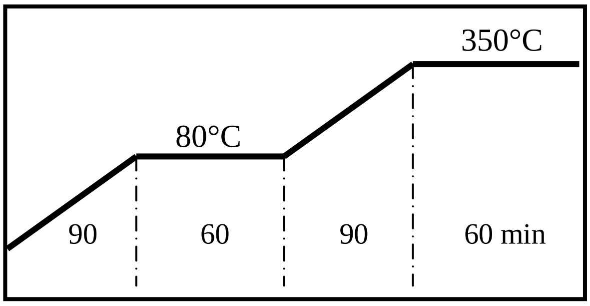

Figure 2.4: Temperature program for the drying and calcining of the SnO_2 coated catalysts.

Subsequently, every precursor piece was weighed to calculate the mass percentage of SnO_2. To ensure a complete coverage of the geometric surface of the sponges, a second loading was carried out following exactly the same procedure as described above.

2.2.3 Impregnation with an aqueous platinum solution

Following the conventional procedure described in chapter 2.1.1, 45-PPI sponges coated with tin dioxide were submerged in a 15 g/L $Pt(NH_4)_4NO_3$ aqueous solution [14], agitated gently and left for three hours. The mass ratio of platinum in the solution to SnO_2 on the support amounted to 2 – 3. They were then removed from the solution, dried at 80 °C and calcined at 350 °C in air following the procedure displayed in Figure 2.4. Prior to use, the Pt was reduced in a flow of 5 % H_2/ N_2 at 80 °C for 2 hours.

2.2.4 Supercritical Fluid Reactive Deposition (SFRD) of platinum

With the thermodynamic fundamentals analyzed before (chapter 2.1.2), three deposition conditions were chosen in order to find out the optimum conditions for the supercritical fluid reactive deposition of platinum on tin dioxide coated ceramic sponges (Table 2.3).

Table 2.3: Experimental conditions chosen for Supercritical Fluid Reactive Deposition of Pt.

SFRD	Pressure (MPa)	Temperature (° C)
1	15.5	80
2	25.0	80
3	15.5	100

SFRD 1: With the conditions set for this experiment, an equilibrium weight fraction of ($w_2 = m_{precursor}/m_{mixture}$ =) $5.93 \cdot 10^{-3}$ can be obtained, allowing for a high degree of deposition over the crossover pressure region without the appearance of a liquid phase (below the melting temperature).

SFRD 2: This deposition is performed in order to observe the influence of solubility of the organometallic in CO_2 on the properties of the catalyst. Raising the pressure from 15.5 MPa (SFRD 1) to 25 MPa results in an increase in solubility or weight fraction from $5.93 \cdot 10^{-3}$ to $1.94 \cdot 10^{-2}$ (g/g). As a consequence, the supercritical solution exhibits a considerable lower saturation ($m_{precursor}/m_{CO2}$ = constant) and, hence, the driving force for adsorption on the SnO_2-phase is reduced.

SFRD 3: To evaluate the possible influence of surface tension, experiment SFRD 3 is carried out above the melting temperature of $Pt(COD)Me_2$, where a liquid-fluid equilibrium exists. At these conditions, liquid droplets and, as a consequence, large particles can be formed due to coalescence prior to reduction, influencing the properties of the catalyst [31].

The setup used for supercritical deposition comprised a deposition vessel connected by pipes and needles valves on both sides to two screw presses for controlled filling of carbon dioxide and hydrogen under pressure (Figure 2.5). The stainless steel deposition vessel (49 cm^3) was equipped with carbon/PTFE O-rings, thermocouple, pressure transducer, rupture disk, and a ventilation line with filters to prevent loss of solid organic metal complex. Prior to each experiment, $Pt(COD)Me_2$ and 3 - 5 SnO_2-coated sponge pieces were placed into the vessel in two separate open recipients. A magnetic agitator was placed between the recipients for an enhanced mixing of the sc-solution. In all experiments, the ratio between $Pt(COD)Me_2$ and the support was kept constant at 0.024 g/g. After assembling the vessel and vacuum degassing, 5 MPa CO_2 were fed into the system. The deposition temperature was then set to avoid condensation of CO_2. Subsequently, the CO_2 pressure was slowly increased (screw press 1) until the desired sc-conditions for deposition were reached. The platinum complex started to dissolve in the carbon dioxide and to adsorb on the tin dioxide wash coat. The duration of dissolution and adsorption chosen was 20 h, which is sufficient time to reach the equilibrium state. After adsorption of the complex, 1.17 vol-% hydrogen was added to the mixture at constant temperature and pressure (screw presses 1 and 2) and kept for 2 h. During this process, the complex is reduced and its organic ligands are transformed to cyclooctane and methane. The system was then depressurized slowly to atmospheric conditions and cooled down to ambient temperature. The Pt/SnO_2-loaded sponge catalysts were removed and the average mass percentages of deposited platinum were measured gravimetrically (Mettler-Toledo) with an accuracy of ± 0.2 mg.

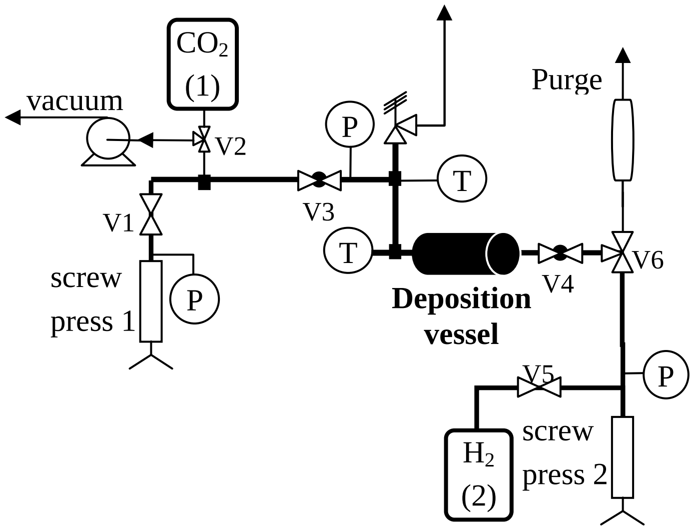

Figure 2.5: Experimental setup for the Supercritical Fluid Reactive Deposition

2.2.5 Catalyst characterization

All 45-PPI sponge catalysts, both from aqueous and supercritical deposition, were characterized with the methods described below.

Determination of the platinum content via x-ray fluorescence (XRF)

The precise platinum contents of the pieces used for catalytic activity tests were determined by means of x-ray fluorescence analysis (Spectrace 5000, 50 kV, Rh-Target). To determine the precise platinum content of each catalytic piece via x-ray fluorescence, a calibration curve was first determined with four Pt/SnO_2-standards containing a known amount of platinum. The finely milled samples were placed in the apparatus to be measured via x-ray fluorescence. Table 2.4 presents the calibration results that compare the platinum percentage of each calibration standard and the platinum percentage analyzed via x-ray fluorescence.

Table 2.4: Calibration values of the Spectrace 5000 apparatus for the measurement with XRF.

Standard	Pt-calibration [%]	Pt-XRF [%]
1	0.476	0.489
2	0.992	1.029
3	1.977	1.957
4	0.218	0.188

Scanning electron microscopy (SEM)

The layer thickness of SnO_2, the surface morphology and the distribution of elements on the carrier were investigated with SEM (LEO 1530) combined with energy dispersive x-ray (EDX) analysis. Prior to the examination of the layer thickness, the sponge samples are embedded in resin to avoid chipping of the SnO_2-layer. For the observation of the surface morphology, no additional preparation is needed.

Transmission electron microscopy (TEM)

The platinum distribution on SnO_2 (microstructure) was analyzed using a Philips-CM200-FEG TEM. The microscope is equipped with in-situ EDX spectrometer for elemental analysis. Samples for TEM are prepared by milling the catalyst followed by dispersion in acetone and deposition on a holey carbon film on a copper mesh. The platinum particle size distribution was determined from over 100 images at different locations.

2.2.6 Description of the reaction unit for CO oxidation

To investigate the CO oxidation kinetics of the prepared catalysts at different residence times, temperatures and hydrodynamic conditions, an experimental apparatus with external recycle was designed and constructed. A flow sheet of the setup is depicted in Figure 2.6. The principal component of the unit is the tubular glass reactor with a length of 250 mm. The glass reactor is surrounded by electrical heating elements (Horst; 400 W), glass wool and insulation (10 mm). The recycle system consists mainly of stainless steel tubes (Swagelok) with an inner diameter of 10 mm. The rather large diameter of the recycle pipes is necessary due to the high flow rates required for the kinetic experiments. Recycle flow is imposed by a membrane pump (KNF) with chemically inert PTFE membranes. By varying the frequency of the pump motor (frecuency regulator ABB), the recycle flow rate and the flow of the gas mixture through the reactor can be varied in the range of 5 – 200 l/min (STP) at a constant residence time. The recycle flow rate is measured by a low-Δp flow meter (M&W Instruments). Since the temperature of the effluent gas mixture from the reactor can be up to 300 °C, a cooling system prior to the pump has to be implemented to protect the membranes of the pump. This is realized by a coiled tubing (3 m long) connected to the recycle system, which is immerged in a mixture of water and ethylene glycol (30 vol.-%) cooled by a cryostat (HAAKE K20). This setup enabled cooling of the gas mixture in the coil down to 10 °C before entering the pump. Synthetic air and a mixture of 25 % CO in N_2 (Messer-Griesheim) are fed to the unit by Brooks mass flow controllers. Before entering the reaction unit, the CO/N_2 mixture has to pass the so called carbonyl-reactor, filled with quartz pellets and heated at 300 °C, to purify it from the ferrous carbonyls $Fe_x(CO)_y$ stemming from the steel bottle. After mixing with synthetic air, the reactant gas stream can be fed into the recycle system or bypassed to analyze the feed gas composition (inlet CO concentration). Part of the product gas stream is passed through a non dispersive infrared analyzer (NDIR-ABB URAS-14) to measure CO and CO_2 concentrations (100 – 500 ppm and 500 – 5000 ppm). The amount of gas passing through the analyzer is adjusted by a needle valve, which also controls the pressure changes in the reaction unit. In a catalytic afterburner (total oxidizer), the product stream is totally oxidized at 320 °C. The afterburner is an electrically heated tubular-flow reactor made of glass with a length and a diameter of 400 mm and 20 mm respectively, equipped with Cu/Mn oxide catalysts pellets in a fixed bed. Pressures and temperatures at various locations of the experimental unit are controlled directly at the apparatus. All temperatures are measured by means of Ni/Cr-Ni-thermocouples (Thermocoax). A safety precaution for pressure increase is realized by a manometer with electrical contact (Bourdon-Haenni), shutting off the pump and the inlet gas flow of CO at system pressures over 1.5 bar.

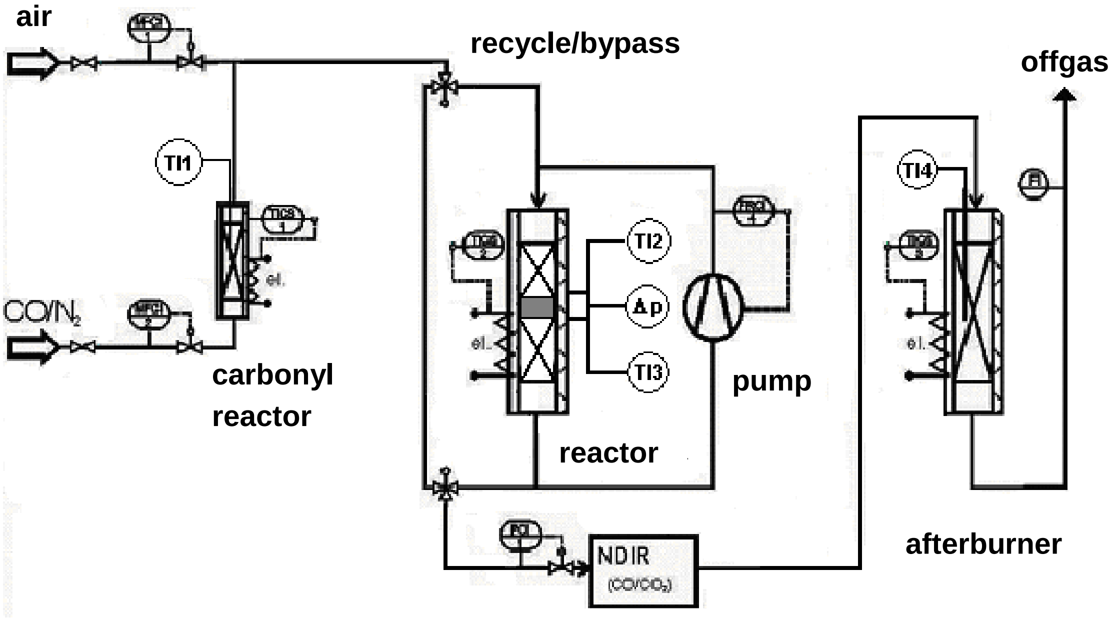

Figure 2.6: Flow sheet of the reaction unit for kinetic measurements.

2.2.7 Reactor packing and system balance

Great attention must be paid to reactor packing. The reactor, a glass tube of 16 (or 25) mm inner diameter and 250 mm length, is connected with two glass joints and stainless steel (Swagelok) fittings to the recycle tubes. Figure 2.7 shows exemplarily a correct packing of a reactor tube with a sponge catalyst. The thin catalyst cylinder (3 – 6 mm length) is carefully packed between the two blank sponge pieces (25 – 35 mm) of the original sponge cartridge to prevent discontinuity and open slits between the pieces. In particular, the blank sponge piece up-flow ensures the full development of the characteristic flow of the gas mixture before it contacts the catalytically coated piece. This part of the packing is wrapped with thin glass fabric to avoid gas-bypassing during measurements. The complete, wrapped segment is pressed into the reactor. Further sponges and glass beads are placed above and below the packed segment of the tube for a better distribution and preheating of the gas before entering the catalytic segment. Thermocouples are laterally inserted into the reactor at the entrance and the outlet of the catalyst bed.

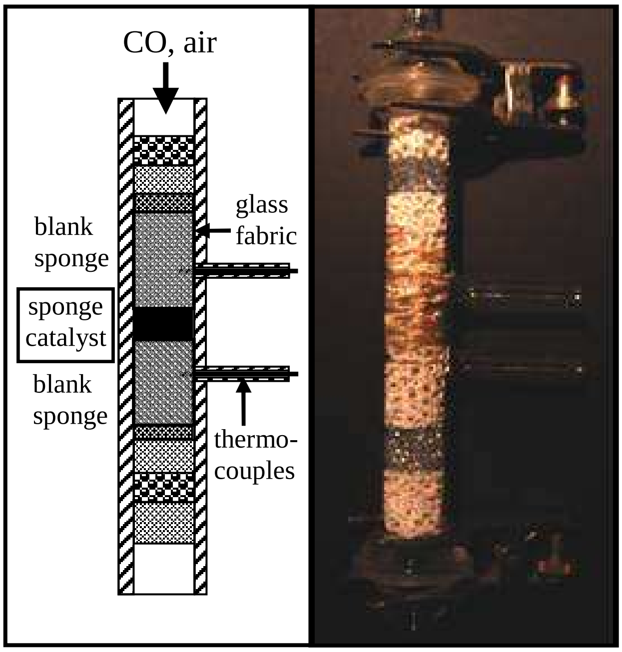

Figure 2.7: Packed reactor for kinetic measurements.

The inlet CO concentrations were kept low between 1000 and 2500 ppm. To calculate the first order rate coefficients, a mass balance was calculated around the whole recycle system (Figure 2.8). In stationary conditions, the mass balance of the system comprising merely the PFR reactor (black dashed square in Figure 2.8) reads (no axial dispersion):

$$0 = -d\dot{n}_{CO,z} + r_v \cdot dV_{B,z} = -\dot{V}_{in} \cdot dC_{CO,z} - k_v \cdot C_{CO,z} \cdot dV_{B,z} \qquad (2.2)$$

which after integration leads to:

$$\ln \frac{C_{CO,out}}{C_{CO,in}} = -k_v \cdot \frac{V_B}{\dot{V}_{in}} \tag{2.3}$$

with

$\dot{n}_{CO,z}$: absolute molar flux of CO at position z [mol/s],

r_v : bulk volume based reaction rate [mol/(m^3·s)],

V_B : bulk volume of the catalytic carrier [m^3],

$\dot{V}_{in}$: reactor inlet flow rate [m^3/s],

$C_{CO,in}$: reactor inlet CO concentration [mol/m^3],

$C_{CO,out}$: outlet CO concentration [mol/m^3],

k_v : volumetric rate coefficient [1/s].

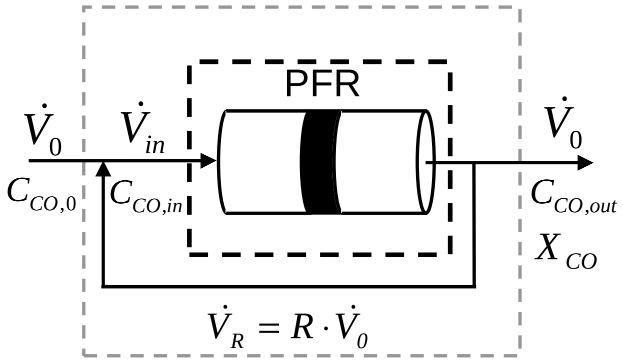

Figure 2.8: Molar balance of a plug flow system (PFR) with external recycle.

However, the reactor inlet concentration and -flow rate are not measured directly. Eq. (2.3) can be expressed as a function of measured variables by mass balancing the CO-fluxes in the mixing point of the recycle:

$$C_{CO,0} \cdot \dot{V}_0 + C_{CO,out} \cdot \dot{V}_R = C_{CO,in} \cdot \dot{V}_{in} \tag{2.4}$$

with

$C_{CO,0}$: system inlet CO concentration [mol/m^3],

$\dot{V}_0$: system inlet flow rate [m^3/s],

$\dot{V}_R$: recycled flow rate = $R \cdot \dot{V}_0$ [m^3/s],

R : recycle ratio [-].

Eq. (2.4) gives, with $\dot{V}_{in} = (1+R)\cdot\dot{V}_0$, the reactor inlet concentration as a function of the known system inlet concentration $C_{CO,0}$:

$$C_{CO,in} = \frac{C_{CO,0} + R\cdot C_{CO,out}}{1+R} \tag{2.5}$$

The outlet concentration of carbon monoxide can be expressed as a function of the system conversion X_{CO}, when the carbon monoxide concentrations are low, directly as:

$$C_{CO,out} = C_{CO,0}\cdot(1-X_{CO}) \tag{2.6}$$

Combining eqs. (2.5), (2.6) and (2.3), and solving for k_v gives:

$$k_v = \frac{(1+R)}{\tau}\cdot\ln\left(\frac{1+R\cdot(1-X_{CO})}{(1+R)\cdot(1-X_{CO})}\right), \tag{2.7}$$

where τ represents the system residence time $\tau = V_B/\dot{V}_0$.

The validity of the assumption of ideal plug flow conditions was confirmed after evaluation of the axial dispersion (Appendix A).

Depending on the kinetic regime being analyzed (e.g. chemical reaction control), it can be convenient to relate the rate coefficient to the mass of the active component Pt. Eq. (2.7) has in this case the same form, with the only difference that the residence time τ is substituted by the modified residence time defined as: $\tau_{\mathrm{mod}} = m_{Pt}/\dot{V}_0$ yielding k_{Pt} instead of k_v.

It is of great importance to balance the system with eq. (2.7) when performing measurements with varying recycle ratios, so as to calculate the accurate, system independent rate coefficients, which are a property of the catalytic structure. When analyzing the kinetics of the CO oxidation on the prepared Pt/SnO_2 sponges at different temperatures, the recycle ratio R was kept constant and high enough (30) to approach the performance of a continuous stirred tank reactor system (CSTR) in most cases. The reaction rate related to the catalyst bulk volume r_v and the 1st order rate coefficient of the chemical reaction k_{Pt} can be calculated in this case by mass balancing the CSTR-system in the steady state giving the simple relations:

$$r_v = \frac{C_{CO,0}}{\tau}\cdot X_{CO} \tag{2.8}$$

$$k_{Pt} = \frac{1}{\tau_{\mathrm{mod}}}\cdot\frac{X_{CO}}{1-X_{CO}} \tag{2.9}$$

The gas hourly space velocity (GHSV, eq. (2.10)) of the CSTR-system was kept constant at 300,000 h^{-1} for all catalysts.

$$GHSV = \frac{\dot{V}_{0,STP}}{V_B} \tag{2.10}$$

At constant hydrodynamic conditions and CO inlet concentrations, the gas temperature was increased from 80 °C until external mass transfer limitation was reached.

2.3 Results and discussion

2.3.1 Loadings of the catalysts

The tin dioxide and platinum loadings of the 45-PPI catalysts (both, impregnation and supercritical deposition) are summarized in Table 2.5. The experimental pressure, temperature and resulting CO_2 density chosen for each supercritical deposition experiment are also included in the table for clarity. The Pt loading of sample SFRD 2 (0.31 wt.-%) is low as compared to samples SFRD 1 (0.71 wt.-%) and 3 (0.91 wt.-%). This can be explained by taking a closer look at the equilibrium solubility of $Pt(COD)Me_2$ in CO_2 and the saturation of the binary mixture. Thereby, the saturation is defined as the ratio of the equilibrium solubility at the prevailing process conditions to the actual dissolved amount of $Pt(COD)Me_2$ in CO_2. The degree of Pt deposition, as defined below, is reduced (Table 2.5):

$$E = \frac{m_{Pt,catalyst}}{m_{Pt(COD)Me_2,used} \cdot (\tilde{M}_{Pt} / \tilde{M}_{Pt(COD)Me_2})} \tag{2.11}$$

where m_i and $\tilde{M}_i$ are the masses and molecular weights of Pt or $Pt(COD)Me_2$. The noticeable lower saturation of the supercritical mixture at higher pressure (14 % for SFRD 2 instead of 64 % at 15.5 MPa and 80 °C) results in a decreased adsorption of the organometallic precursor due to the lower driving force at these conditions. Since only 38 % of the platinum applied is deposited on the catalyst in experiment SFRD 2, a lower pressure (15.5 MPa) seems favorable when focusing on the yield of the used organometallic.

Although the pressure during experiments SFRD 1 and 3 was kept constant, the higher temperature during SFRD 3 results in a lower density (Table 2.5). This results in a decrease of the equilibrium solubility and, therewith, in a higher saturation of the supercritical mixture. This is most probably the reason for the higher degree of Pt deposition on catalyst SFRD 3 as compared to SFRD 1.

Table 2.5: Pt- and SnO_2-contents of the prepared catalysts and experimental conditions for supercritical deposition. The density of the supercritical CO_2 (ρ) was taken from NIST data base [24].

Catalyst		p [MPa]	T [°C]	ρ **[g / cm^3]**	**SnO_2 [wt.-%]**	**Pt [a] [wt.-%]**	**E [b] [-]**
Wet dep.	●	-	-		**6.3**	**0.43**	**-**
SFRD 1	■	15.5	80	**0.449**	**7.3**	**0.71**	**0.65**
SFRD 2	◆	25.0	80	**0.687**	**6.2**	**0.31**	**0.38**
SFRD 3	▲	15.5	100	**0.348**	**6.8**	**0.91**	**0.82**

[a] *Platinum content determined via x-ray fluorescence*
[b] *degree of Pt deposition according to eq. (2.11)*

2.3.2 Surface morphology

SnO_2 layer thickness

The layer of SnO_2 on the Al_2O_3 surface of the sponges is homogeneous along the struts. As can be seen in Figure 2.9, the layer (appearing as a thin white line between the Al_2O_3-carrier and the resin) is 5 – 10 µm thick along the sponge structure and up to 20 µm in regions with a higher concavity.

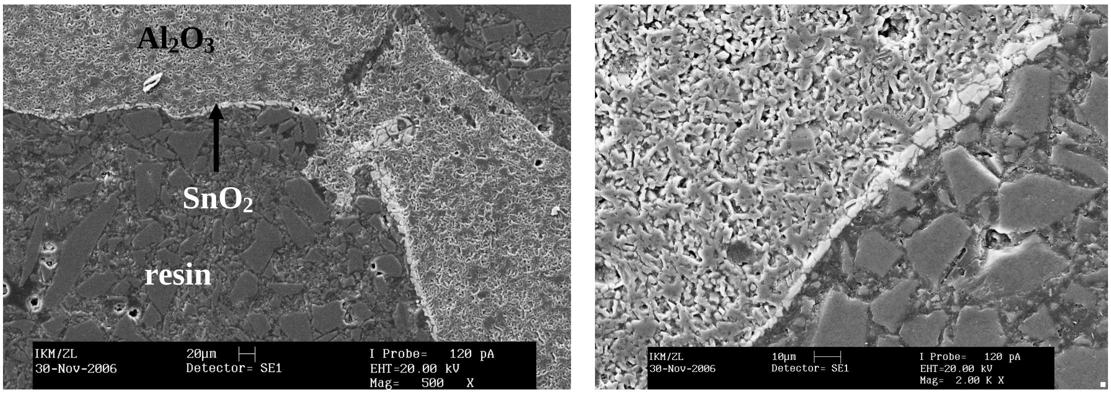

Figure 2.9: SEM images of the SnO_2-layer thickness of a sectioned sponge catalyst embedded in resin.

All sponge geometries were loaded with SnO_2 by the same method. When comparing the average mass percentages of SnO_2 on different pore densities (e.g. 20-, 30- and 45-PPI, $\varepsilon = 80\%$), it becomes clear that the layer thickness of SnO_2 is constant. The average SnO_2 contents of the 20- 30- and 45- PPI sponges were 4.15, 5.25 and 6.65 w.-% respectively, increasing with the geometrical surface area. Based only on the mass of the carrier, the mean loadings in terms of mass ratios (m_{SnO2}/m_{Al2O3}) are:

20-PPI: 0,0433

30-PPI: 0,0554

45-PPI: 0,0712

The relation between the layer thickness s, the geometrical surface per bed volume S_{Geo} and the weight loading can be described as follows:

$$\frac{m_{SnO_2}}{m_{Al_2O_3}} = \frac{\rho_{SnO_2}}{\rho_{Al_2O_3}} \cdot \frac{V_{SnO_2}}{V_{Al_2O_3}} = \frac{\rho_{SnO_2}}{\rho_{Al_2O_3}} \cdot \frac{A_{Geo} \cdot s}{V_{Al_2O_3}} = \frac{\rho_{SnO_2}}{\rho_{Al_2O_3}} \cdot \frac{S_{Geo}}{1-\varepsilon_h} \cdot s \tag{2.12}$$

The ratio of SnO_2- to α-Al_2O_3-density amounts to 1.1 (from mercury intrusion porosimetry (MIP), chapter 3). The mean outer porosity ε_h of the alumina sponges, measured with MIP is approximately 0.75. The geometric surface areas of the sponges were analyzed by means of magnetic resonance imaging (MRI). A detailed description on the morphological characterization of the structures from this work is presented in chapter 3. The values for S_{geo} for the 20-, 30- and 45-PPI samples with 80% porosity are:

20-PPI: S_{geo} = 1187.0 m^2/m^3

30-PPI: S_{geo} = 1437.8 m^2/m^3

45-PPI: S_{geo} = 1884.3 m^2/m^3

The layer thickness should be constant over all pore densities. From eq. (2.12) then follows:

$$s = \frac{0,25}{1,101} \cdot \frac{m_{SnO_2}}{m_{Al_2O_3}} \cdot \frac{1}{S_{Geo}} \overset{!}{=} const., \tag{2.13}$$

leading to the following exemplary values for the three sponges:

20-PPI: s = 8.29 µm

30-PPI: s = 8.76 µm

45-PPI: s = 8.59 µm

The calculated values for the layer thickness not only remain constant within 5.5 %, but also are in good agreement with the results from SEM images taken from 20- and 45-PPI sponges.

Surface morphology of alumina carrier and catalytic layer

The sintered crystalline α-Al_2O_3 structure of the blank carrier sponges used in this work is shown in the left SEM image of Figure 2.10. The material is mostly sintered, leaving only a few pores observable with SEM. The right image (Figure 2.10-B) shows, on the other hand, the scaly structure of the SnO_2 layer of a catalyst from supercritical deposition SFRD 1. The cracks observable on the layer from the second coating step arise upon drying, when capillary forces cause a strong compression and shrinkage of the wash coat.

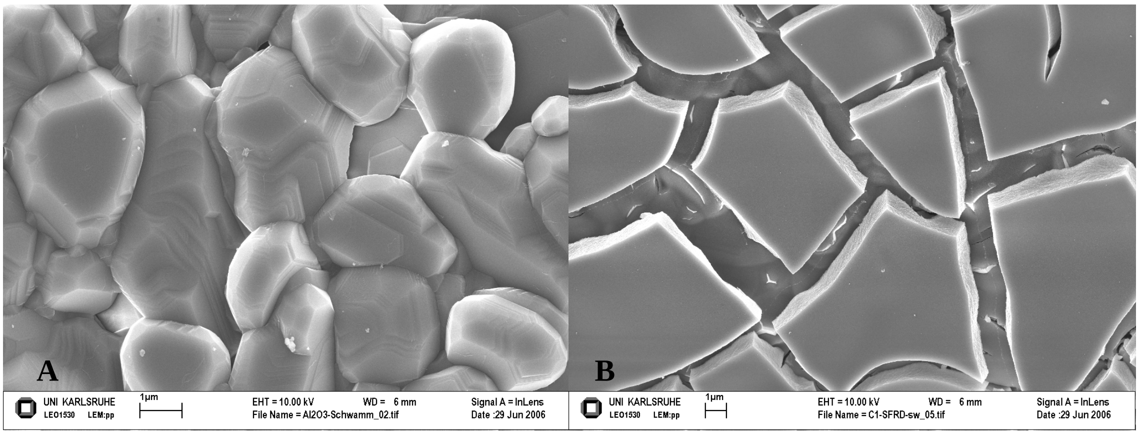

Figure 2.10: *A: α-Al_2O_3-morphology of a blank sponge carrier. B: SnO_2 layers of a coated sponge catalyst (SFRD 1).*

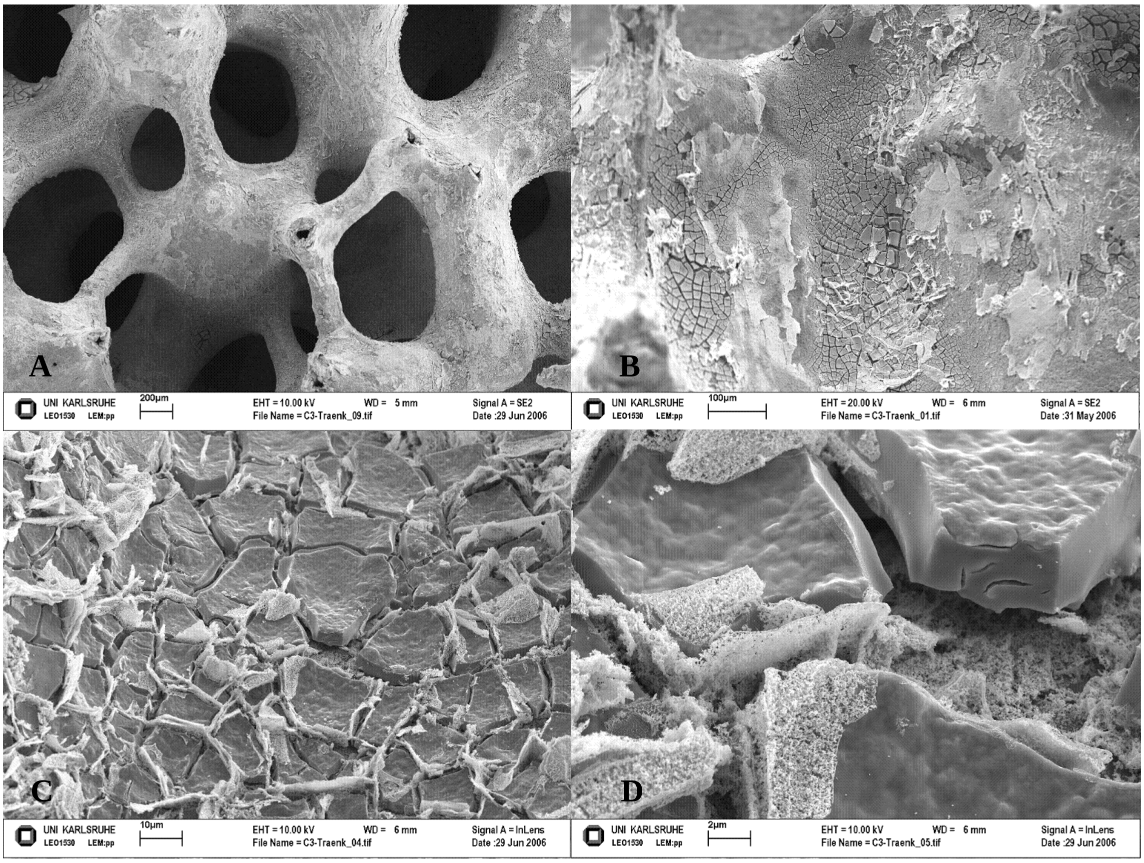

Figure 2.11: *SEM images of sponge catalyst prepared by aqueous impregnation of Pt. A: overall view of the catalyst with recognizable spots. B: Strut intersection with clearly recognizable platinum accumulations on the SnO_2 layer (EDX confirmed). C and D: SnO_2 wash coat with Pt-crystals on and between the cracks of the second layer (different magnifications).*

No platinum particles were visible on the SEM images taken from any of the SFRD catalysts, even though the presence of Pt and, of course, SnO_2 was confirmed with EDX on every analyzed spot of the wash coat, showing characteristic peaks (Pt) at 2.1 keV and 9.4 keV. In contrast, the catalyst prepared through aqueous impregnation exhibited large platinum crystals sticking out on various locations of the SnO_2 surface, especially in the cracks of the wash coat (Figure 2.11-C and -D). Some regions of this catalyst are also completely covered by platinum, resulting in a non homogeneous coloration that is recognizable with the blank eye. SEM images give a better insight into these inhomogeneities. The island-like accumulations of Pt are observable on SEM. The EDX-analysis's of these regions show merely Pt-peaks, with no tin dioxide identifiable. The analysis of the wash coat itself yields both, Pt and SnO_2 signals, similar to the SFRD samples, but with somewhat larger platinum peaks (constant x-ray radiation intensity).

2.3.3 Platinum particle size distribution

The catalyst obtained from supercritical depositions SFRD 1 and 2 show a narrow size distribution of platinum nanoparticles. No significant difference between the size distribution of the Pt particles from SFRD 1 and 2 was observed. Hence, these two catalysts were re-evaluated together giving a single, still very narrow platinum particle size distribution, displayed in Figure 2.12. The average diameter *D* of the Pt particles deposited in catalysts SFRD 1 and 2 amounts to 3.2 nm.

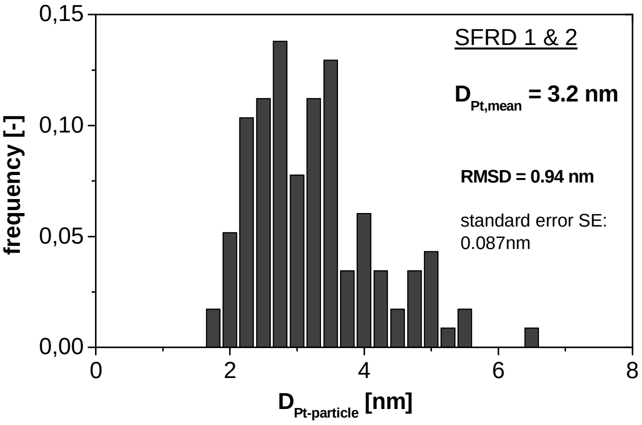

Figure 2.12: Pt-particle size distribution in catalysts SFRD 1 & 2 derived from 117 analyzed particles.

Neither agglomerates nor Pt crystals with diameters exceeding 7 nm were observed. Platinum could be detected, in some cases only weakly, in every analyzed spot of the SnO_2 layer. Figure 2.13 shows a typical TEM image of catalyst SFRD 1 together with a corresponding EDX plot of a platinum- on a tin dioxide nanoparticle.

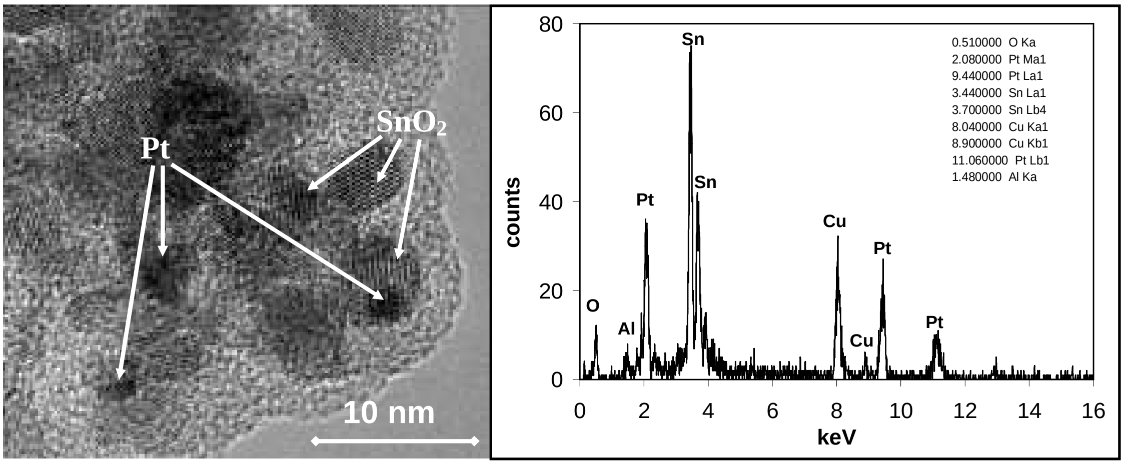

Figure 2.13: TEM and EDX analysis of catalyst SFRD 1.

Catalyst SFRD 3 exhibits a particle size distribution shifted to some degree to larger sizes than the first two, as can be seen in Figure 2.14. Elongated particles were observed, reaching sizes up to 13 nm. Furthermore, some of the particles show signs of coalescence (Figure 2.15), indicating the presence of a liquid phase after adsorption of the platinum complex. The high contrast of the observed Pt in this sample in comparison to the other two catalysts from supercritical deposition is a clear sign of particle growth due to coalescence. EDX-analysis of SFRD 3 shows no appreciable differences.

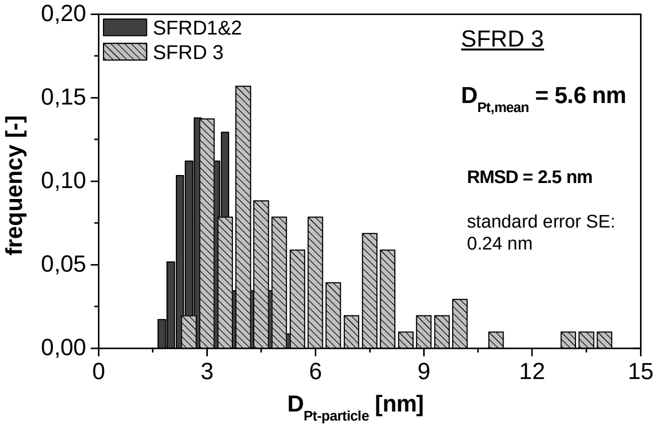

Figure 2.14: Comparison of Pt size distributions between the catalyst SFRD 3 (102 analyzed particles) and the catalysts SFRD 1 & 2.

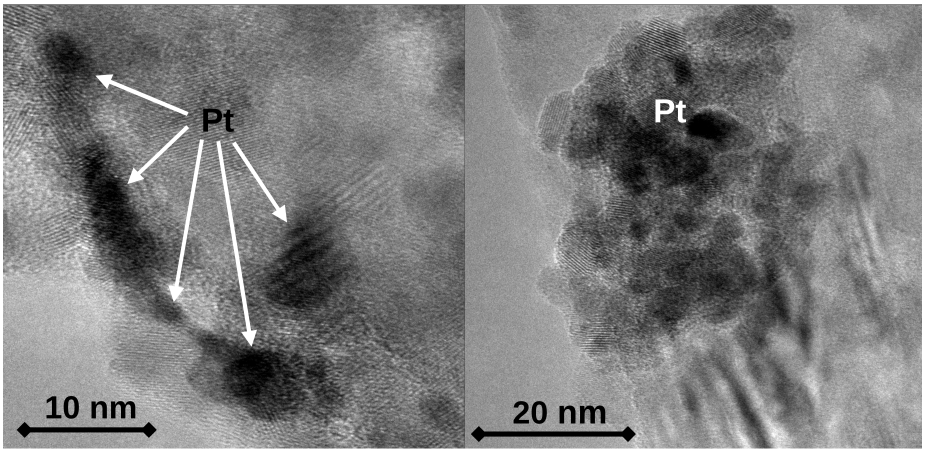

Figure 2.15: TEM images of the active phase of catalyst SFRD 3, showing particle coalescence of Pt-nanoparticles.

The size of the platinum particles deposited on the sponge catalysts by means of SFRD is obviously too small to be observable with SEM. In contrast, aqueous impregnation yields agglomerates of Pt already recognizable with SEM, and a different size and morphology of the particles can be expected in this case. In Figure 2.16, the data of Figure 2.12 and the Pt-particle size distribution of the catalyst from aqueous impregnation were merged for comparison. Although all particles with diameters > 100 nm (in the catalyst made by impregnation) were not taken into consideration, the differences between the two catalyst types are quite obvious. While 7 nm is the maximum particle diameter found in sample SFRD 1 & 2, this value represents the minimum size range of Pt particles on the conventionally loaded sponge; the average platinum particle diameter of this last sample amounts to 27 nm.

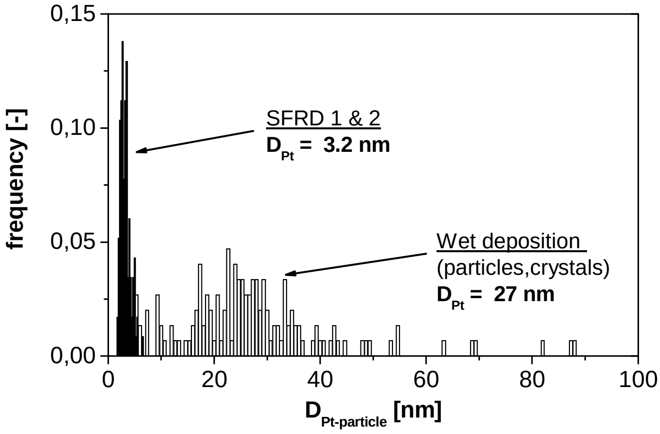

Figure 2.16: Comparison of Pt size distributions between the catalyst from wet deposition (175 analyzed particles) and the catalysts SFRD 1 & 2.

Within the proximity of SnO_2-particles, nanoparticles with diameters between 7 and 20 nm were detected in the sample from conventional preparation (Figure 2.17-A). In these regions, EDX-analyses indicate slightly higher Pt peak intensities than in the case of catalyst SFRD 1. Bigger Pt crystals (Figure 2.17-B) and very large agglomerates with sizes up to 2 µm (Figure 2.17-C) were observed in areas where no tin dioxide could be found, showing EDX-spectra as depicted in Figure 2.17-D. These large Pt particles are of the same type as those visible in the SEM images from the same catalyst (Figure 2.11-C and -D), which are grown in the cracks and reaching out of the surface of the SnO_2 wash coat.

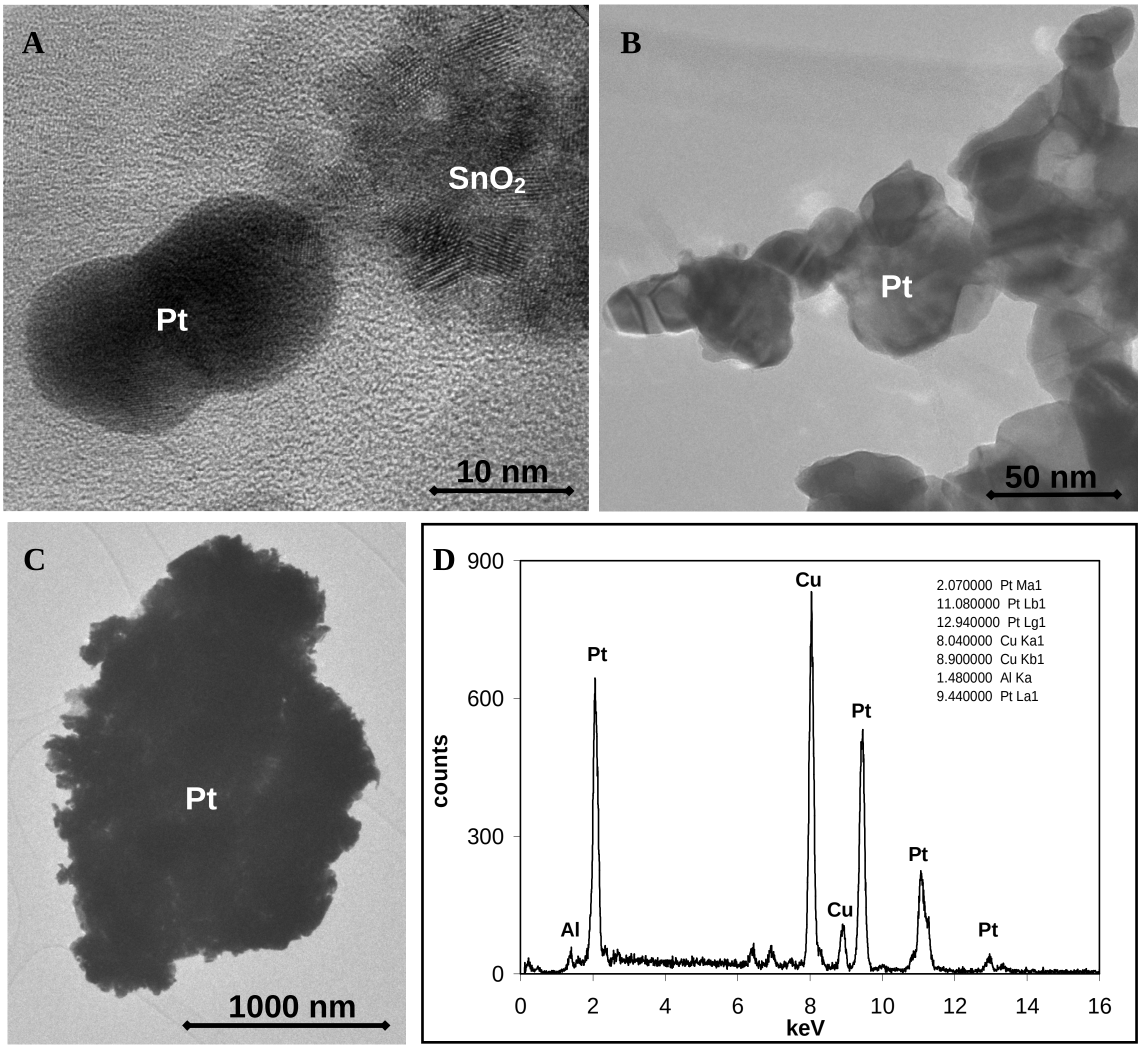

Figure 2.17: TEM- and EDX-analysis of sponge catalyst prepared by aqueous deposition of Pt. A: Pt-nanoparticle. B: Pt-crystals. C: Pt-agglomerates. D: EDX-spectra of the region of the active phase with agglomerated Pt-crystals.

2.3.4 CO oxidation activity

Because the reaction of carbon monoxide with oxygen proceeds at the boundary line between Pt and SnO_2 exposed to the gas phase, it can be anticipated that the sponge loaded with Pt by means of wet impregnation should show a lower activity towards CO oxidation because it contains larger Pt particles, part of which, in addition, have no contact with SnO_2. The volumetric reaction rates of the sponge catalysts (eq. (2.8)) are plotted versus the gas temperature in Figure 2.18. Catalysts from SFRD 1 and 2 showed high activities at moderate temperatures, reaching the region of external mass transfer limitation already at 150 °C. The catalyst stemming from wet deposition exhibited a very low activity below 146 °C. Above 156 °C, a distinct increase in the reaction rate is observed until mass transfer is controlling above 200 °C.

In the temperature regime, where external mass transfer is governing, not the intrinsic activities of the catalysts but rather their surface area are determining the rate. At equal bed volumes and volumetric surface areas, all catalysts should perform at the same rate in this transport-controlled regime. Here, all catalysts except for sample SFRD 3 approached the same high-temperature rate. The lower rate measured over SFRD 3 is ascribed to the lower geometric surface per bed volume (S_{Geo}) of the sponge piece used as carrier for this catalyst. Although all sponge supports were purchased from the same manufacturer, they were not exactly uniform, as will be discussed in chapter 3.

To reveal differences in the intrinsic catalytic activity of the samples, it is necessary to evaluate the data at lower temperatures when the rates are controlled by the chemical reaction rather than by the transport of reactants to the surface. Hence, only the data represented by the filled symbols in Figure 2.18 were used to calculate the rate coefficients k_{Pt}. It should be noticed that these coefficients are related to the platinum content of the catalytic sponges (eq. (2.9)). Therefore, they reflect the intrinsic catalytic activity irrespective of the actual platinum loading. The corresponding Arrhenius plots are depicted in Figure 2.19. Obviously, the slopes of all plots, i.e. the activation energies of the catalysts, are almost the same, which could be expected in view of the similar chemical nature of the catalysts. The absolute activity levels, however, differ and follow the sequence SFRD 1 ≅ SFRD 2 > SFRD 3 > impregnation.

The considerable differences in activity can be ascribed to the diverging degrees of platinum dispersions on the catalysts as described previously, which are highest in case of the samples SFRD 1 and 2, and lowest in case of the sample which was Pt-loaded by means of aqueous impregnation.

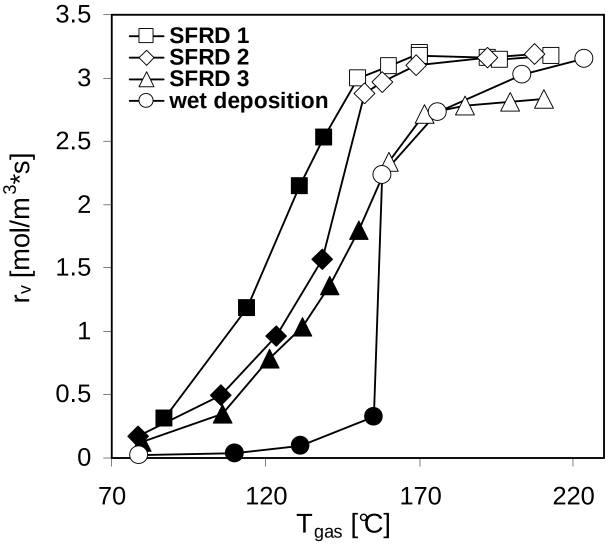

Figure 2.18: Volumetric reaction rates of sponge catalysts as a function of the gas temperature; filled symbols: rate regime governed by chemical kinetics (data taken for plotting rate coefficients in Figure 2.19); open symbols: mass transfer controlled regime.

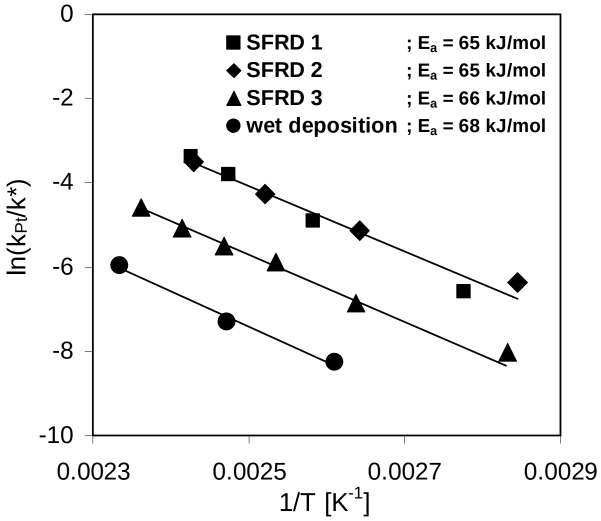

Figure 2.19: Arrhenius plots of the CO-oxidation in the regime of chemical rate control; E_a is the activation energy derived from the slopes.

In contrast to samples SFRD 1 and 2, the platinum loading of SFRD 3 was performed at conditions where the adsorbed Pt(COD)Me_2 could melt. A liquid phase might be formed, if the molecules of Pt(COD)Me_2 are dense enough to form a continuous phase on SnO_2. So, if the available surface area of A_{SnO2} [m^2] on the catalyst is smaller than the required area of the deposited molecules of the organometallic, a liquid phase would form on the SnO_2-layer. The available area for adsorption can be calculated as follows:

$$A_{SnO_2} = m_{cat} \cdot w_{SnO_2} \cdot S_{BET,SnO_2} = 6.44 \text{ m}^2 \qquad (2.14)$$

with

w_{SnO2} (weight-% of SnO_2) = 6.8 %

$S_{BET,SnO2}$ (BET-surface area) = 118 m^2/g (S$_{BET,Al2O3}$ = 0.18 m^2/g , negligible)

With the modelling software Cerius^2 (Accelrys), the molecular structure of $Pt(COD)Me_2$ could be reconstructed. The energetically most favourable atomic arrangement of the organometallic was calculated to obtain the surface and volume of the molecule and its diameter (spherical-like atomic arrangement): 0.8 nm. The value of the area required for adsorption of one complex molecule, taken as the projection of the spherical molecule on the SnO_2-surface, can be then calculated to:

$$A^{molecular}_{PtCODMe_2} = \frac{\pi}{4} D^2_{molecule} = 0.503 \text{ nm}^2 \qquad (2.15)$$

With the molecular weight of the organometallic (333.34 g/mole), the required area per gram can be calculated to:

$$S^{mass}_{PtCODMe_2} = \frac{A^{molecular}_{PtCODMe_2} \cdot N_A}{\tilde{M}_{PtCODMe_2}} = 908{,}72 \text{ m}^2/\text{g} \qquad (2.16)$$

giving the total required area:

$$A_{PtCODMe_2} = S^{mass}_{PtCODMe_2} \cdot m_{cat} \cdot w_{Pt} \cdot \frac{\tilde{M}_{PtCODMe_2}}{\tilde{M}_{Pt}} = 11{,}87 \text{ m}^2 \qquad (2.17)$$

Since $A_{PtCODMe2}$ is higher than A_{SnO2}, a continuous (bulk) phase of $Pt(COD)Me_2$ is formed after adsorption, which most probably melts at the prevailing experimental conditions. The formation of the liquid phase causes coalescence of Pt-complex molecules on the SnO_2-layer, leading to larger Pt particles after reduction, as confirmed with TEM images (Figure 2.15), and thus affecting the dispersion of the noble metal on SnO_2 and with it the activity of the catalyst.

2.3.5 Long term stability

Recycle system

The long term stability of a catalyst is as important for industrial implementation as the activity. The deactivation is predominantly caused by organic impurities in the reactant gas mixture or by thermal effects. Regarding this work, it was important to realize a constant activity high enough to measure the mass transfer properties of a given catalyst (chapter 4) at different hydrodynamic conditions for at least 6 consecutive hours. However, catalyst deactivation was observed to such an extent that the runtime for reproducible measurements was reduced to 2 hours. Presumably, the PTFE membranes of the pump used for the recycle system released hydrocarbons when warm during use. The implementation of a guard bed of zeolite pellets (ZSM5/NaX; 50/50 kept at room temperature) up-flow to the preheating zone of the reactor prevented deactivation for at least 7 hours on stream. The zeolite packing had to be regenerated by calcination in air for 3 h at 550°C. A long term stability run performed on a 45-PPI sponge catalyst from SFRD 1 is displayed in Figure 2.20. At constant *GHSV* of 350,000 h^{-1} and a recycle ratio $R = 7$, the temperature was periodically varied from 80 °C to 205 °C during approximately 800 min. During this period, no deactivation of the catalyst in the mass transfer regime was observed. The CO concentrations used were the same as in the kinetic experiments described in chapter 2.2.7.

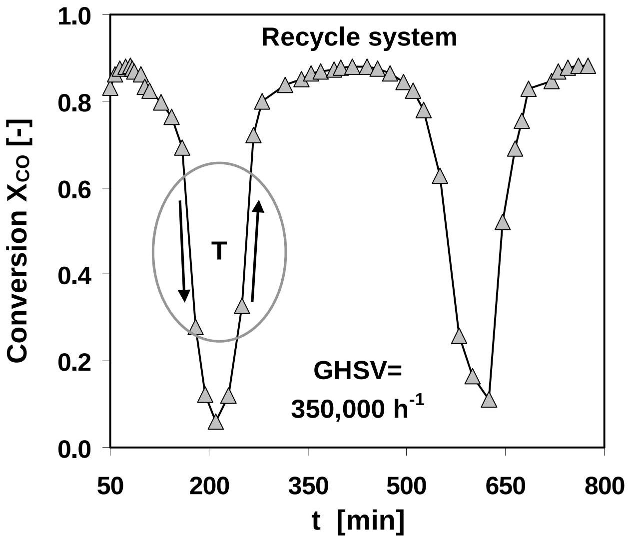

Figure 2.20: Catalyst stability test, performed during 13 hours on a sponge catalyst from supercritical deposition in the recycle system mode.

Once-through mode

The beneficial effect of the zeolite guard bed is, of course, limited by the adsorption capacity of the zeolites. In an attempt to check realistic long term stability, the apparatus was modified to once-through mode, i.e. no external recycle and no zeolite guard bed. A fresh sponge sample (same type as used previously) was packed and tested during 6000 consecutive minutes (100 h). The *GHSV* was kept constant at 250,000 - 300,000 h^{-1}. Temperatures were changed in order to find out in which kinetic regime the activity was affected the most. An earlier test confirmed that the activity remained practically unchanged for longer periods at temperatures below 120 °C. After 3000 h time on stream at temperatures up to 175 °C (Figure 2.21), the activity of the sample decreased between 30 % (95 °C) and 58 % (85 °C). The temperature was then increased to 220 °C and left there for 650 min. The thermal deactivation suffered after this period was very high. The catalyst lost 34 % of its initial activity at 220 °C, 39 % at 170 °C, 67 % at 95 °C and as much as 84 % at 85 °C, as can be seen in the time axis shortly after 4000 min in the figure. The catalyst was subsequently left to reaction at 95 °C for another 1200 min, period after which the temperature was again increased to up to 230 °C, resulting in an activity decrease of 40 % within 150 min at this temperature.

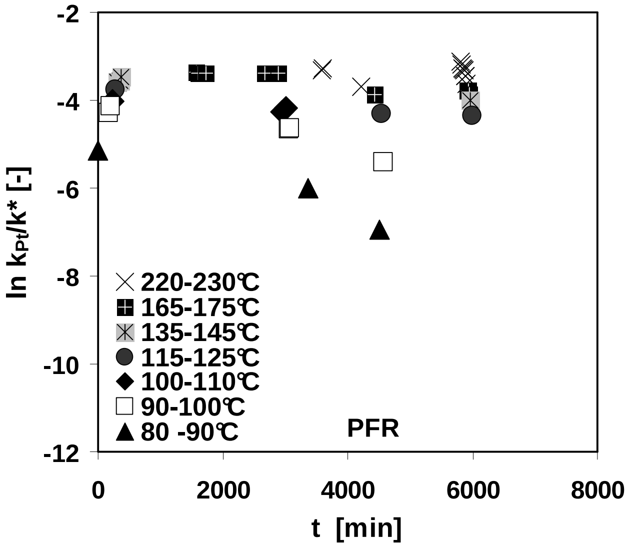

Figure 2.21: Long term stability test in plug flow mode done at different temperatures during 6000 min.

It can be seen from this analysis, that even though high temperatures affect the catalytic activity in the regime controlled mainly by mass transfer to the catalyst (> 120 °C at hydrodynamic conditions in this test), the effect is much stronger at lower temperatures, where the reaction is the principal rate limiting step and the dispersion of Pt in SnO_2 is therefore of stringent importance. The strong deactivation is most probably caused by thermal coalescence of the highly dispersed Pt-nanoparticles on the tin dioxide, lowering the boundary borderline between the noble metal and the metal oxide. From this evaluation it can be concluded that the catalysts from supercritical deposition of platinum are temperature sensitive above 120 °C.

2.3.6 Practical considerations in the characterization of Pt/SnO_2

Since the dispersion plays an important role in the activity of the catalytic system platinum/tin dioxide, two different methods for the characterization of the noble metal dispersion of the prepared catalysts were tried prior to the laborious quantitative characterization of the Pt-distribution with TEM-analysis. The dispersion of platinum (among other metals) on supported catalysts is usually measured by chemisorption or temperature-programmed desorption (TPD) of probe molecules such as H_2, O_2 and CO [32]. These methods are based on the determination of the number of probe gas molecules adsorbing on the platinum atoms. Each probe gas has, of course, a specific stoichiometry factor.

In this work, H_2 chemisorption and CO adsorption on the catalysts were used to characterize as far as possible the dispersion of Pt on SnO_2. To test the reproducibility of these methods, a 1% Pt/Al_2O_3 industrial catalyst (BASF) was also involved. The results from the H_2 chemisorption analysis done on catalysts prepared by Pt-impregnation and SFRD 1 were very surprising, since they showed dispersion degrees higher than one for both analyzed catalysts. This would mean that the apparent amount of active platinum was higher than the amount of total platinum. The reason for this contradictory result can only be the reduction of SnO_2 nearby Pt-sites, the latter catalyzing this reduction [16]. The reduction of SnO_2 implies a hydrogen consumption that can not be predicted. Consequently, H_2 chemisorption is not a suitable method for characterizing the catalytic system Pt/SnO_2.

In a second attempt and following the method of Grass [30], the CO adsorption capacity of the same catalyst types was analyzed. A different problem arose from the experimental results obtained. The catalyst obtained from aqueous impregnation exhibited a CO adsorption capacity comparable to that of the catalyst prepared by supercritical deposition although SEM and TEM analyses had shown considerable differences in particle size and morphology of platinum. Possibly, measurement of the CO adsorption is no suitable method because it characterizes the total Pt surface of a sample (where CO adsorbs) rather than the border line Pt/SnO_2 which is characteristic for the size and dispersion of the metal.

A detailed description of the experimental methods used, the assumptions made and the results obtained is given in Appendix B and C.

It is worth noticing that other authors have also reported that the adsorption of the probe gas on the support of the noble-metal/metal-oxide catalyst significantly affects the accuracy of the metal dispersion results obtained from most methods. For instance, Dawody et al. [32] found quite different values for Pt-dispersion and -particle size of one $Pt/BaO/Al_2O_3$ catalyst, depending on the different methods used, such as CO-TPD, H_2 chemisorption, N_2O decomposition, SEM- and TEM-analyses. These authors conclude that it is always advantageous to combine any of these sorption methods with electron microscopy analyses to obtain more accurate and most of all, reliable results. Moreover, characterization methods involving adsorption of probe gases most often require thermal pre-treatment of the sample that often implies high temperatures up to 600 °C [32,33]. As discussed above, the dispersion of catalytic systems can be reduced at high temperatures.

2.4 Summary and concluding remarks

With knowledge of the thermodynamic behaviour of the system Pt(COD)Me_2/CO_2, allowing the determination of conditions for supercritical deposition with high solubility of the organometallic below its melting point, three experimental conditions for supercritical fluid reactive deposition (SFRD) of Pt on SnO_2-coated 45-PPI sponges were set: 80 °C/15.5 MPa (SFRD 1), 80 °C/25 MPa (SFRD 2) and 100 °C/15.5 MPa (SFRD 3), to evaluate the influence of pressure and temperature during deposition on the catalyst activity.

Catalysts SFRD 1 and 2 showed the highest rate coefficients (k_{Pt}) based on the amount of Pt. Supercritical deposition SFRD 3 was done above the melting temperature of the organometallic. Surface tension affects the dispersion of the deposited platinum due to particle coalescence, resulting in decreased activity for CO oxidation. SnO_2-coated sponges were also loaded with Pt via aqueous impregnation for comparison. The resulting catalytic sponge had by far the lowest activity in CO oxidation. Whereas no Pt was visible on SEM images of the catalysts prepared by supercritical deposition, clear accumulation of large Pt crystals was observed in the cracks of the scaly tin dioxide layer. TEM images allowed for the evaluation of the mean particle size of Pt. While sponges from supercritical deposition experiments exhibited homogeneously distributed Pt nanoparticles with an average diameter of 3 nm – 6 nm, the sample from Pt-impregnation showed a wide size distribution of the deposited Pt, with particles of approximately 30 nm and agglomerates up to 2 µm in size, confirming the substantial influence of Pt dispersion on catalyst activity.

Long term stability tests done on a catalyst from deposition SFRD 1 showed that at temperatures below 120 °C, catalytic activity is stable. Above 130°C thermal deactivation takes place most probably due to coalescence of the dispersed Pt particles.

The results of this investigation clearly show that supercritical fluid reactive deposition is an appropriate and convenient method for the homogeneous deposition of metallic nanoparticles on catalyst supports. The main advantages are its flexibility regarding the geometry of the carrier and the wash coat, low processing temperatures and the absence of contaminants in the ready-to-use catalyst. The high activity and stability at low temperatures of the Pt/SnO_2 catalysts prepared by supercritical deposition could make them attractive for their use in CO removal processes, e.g in the low-temperature fuel cell technology, such as the preferential oxidation of carbon monoxide (PROX). The choice of the most suitable noble metal and metal oxide for this process needs to be thoroughly investigated in future works.

The growing range of organometallic compounds available, based on different metals, make SFRD a most interesting deposition method for the preparation of dispersed catalytic systems for many relevant industrial reactions, where a great variety of combinations of noble metals and metal oxides are needed.

References

[1] I. Langmuir, *The mechanism of the catalytic action of platinum in the reactions* $2CO + O_2 = 2CO_2$ *and* $2H_2 + O_2 = 2H_2O$, Trans. Farad. Soc., 17 (1921) 295 – 333.

[2] T. Engel, G. Ertl, *Elementary steps in the Catalytic Oxidation of Carbon Monoxide on Platinum Metals,* Adv. Catal., 28 (1979) 1 – 78.

[3] S. Fuchs, T. Hahn, H.-G. Lintz, *The oxidation of carbon monoxide by oxygen over platinum, palladium and rhodium catalysts from* 10^{-10} *to 1 bar,* Chem. Eng. Process. 33 (1994) 363 – 369.

[4] S. Fuchs, *Zur Übertragbarkeit kinetischer Daten am Beispiel der Oxidation von Kohlenmonoxid an Platin, Palladium und Rhodium,* Dissertation, University of Karlsruhe, 1994.

[5] T. Hahn, *Zur Extrapolation kinetischer Daten aus Modellexperimenten im Ultrahochvakuum: Die Oxidation von Kohlenmonoxid an Edelmetallen,* Habilitation Thesis, 1994.

[6] R.J. Farrauto, Y. Liu, W. Ruettinger, O. Ilinich, L. Shore, T. Giroux, *Precious metal catalysts supported on ceramic and metal monolithic structures for the hydrogen economy,* Catal. Rev., 49 (2007) 141-196.

[7] K. Grass, H.-G. Lintz, *The kinetics of carbon monoxide on tin(IV) oxide supported platinum catalysts,* J. Catal., 172 (1997) 446-452.

[8] G. C. Bond, L. R. Molloy, M. J. Fuller, *Oxidation of Carbon Monoxide over Palladium-Tin(IV) Oxide Catalysts: An Example of Spillover Catalysis*, J. C. S. Chem. Comm. (1975) 796 – 797.

[9] M. Haruta, T. Kobayashi, H. Sano, N. Yamada, *Novel gold catalysts for the oxidation of carbon monoxide at a temperature far below 0°C,* Chem. Lett. (1987) 405 – 408.

[10] R. Schlögl, G. Loose, M. Wesemann, A. Baiker, *Oxidation of carbon monoxide over palladium on zirconia prepared from amorphous Pd-Zr alloy II. The nature of the active surface,* J. Catal., 137 (1992) 139 – 157.

[11] S. N. Pavlova, V.A. Sadykov, D. I. Kochubei, B. N. Novgorodov, G. N. Kryukova, V. A. Razdobarov, *The structure of supported Pd, kinetics and mechanism of the low-temperature oxidation of carbon monoxide*, in: L. Guczi, F. Solymosi, P. Tétényi (Eds.), *New frontiers in catalysis,* Proceedings of the 10th international congress on catalysis (1993) 2625 – 2628.

[12] M. Haruta, S. Tsubota, T. Kobayashi, H. Kageyama, M. J. Genet, B. Delmon, *Low-temperature oxidation of CO over gold supported on* TiO_2*, a-*Fe_2O_3*, and* Co_3O_4, J. Catal., 144 (1993) 175 – 192.

[13] F. Moreau , G. C. Bond, *CO oxidation activity of gold catalysts supported on various oxides and their improvement by inclusion of an iron component*, Catal. Today, 114 (2006) 362 – 368.

[14] C. J. Wright, C. F. Sampson, *Catalyst preparation*, UK Patent GB 2134004B (1986).

[15] S. D. Gardner, G. B. Hoflund, B. T. Upchurch, D. R. Schryer, E. J. Kielin, J. Schryer, *Comparison on the performance characteristics of* Pt/SnO_x *and* Au/MnO_x *catalysts for low-temperature CO oxidation*, J. Catal., 129 (1991) 114 – 120.

[16] J. E. Drawdy, G. B. Hoflund, S. D. Gardner, E. Yngvadottir, D. R. Schryer, *Effect of pretreatment on a platinized tin oxide catalyst used for low temperature CO oxidation*, Surf. Interface Anal., 16 (1990) 369 – 374.

[17] G. B. Hoflund, S. D. Gardner, D. R. Schryer, B. T. Upchurch, E. J. Kielin, *Effect of* CO_2 *on the performance of* Au/MnO_x *and* Pt/SnO_x *low-temperature CO oxidation catalysts*, Langmuir, 11 (1995) 3431 – 3434.

[18] D.R. Schryer, B.T. Upchurch, B.D. Sidney, K.G. Brown, G.B. Hoflund, R.K. Herz, *A proposed mechanism for* Pt/SnO_x*-catalyzed CO oxidation*, J. Catal., 130 (1991) 314-317.

[19] Y. Zhang, C. Erkey, *Preparation of supported metallic nanoparticles using supercritical fluids: A review*, J. of Supercrit. Fluids, 38 (2006) 252-267.

[20] J. J. Watkins, J. M. Blackburn, T. J. McCarthy, *Chemical Fluid Deposition: Reactive deposition of platinum metal from carbon dioxide solution*. Chem. Mater., 11 (1999) 213-215.

[21] K. S. Morley, P. C. Marr, P. B. Webb, A. R. Berry, F. J. Allison, G. Moldovan, P. D. Brown, S. M. Howdle, *Clean preparation of nanoparticulate metals in porous supports: A supercritical route*. J. Mater. Chem. 12 (2002) 1898 – 1905.

[22] Y. Zhang, D. Kang, C. Saquing, M. Aindow, C. Erkey, *Supported Platinum Nanoparticles by Supercritical Deposition*. Ind. Eng. Chem. Res. 44 (2005) 4161 – 4164.

[23] P. S. Shas, S. Husain, K. P. Johnston, B. A. Korgel, *Nanocrystal arrested precipitation in supercritical carbon dioxide*, J. Phys. Chem. B, 105 (2001) 9433 – 9440.

[24] http://webbook.nist.gov/chemistry/fluid/.

[25] J. J. Watkins, T. J. McCarthy, *Method of chemically depositing material onto substrate*, US Patent 5,789,027 (1998).

[26] G. Incera Garrido, F. C. Patcas, G. Upper, M. Türk, S. Yilmaz, B. Kraushaar-Czarnetzki, *Supercritical deposition of Pt on* SnO_2*-coated* Al_2O_3 *foams: Phase behaviour and catalytic performance*, Appl. Catal. A: General 338 (2008) 58 – 65.

[27] G. Upper, Dissertation in preparation, University of Karlsruhe (TH), 2008.

[28] R. M. Lemert, K. P. Johnston, *Solid-liquid-gas equilibria in multicomponent supercritical fluid systems*, Fluid Phase Equilib. 45 (1989) 265 – 286.

[29] S. K. Kumar, K. P. Johnston, *Modelling the solubility of solids in supercritical fluids with density as the independent variable*, J. Supercrit. Fluids, 1 (1988) 15 – 22.

[30] K. Grass, *Synergismus von Platin und Zinndioxid bei der katalytischen Oxidation von Kohlenmonoxid bei Umgebugstemperatur*, Dissertation, University of Karlsruhe (TH), 1996.

[31] A. Diefenbacher, M. Türk, *Phase equilibria of organic solid solutes and supercritical fluids with respect to the RESS process*, J. Supercrit. Fluids, 22 (2002) 175-184.

[32] J. Dawody, L. Eurenius, H. Abdulhamid, M. Skoglundh, E. Olsson, E. Fridell, *Platinum dispersion measurements for* $Pt/BaO/Al_2O_3$, NO_x *storage catalysts*, Appl. Catal. A: General 296 (2005) 157-168.

[33] B. Mirkelamoglu, G. Karakas, *CO oxidation over palladium – and sodium-promoted tin dioxide: catalyst characterization and temperature-programmed studies*, Appl. Catal. A: General 281 (2005) 275 – 285.

3 Morphological characterization of ceramic sponges

3.1 Introduction

The knowledge of the geometric features of any structure is a prerequisite for the analysis of any further property, be it mechanical strength, mass transfer, heat transfer, or pressure drop, since it is necessary to ascribe correctly transport properties to geometrical or morphological features of the structure such as a characteristic length.

Synthetic ceramic and metallic sponges represent, like the cancellous bone or a natural sponge, an open network of struts that connect in vertices and surround faces (or pores), which, in turn, enclose three-dimensional cells [1]. The most important structural parameters of sponges are:

- mean inner pore and strut diameters : d_p and d_t respectively [m],
- outer (hydrodynamic) and total porosities : ε_h and ε_t respectively [-],
- geometric surface area : S_{geo} [m^2/m^3].

In contrast to known packings like beads and honeycombs, where the geometry is well defined and studied [1-3], the structural features of reticulated cellular materials are difficult to obtain due to their complex and most often irregular geometric properties. Hence, the development of morphological models characterizing in a representative way the macroscopic properties of sponges is not easy to achieve. Various idealising geometric models have been proposed so far, describing ceramic and metallic sponges as cubic cells [4-6], hexagonal arrays [7], or as a regular packing of tetrakaidecahedra (TTKD) [1,8]. The most comprehensive evaluation of the structural properties of cellular materials has been given by Gibson and Ashby [1]. The authors compare packings of space filling polyhedra, namely: triangular-, rectangular- and hexagonal prisms, rhombic dodecahedra and tetrakaidecahedra. They conclude that even though synthetic foams and sponges are anisotropic and not easily geometrically idealized, the structure is best represented as a regular packing of tetrakaidecahedra. The conclusion is based on the good agreement of the average number of edges per face and faces per cell of the TTKD-model as compared to cellular metals (Figure 3.1) and biological tissues.

The space filling packing of TTKD was firstly proposed by Lord Kelvin in 1887 as the most efficient manor to fill space. The TTKD is composed of eight regular hexagons and six squares building the 14 faces of the unit cell, connected by 36 edges and 24 vortices. By introducing a finite strut thickness for every edge, mathematical relations can be obtained for the geometric surface per unit volume and the porosity. Recent studies have shown that the tetrakaidecahedron model can also be used to predict accurately mechanical properties of metallic sponges like effective stiffness and failure strength [8].

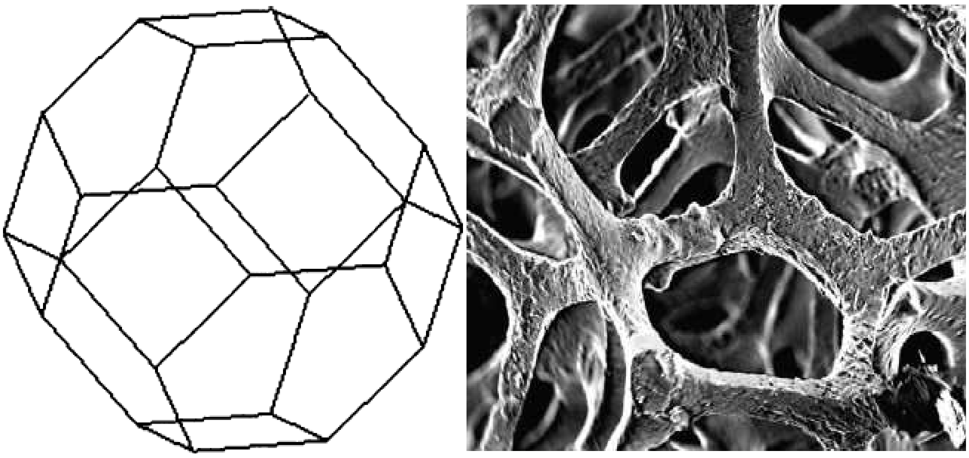

Figure 3.1: Tetrakaidecahedron unit cell (left) and metal sponge (right).

Nevertheless, geometric modelling of sponges is a delicate issue, since the strut network is irregular and the cell shape may be anisotropic rather than spherical. Furthermore, the struts and vortices have unequal thicknesses, and a not quantifiable amount of cells tends to be closed. The irregularities can vary strongly from sponge to sponge, not allowing for a precise morphological description of these structures.

The present chapter focuses on the morphological characterization of ceramic sponges through three different methods:

- microscope image analysis to obtain pore- and strut diameters and cell anisotropy,
- magnetic resonance imaging (MRI) to obtain the geometric surface areas and porosities and a to compare with two geometric models for a sponge,
- mercury intrusion porosimetry to obtain the hydrodynamic relevant (outer) and the total porosities.

3.1.1 Magnetic Resonance Imaging (MRI)

The geometric surface area per bulk volume of ceramic sponges is an important geometric feature and difficult to asses experimentally. It can not be determined via the nitrogen adsorption isotherm (BET) because of the roughness of the ceramic material and because the polymeric template leaves voids inside the solid struts after burn-off. The surface relevant for transport phenomena is the external surface of the struts as if they were perfectly smooth. Therefore, a volume imaging method is necessary. One technique commonly used and already applied to sponges is x-ray absorption tomography [9].

Magnetic resonance imaging (MRI) is another method increasingly used in the field of engineering that allows a three-dimensional imaging of a structure with acceptable image resolution [10]. The principles of MRI experiments can be described by classical-mechanics equations (see eq. (3.1)), although it is based on the quantum mechanical effect of nuclear magnetic resonance (NMR) [11].

Whereas two kinds of magnetic fields are involved in standard NMR experiments, a third type of magnetic field is required for MRI. Firstly, a strong, static and homogeneous magnetic field B_0 (in this work B_0 = 4.7 T) is required to achieve a macroscopic magnetization (M) of the sample. According to Curie's law, M results from the Boltzmann distribution of the spin states of the nuclei of the NMR-active atoms of the sample (here ^{1}H). Per definition, the orientation of B_0 is defined as the z-axis and in thermal equilibrium, M is oriented along z. A second homogeneous magnetic field $B_1(t)$ transverse to B_0 has to be applied to generate transverse magnetization. The nuclear magnetization (M) then experiences a torque $M \times B$ in the (not parallel) magnetic field. As the magnetization is proportional to the macroscopic angular momentum I of the nuclear spins, $M = \gamma I$, the classical equation of motion reads $dI/dt = M \times B$. Multiplying both sides by the substance-specific gyromagnetic ratio γ, the so called Bloch equation (here ignoring relaxation) is obtained:

$$d\vec{M}/dt = \gamma \cdot (d\vec{I}/dt) = \gamma \cdot (\vec{M} \times \vec{B}) \tag{3.1}$$

Hence, the generation of a magnetization transverse to B_0 induces the so-called Larmor precession around B_0, with the angular velocity:

$$\vec{\omega}_0 = -\gamma \cdot \vec{B}_0 \tag{3.2}$$

This precession induces the voltage detected in the NMR or MRI experiment. Usually, the same coil is used to generate the “excitation pulse” $B_1(t)$ and to measure the response signal.

To achieve spatial resolution in MRI, it is necessary to introduce a third kind of magnetic fields, the so-called gradients G_i, which superimpose a linear spatial variation on B_0 along the three dimensions.

$$\vec{G}_j = \partial \vec{B}_z / \partial j \text{ , } j = x,y \text{ or } z \tag{3.3}$$

The resulting magnetic field generated by the gradient in the sample at the location $r = (x,y,z)$ is the scalar product $G \cdot r$, where $G = (G_x, G_y, G_z)$. The gradients produce an additional precession around the z-axis (axis of B_0). The corresponding location-dependent angular frequencies are given by:

$$\vec{\omega}(r) = -\gamma \cdot (\vec{G} \cdot \vec{r}) \vec{e}_z \text{ ,} \tag{3.4}$$

in analogy to eq. (3.2). This place-to-frequency transformation is the basis of MRI. In this simplified description, the NMR-frequency variation due to the so-called chemical shift, which is generally small compared to the frequency shift due to the imaging gradients, is neglected.

By applying magnetic-field gradients, the magnetization, the resulting precessions and their frequency are related to the sample position or location, allowing the spatial resolved scan of the density of nuclear spins $\rho(r)$ in the sample. Starting from eq. (3.1) with initial magnetization along x and including the magnetic field due to imaging gradients, the measured signal (total transverse magnetization) can be shown to equal the Fourier transform of the spin density:

$$M_{total}(\vec{k}) = \iiint_{sample} dxdydz \cdot \rho(\vec{r}) \cdot exp(i\vec{k}\vec{r}) \tag{3.5}$$

with:

$$\vec{k} = \int_0^t dt^* \gamma \cdot \vec{G}(t^*)$$

denoted as the wave vector. In this complex notation, the x and y components of the transverse magnetization are defined with the real and imaginary part of the complex function, respectively.

Spin density imaging can be done for 1-, 2- or 3D with so-called pulse sequences by applying different gradients, exciting local spins in the analyzed dimensions of the sample, and sampling the discrete data over the entire k-space. To increase sensitivity (or signal to noise ratio), a given pulse sequence can be repeated several times. Fourier transformation of the signal reveals the magnetization contributions in the sample as a function of the position along the gradient directions. Nevertheless, the pulse sequences must be largely extended for 3D, making the measurements extremely time consuming. The third dimension is more often approached by the faster alternative of “Slice selection”. Further details on the wide variety of experimental methods of MRI are not within the scope of this work. A detailed description on the background and the different measuring methods in MRI are given by Hardy in [11].

3.1.2 Mercury intrusion porosimetry

The void fraction of cellular ceramics is usually obtained from conventional methods like helium- [12] or water pycnometry by measuring the solid density ρ_S and the bulk density ρ_B of a sponge:

$$\varepsilon_t = 1 - \frac{\rho_B}{\rho_S} \tag{3.6}$$

These techniques yield the total porosity ε_t, since He and water diffuse into the voids of struts of the ceramic material. The supports have two porosities: the outer-, or hydrodynamically relevant macroscopic void space ε_h composed of the continuous cell network between the struts, and the total porosity ε_t, which includes the voids inside the struts as well as the pores inside the solid matrix. It is, therefore, necessary to analyze separately both relevant void fractions.

Mercury intrusion porosimetry is a suitable method for reaching this goal. The outer porosity is obtained by measuring the intruded volume of Hg at atmospheric pressure, where the liquid metal fills merely the cells of the sponge. The volume of the porous strut network V_{strut} is then obtained from the difference between the known volume of the receptacle where the sponge sample is placed (penetrometer) $V_{penetr.}$ and the volume of mercury filled in the penetrometer at atmospheric pressure $V_{Hg,atm}$. The outer density ρ_o can be calculated with known sample mass as:

$$\rho_o = \frac{m_{sample}}{V_{strut}} = \frac{m_{sample}}{V_{penetr.} - V_{Hg,atm}} \tag{3.7}$$

Higher pressures must be applied to fill the remaining voids. The relation between the capillary pressure and the radius of a pore or capillary was given by Washburn [13] from theoretical investigations on the dynamics of capillary flow. It can be easily derived from an energy balance on the edge of a cylindrical pore:

$$p \cdot dV = -\gamma_{Hg} \cdot cos\theta \cdot dA \rightarrow p \cdot \pi \cdot r^2 dL = -\gamma_{Hg} \cdot cos\theta \cdot 2\pi \cdot r \cdot dL \tag{3.8}$$

giving:

$$p = -\frac{2 \cdot \gamma_{Hg} \cdot cos\theta}{r} \tag{3.9}$$

with:

p	:	imposed or capillary pressure	[bar],
γ_{Hg}	:	surface tension of mercury	[N/m],
θ	:	contact angle between Hg and the solid	[-],
r	:	capillary or pore radius	[m],
V	:	volume	[m^3],
A	:	area	[m^2],
L	:	length	[m].

Because mercury causes a contact angle > 90° with ceramic material, pressure has to be imposed to fill a pore. The pressure required for filling a pore increases with decreasing radius of the pore. The maximum pressure applicable is 4000 bar, which corresponds to a minimum pore diameter of 3 nm (eq. (3.9)).

Mercury is pressed into the sample in controlled pressure steps during which the intruded volume of Hg is monitored. After total intrusion, the solid density is calculated from the difference between penetrometer volume and total mercury volume in the system ($V_{Hg,tot} = V_{Hg,atm} + V_{Hg,intr.}$) as:

$$\rho_s = \frac{m_{sample}}{V_{penetr.} - V_{Hg,tot}} = \frac{m_{sample}}{V_{solid}} \tag{3.10}$$

The hydrodynamic- and total porosities of a sample can be obtained from the ratio of bulk density to outer- (or strut-) and solid density, equations (3.11) and (3.6), respectively.

$$\varepsilon_h = 1 - \frac{\rho_B}{\rho_o} \tag{3.11}$$

3.2 Experimental

The carrier structures

Nine ceramic sponges and one metallic sponge were used in this work. The ceramic sponges (99.5 wt. % α-Al_2O_3) were manufactured by Vesuvius Inc. as cylindrical pieces. The cell densities and void fractions as given by the manufacturer were 10-, 20-, 30- and 45- PPI and 0.75, 0.8 and 0.85, respectively.

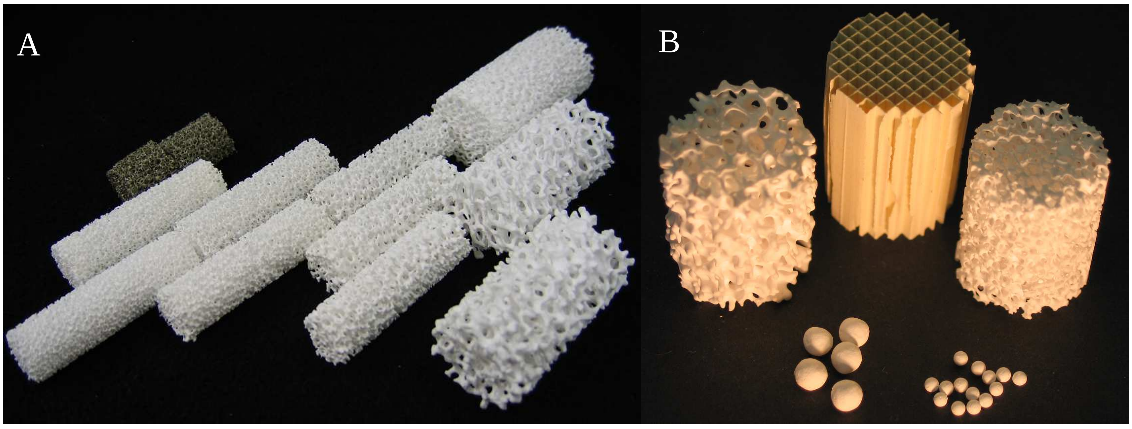

Figure 3.2: A: 10-, 20- 30- and 45-PPI sponges with porosities between 75 and 85 % and a 40-PPI metal sponge (from the right to the left). B: 400 CPSI-honeycomb and 1.5 and 3.3 mm beads compared to 20 and 45- PPI sponges.

The dimensions of the cylindrical pieces varied depending on the cell density, as displayed in Figure 3.2-A. In order to achieve a representative amount of pores over the diameter of a given sample, the 10-PPI samples had 25 mm in diameter, while the 20-, 30- and 45- PPI sponges had a diameter of 15 mm. The 20-PPI sponges with 80%

porosity were analyzed in 15 mm as well as in 25 mm diameter to evaluate the influence of sample dimension. All samples were 50 mm in length.

A cordierite honeycomb (HC) with 400 channels per square inch (CPSI) (Corning) and spherical beads with diameters of 1.5 and 3.3 mm (α-Al_2O_3, Norton) were also analyzed for comparison (Figure 3.2-B). The main geometric features of the packed structures used for comparison are summarized in Table 3.1.

Table 3.1: Properties of honeycomb and beads used for the comparison with sponges.

Carrier	Material	Char. length D_h, D_P [a] [mm]	wall thickness t [mm]	Porosity [%]	Geometric surface [c] [m^2/m^3]
HC 400 CPSI	Cordierite	1.12	0.21	70.9	2534
Beads 3.3 mm	Al_2O_3	3.33	-	44.0 [b]	997
Beads 1.5 mm	Al_2O_3	1.45	-	41.1 [b]	2436

[a] Particle diameter D_p (beads); hydraulic diameter D_h (honeycomb).

[b] Porosity of the packed beads in a 16 mm tube.

[c] Geometric surface per bed volume S_{geo}.

3.2.1 Characterization of the characteristic lengths by image analysis

Two-dimensional characterization of inner pores and struts

From each sponge type, thin cylinders of 4 – 6 mm thickness were cut and analyzed with a LEICA-DM-4000-M microscope. Images were taken from the slices using a LEICA DFC 280 digital camera with an optical magnification of 25. Only clearly focused pores and struts were analyzed from these images by using the Application Suite software from LEICA Microsystems Cambridge Ltd. Two orthogonal lengths were taken from each pore. The strut diameter was determined at the middle of the strut which usually is the thinnest part between the vortices. More than 100 pores and struts were analyzed and statistically evaluated for each sponge type in order to ensure representative values.

Three-dimensional characterization of inner pores

Due to the observed anisotropy of pores and cells, the inner pores of the sponges were analyzed in the third dimension, the depth in direction of flow. 50 mm cylindrical pieces of each sponge were cut along their length, and the pores were analyzed as described above. Nevertheless, merely 30 – 50 pores per sponge type could be analyzed in the plane parallel to flow direction.

3.2.2 Characterization of the geometric surface area and the porosity with MRI

MRI measurements and data processing were performed at the University of Karlsruhe (TH) in collaboration with E. H. Hardy, J. Große and B. Dietrich within the scope of the research group FOR 583 of the German Research Foundation (DFG). The measurements were performed on every sponge type using a Bruker Avance 200 SWB tomograph (magnetic flux density 4.7 T, micro 2.5 gradient system generating up to 1 T/m). Since the ceramic sponges produce practically no signal in MRI experiments, the pore space was imaged by filling it with a liquid active for ^{1}H-MRI measurements. A bubble-free filling with degassed water under vacuum was performed on every cylindrical sponge sample, and copper sulphate (1 g/L) was added to speed-up the relaxation. The resolution obtained in MRI depends on the size of the sample and on the number of volume elements (voxels) chosen. Dividing the investigated field of view by the total number of voxels determines the size of one voxel. Here, the data matrix size was set to 256×256×256 voxels (3-dim) to achieve a reasonable acquisition time. This led to resolutions and fields of view of 50 – 86 µm per voxel and 13^3 – 22^3 mm respectively, depending on the pore density of the sample. The signal to noise ratio strongly depends on the number of averages taken for an image. Previous investigations on the necessary number of averages have shown that two averages give sufficient signal quality for data processing [10].

A threshold for the signal had to be chosen to distinguish regions of high signal (water in voids) from regions of low signal (ceramic). One single threshold was chosen from the histogram of a complete dataset at the minimum between the two peaks. Since only the outer geometric surface is relevant for transport phenomena, an additional step was needed prior to the calculation of the geometric surface. The hollow strut structure had to be filled. For this purpose, an algorithm was developed by E. Hardy, using the fact that the voids in the struts were narrow and concave. The number of solid voxels (no MRI-signal) in the cubic neighbourhood (26 neighbours for each voxel) of each void-voxel was counted. If there were more than 14 solid neighbours, the voxel was identified as void inside the struts and set to solid. In addition, with the filling method the outer porosity can be determined by counting the number of solid voxels in the filled data matrix. The total porosity is obtained by counting the solid voxels of the raw data.

The specific surface area of the filled sponge structure matrix was determined using a Crofton formula, counting and averaging void-solid interfaces along various directions. A detailed description of the theoretical background, the algorithms used, and the principle of this method can be found elsewhere [14].

In order to validate the experimental technique, measurements were also performed on the 400-CPSI honeycomb structure. The only difference was that the algorithm for the filling of the pores was not necessary, since the porous structure inside the solid cordierite channel walls of the honeycomb is sintered after extrusion, leaving nearly no pores inside. The specific surface was calculated with the Crofton formula as well.

3.2.3 Density and porosity characterization of sponges

The densities of the analyzed sponges as well as those of the honeycomb and the beads were measured with a Micromeritics Autopore III 9420 porosimeter. The pressure range used was 0.007 – 1000 bar. Before mercury intrusion analysis, the cylindrical samples were weighted and their bulk volume was measured yielding the bulk density:

$$\rho_B = \frac{m_{sample}}{V_{bulk}} = \frac{4 \cdot m_{sample}}{\pi \cdot \overline{D}_{sample}^2 \cdot \overline{L}_{sample}} \tag{3.12}$$

After vacuum-degassing of the penetrometer where the sample was placed, the system was filled with mercury. Since no pressure was applied, mercury only filled the open cells of the sponge. The mercury-filled sample was then removed from the apparatus and weighted. With known density of mercury and penetrometer volume, the outer density of the solid sponge structure including the hollow void fraction within the struts was calculated with eq. (3.7). The penetrometer was then placed in the high pressure system of the Autopore-porosimeter to fill all remaining voids in the sample. A typical intrusion plot is depicted in Figure 3.3-A.

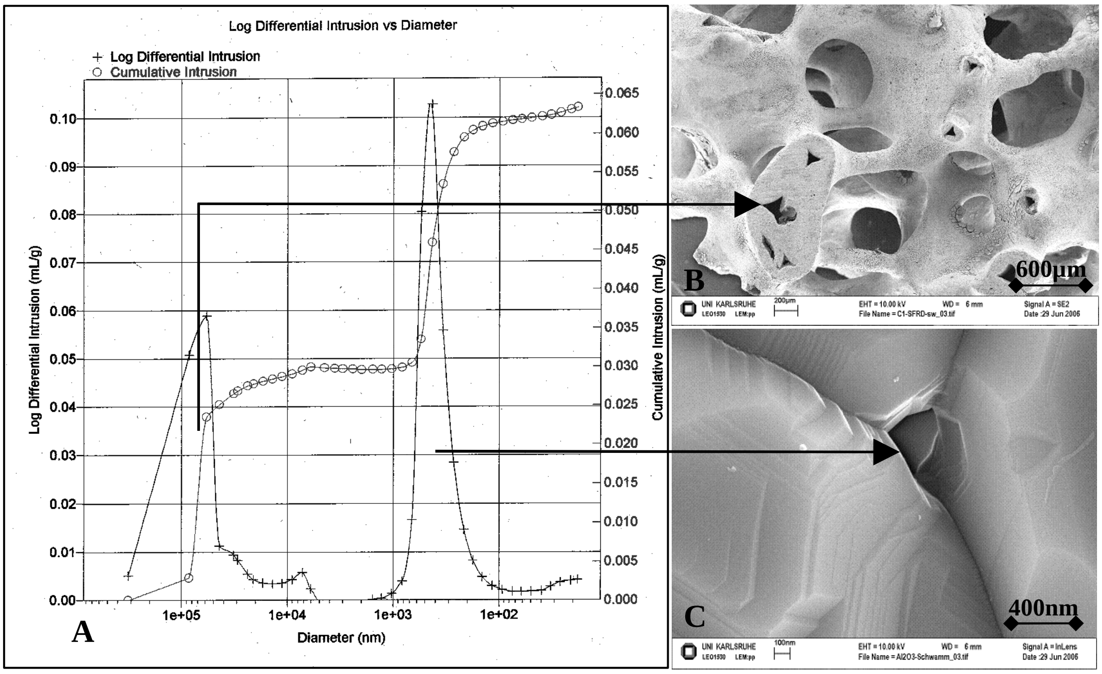

Figure 3.3: A: Hg intrusion as a function of the pore diameter of a 20PPI_0.8 sample (denotation: see Table 3.2). B: SEM image of the hollow triangular strut structure. C: SEM image of a pore between crystals of the α-Al_2O_3 ceramic.

The decreasing diameters along the abscissa correspond to the increasing pressure (eq. (3.9)) during the filling process of the slightly porous solid structure of the sponge. There are two pressure (or diameter) ranges with a steep increase in Hg-intrusion. The first is related to the filling of pores with diameters between 50 and 200 µm. These pores represent the hollow strut network of the ceramic material in accordance with microscope and SEM images from various samples (Figure 3.3-B). At pressures between 30 and 1000 bar, the pores of the not completely sintered ceramic material (12 – 600 nm) are filled (Figure 3.3-C). After intrusion, the density of the solid material and the outer and total porosities were calculated with equations (3.10), (3.11) and (3.6), respectively.

3.3 Results and discussion

3.3.1 Pore and strut size evaluation

Pores and struts orthogonal to direction of flow

Two typical microscope images from the optical characterization are displayed in Figure 3.4. The strut diameters d_t are represented by the black arrows. The two orthogonal lengths taken to calculate the mean inner pore diameter are denoted as *a* (the larger length) and *c* (the shorter length), represented in the figure by white and grey arrows, respectively. The right image in Figure 3.4 shows one pore (the larger one) from which the inner pore diameter can not be correctly measured, since the upper strut is not focused. From the lengths *a* and *c*, the inner pore diameter can be calculated as $\boldsymbol{d_p = (a + c)/2}$. The pore diameter was calculated from cylindrical planes of the sponges, as shown in the upper cylinder of Figure 3.5.

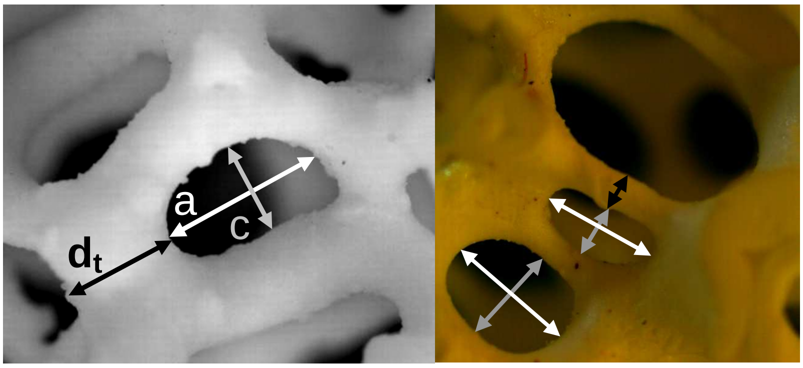

Figure 3.4: Inner pore and strut diameters from image analysis. Both orthogonal pore lengths were considered in the statistical evaluation.

Pore depth in direction of flow: the third dimension

Due to the observed anisotropy in the radial plane, the depth of the pores of all samples was also measured in a second characterization step by cutting the cylindrical samples in the axial direction (lower cylinder in Figure 3.5). In the axial plane, only the depth of the pore *b* could be measured, since depending on the angle of the cut, the visible width of the pore can be altered. In such a case, a slightly different *a** or *c** would be measured. This was confirmed by comparing *a* to *a** and *c* to *c** of some of the sponge samples in both planes. Only the 10-PPI sponges had such an oriented and easily observable anisotropy, so that the axial cut could be carried out in the precise directions of the characterized lengths *a* and *c* from the radial cut. In this case, there was, in fact, a good agreement of the pore lengths in both cuts.

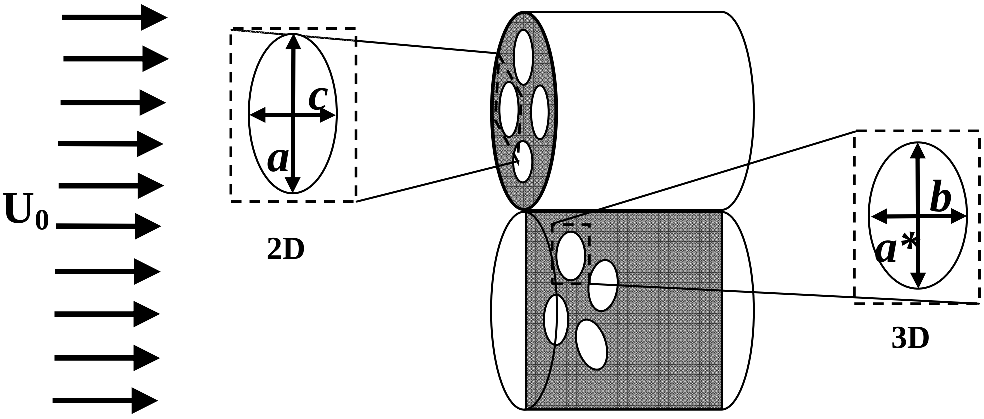

Figure 3.5: Radial- (top) and axial- (bottom) planes of a sponge cylinder with the respective lengths of a pore.

Pore and strut size distribution

Since the most extensive characterization was done in planes perpendicular to the direction of flow, where over 100 pores were analyzed per sponge type, the lengths *a* and *c*, the resulting inner pore diameter ($d_p = (a + c)/2$) and the strut diameter d_t were taken for statistical evaluation. Figure 3.6 shows the broad size distribution of *a* and *c* resulting from the image analysis of the 10PPI_0.85 sponge (for denotation see Table 3.2). There is a marked anisotropy when evaluating both size distributions, even though there is a considerable overlapping. The anisotropy decreases to some extent with increasing pore density.

The pores of all analyzed sponges have a very broad size distribution as shown exemplarily for the 30PPI_0.8 (denotation see Table 3.2) sponge in Figure 3.7. The density of probability from a Gaussian normal distribution having the experimentally determined values for the mean inner pore diameter and the absolute standard deviation is also plotted in the figure for comparison. The inner pore and strut size distribution plots of the remaining ceramic sponges with 80 % total porosity are exemplarily given in Appendix D. While the struts have a rather narrow size distribution, the size of the pores can vary up to one order of magnitude, i.e., in the case of this sponge 0.2 – 2 mm. This tendency was observed among all analyzed samples.

The values for the 30PPI_0.8 sponge were calculated to d_p = 0.871 mm, with a root mean square deviation σ = 0.327 mm (37,6 %) and d_t = 0.319 mm, with σ = 0.075 mm (23.7 %).

The relative deviations of the pore size distributions of the sponges varied between 36 % and 47 %.

The mean pore diameter is here defined as the sum of mean inner pore and strut diameter. It thus represents the average distance between two opposite struts surrounding a pore (Figure 3.4):

$D_p = d_p + d_t = 1.190$ mm.

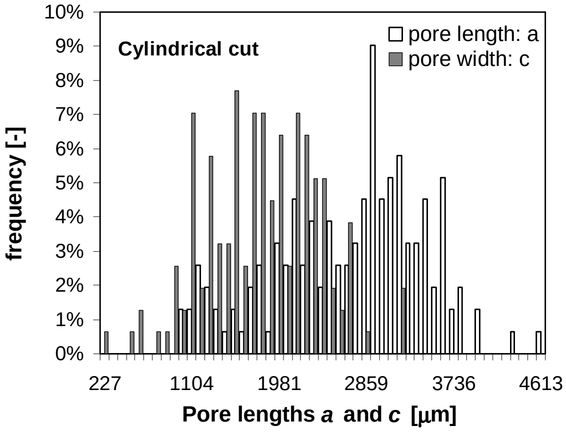

Figure 3.6: Size distribution of pore length and width radial to the flow direction for the 10-PPI sponge with 85 % porosity.

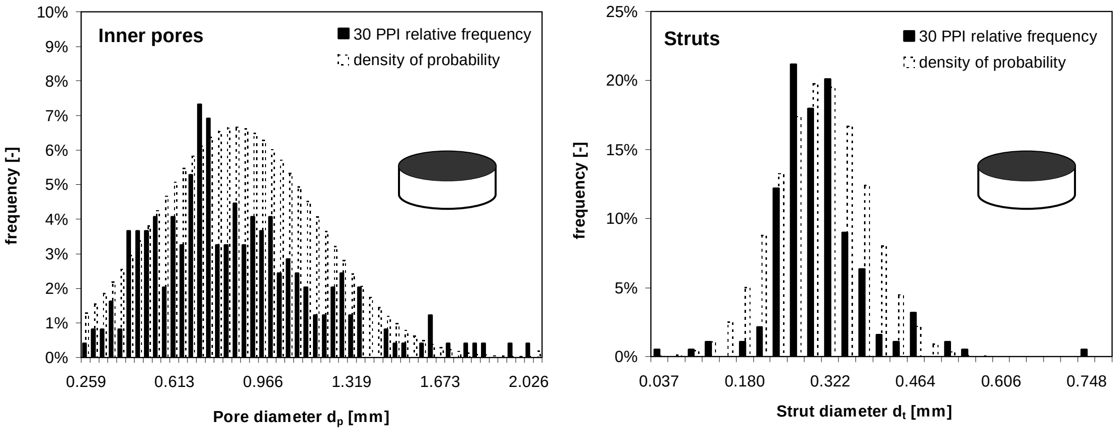

Figure 3.7: Inner pore (left) and strut (right) size distributions (radial to the flow direction) of the 30PPI_0.8 sponge (denotation: see Table 3.2).

The mean pore diameter was chosen as the characteristic length for these structures, since it takes into account the solid and the void of the sponge and should not vary with varying void fraction at constant cell densities. Moreover, the ratios between all measured lengths, inner pore-, strut-, and consequently mean pore diameters (d_p/d_t,

D_p/d_t) remain nearly constant at all pore densities, i.e. the lengths vary proportionally with the pore density. For this reason, the choice of any of the measured features as the characteristic length L_{char} is analogue. The main geometric features of the sponges used in this work are listed in Table 3.2.

Anisotropy

Most sponges are anisotropic, i.e. the strut network is deformed and the cells exhibit ellipsoid shapes oriented in space. Anisotropy is caused already upon fabrication of the polymeric templates and may be enhanced during the replication process which includes squeezing of the greenbodies in one direction. Anisotropy can strongly influence the mechanical strength [1] and the transport properties of sponges and should therefore be quantified, if possible. According to Gibson and Ashby [1], the so-called shape anisotropy ratio R can be determined through the ratio of the largest cell dimension to the smallest. Typically, R lies between 1.3 and 1.5, but it can reach values up to 10. In this work, the anisotropy is more conveniently quantified by ratios of the measured lengths of the inner pores in different directions. It has been discussed and shown in Figure 3.5 what the pore lengths a, b, and c are representing. Figure 3.8 shows three types of pore-anisotropy ratios as a function of the mean pore diameter for the 10-, 20- and 30-PPI sponges with 85 % void. The anisotropy of the 45-PPI sponges could not by evaluated experimentally in a quantitative manner due to the great amount of closed pores, and the accordingly small amount of pores available for measurements in the plane parallel to direction of flow (axial-plane). The ratio a/b would represent the pore anisotropy in the axial direction, a/c the anisotropy in radial direction, and $a^2/(b{\cdot}c)$ would be an approach to the pore anisotropy independently on the direction evaluated.

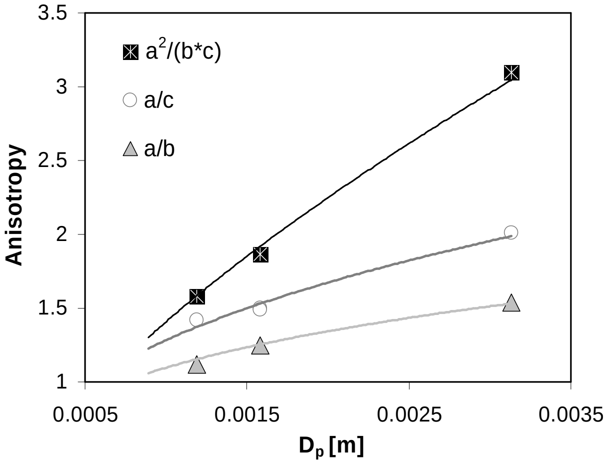

Figure 3.8: Anisotropy ratios defined in this work vs. the mean pore diameters of 10-, 20- and 30-PPI sponges with a porosity of 85 %.

It can be seen that the length a in the radial plane is the longest, since all ratios are bigger than one. Moreover, the ratio a/b has lower values than a/c for all sponges, so the length of b is between a and c. A very important fact recognized during the evaluation of the results concerns the fact that the longest and shortest pore lengths a and c are in the perpendicular plane for the 20-, 30-, and 45-PPI sponges, whereas in case of sponges with the lowest pore density (10-PPI, both porosities), the shortest length c is in the direction of flow. This anomaly can only be ascribed to the manufacturing process. The 10-PPI sponge cylindrical polymeric precursors were most probably cut out in a different direction than the other sponge geometries with respect to the cell orientation of the large pieces of polymeric sponges.

The most convenient quantity for the description of the anisotropy of the pores is the ratio $a^2/(b \cdot c)$ since it is independent on the orientation of the pores in the structures used. The values of the anisotropy ratios of all ceramic sponges are summarized in Table 3.2. Because optical analysis of the 45-PPI sponges has not been performed in 3D, the values of the anisotropy ratio $a^2/(b \cdot c)$ have been estimated by extrapolation from the experimental anisotropy ratios of the other sponges.

Table 3.2: Geometric features and porosities of the sponges used in this work.

Sponge type [a]	Material	d_p [b] [mm]	d_t [b] [mm]	**D_p [c] [mm]**	**$\frac{a^2}{b \cdot c}$ [d] [-]**	ε_t [e] [-] (total)	**ε_h [e] [-] (outer)**	$\varepsilon_{t,MRI}$ [f] [-]	**$\varepsilon_{h,MRI}$ [f] [-]**	**$S_{geo,MRI}$ [f] [m^{-1}]**	$S_{geo,TTKD}$ [g] [m^{-1}]
10PPI_0.8	Al_2O_3	1.933	0.835	**2.768**	**2.55**	0.818	**0.772**	0.806	**0.766**	**675.4**	831.5
20PPI_0.8	-	1.192	0.418	**1.610**	**2.11**	0.804	**0.751**	0.775	**0.751**	**1187.0**	1493.9
30PPI_0.8	-	0.871	0.319	**1.190**	**1.54**	0.816	**0.766**	0.784	**0.740**	**1437.8**	1959.3
45PPI_0.8	-	0.666	0.201	**0.867**	(*1.36*)	0.813	**0.761**	0.769	**0.753**	**1884.3**	2717.9
10PPI_0.85	-	2.252	0.880	**3.132**	**3.04**	0.852	**0.812**	0.831	**0.810**	**629.3**	667.3
20PPI_0.85	-	1.131	0.451	**1.582**	**1.87**	0.858	**0.814**	0.836	**0.811**	**1109.1**	1314.0
30PPI_0.85	-	0.861	0.330	**1.191**	**1.58**	0.852	**0.807**	0.833	**0.814**	**1422.4**	1777.9
45PPI_0.85	-	0.687	0.206	**0.893**	(*1.30*)	0.848	**0.801**	0.794	**0.770**	**1816.3**	2407.8
20PPI_0.75	-	1.069	0.460	**1.529**	**1.52**	0.777	**0.719**	0.722	**0.710**	**1290.3**	1671.1
M-40PPI_0.95	*stainless steel*	*0.628*	*0.174*	***0.802***	-	*0.946*	***0.917***	-	-	-	*1731.5*

[a] Pore count (PPI) and total porosity as reported by the manufacturer; “M” = metal sponge.

[b] From microscopy image analysis: > 100 pores & struts for each sponge type.

[c] Chosen as the characteristic length for dimensional analysis.

[d] Anisotropy ratio from 3D image analysis; in case of 45-PPI sponges: estimated values.

[e] From Hg-Porosimetry.

[f] From MRI-evaluation.

[g] Calculated with tetrakaidecahedron model using D_p and ε_h.

3.3.2 S_{geo}, ε_t and ε_h: MRI-data and model comparison

Figure 3.9 shows a two-dimensional section of the three-dimensional MRI-scan of the 20PPI_0.75 sponge, as well as the same section after data processing with the algorithm used for the filling of the hollow struts.

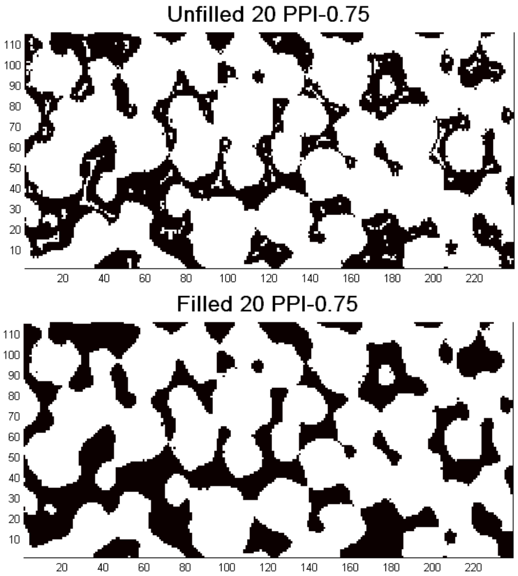

Figure 3.9: Example of data processing of the hollow strut structure from MRI-analysis of the 20PPI_0.75 sponge.

The geometric surfaces per bulk volume $S_{geo,MRI}$ and the porosities $\varepsilon_{h,MRI}$ and $\varepsilon_{t,MRI}$ obtained from MRI-data of the Al_2O_3 sponges analyzed in this work are listed in Table 3.2. As compared to the total porosities provided by the manufacturer and those measured by means of mercury intrusion porosimetry (MIP), the total porosities obtained from the processing of the MRI-data are too low in all cases. The deviation increases with increasing pore density and can be explained by the insufficient resolution of the MRI technique. With a resolution of 50 μm (best case), the strut size of the 30- and 45-PPI sponges correspond to 4 – 6.5 voxels. Some of the inner cavities in these struts have diameters smaller than approx. 40 microns and can not be detected in these measurements. In the case of the outer porosity, this effect expectedly has only little influence on the results. Here, the agreement between MIP and MRI data is satisfactory.

For comparison and validation of the experimental method, the 400-CPSI honeycomb was analyzed with MRI as well. As explained previously, the filling process of the MRI-data was not necessary, as can be seen in the two dimensional section of the raw data displayed in Figure 3.10.

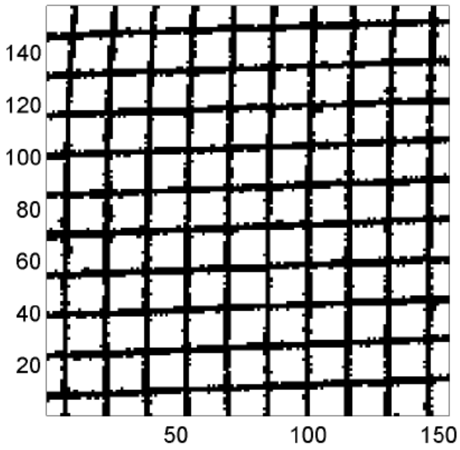

Figure 3.10: Two-dimensional cut of the raw MRI-data matrix of the 400-CPSI honeycomb structure.

As shown in Table 3.3, the porosity obtained from the MRI data processing is in excellent agreement with the porosity determined from MIP. Likewise, the deviations in S_{geo} either determined from MRI or from the morphological evaluation of the honeycomb structure, using experimental values for the porosity and the wall thickness d_w is negligible (1 %).

Table 3.3: Comparison between features from MIP and morphological analysis and features from MRI-experiments of the 400-CPSI honeycomb.

	ε [%]	S_{geo} [m^2/m^3]
MIP/geometrical calculation	70.9 [a]	2534 [b]
MRI-data	70.2	2558

[a] Porosity obtained from Hg-porosimetry

[b] Calculated from the geometrical relation [3]: $S_{geo} = 4 \cdot (\sqrt{\varepsilon} - \varepsilon) / d_W$

Until now, the geometric surface of sponges has been estimated from theoretical models based on regular unit cells. A dense packing of tetrakaidecahedra (TTKD) is one of the geometries that best represents open-cell foams [1]. From this model by Gibson and Ashby, an expression for the geometrical surface per bulk volume was developed by Buciuman and Kraushaar-Czarnetzki leading to [15]:

$$S_{geo,TTKD} = \frac{4.82}{D_p} \cdot \sqrt{\frac{\rho_B}{\rho_s}} = \frac{4.82}{D_p} \cdot \sqrt{1-\varepsilon} \tag{3.13}$$

These authors assumed struts with the shape of triangular prisms. A simpler model recently proposed for the calculation of the specific geometrical surface of sponges is the cubic cell (CC) model. It was originally developed for metallic sponges by Lu et al. [4] and later used by Giani et al. [5] and Lacroix et al. [6]. Assuming ideal cylindrical struts, the following relation results:

$$S_{geo,CC} = \frac{4}{d_t} \cdot (1-\varepsilon) \tag{3.14}$$

The experimental values of $S_{geo,MRI}$ were compared to the values calculated from geometrical models as described above. The experimental values of D_p were taken for eq. (3.13). In the case of $S_{geo,CC}$, two characteristic lengths were tested: first, the measured strut diameters d_t and second, the strut diameter developed from the cubic model by Lacroix et al. as a function of inner pore diameter d_p and porosity ε (eq. (3.15)). The latter results in surface areas closer to the experimental values for $S_{geo,MRI}$ from this work.

$$d_{t,Lacroix} = \frac{\sqrt{\frac{4}{3\cdot\pi}\cdot(1-\varepsilon)}}{1-\sqrt{\frac{4}{3\cdot\pi}\cdot(1-\varepsilon)}} \cdot d_p \tag{3.15}$$

Since both models assume struts without voids inside, the total porosity in eqs. (3.13) - (3.15) has to be substituted by the outer porosity of the ceramic sponges used herein, because these exhibit hollow struts and, therefore, a lower density. The comparison between the measured $S_{geo,MRI}$ and the calculated surfaces $S_{geo,TTKD}$ and $S_{geo,CC}$ of sponges with pore densities between 10 and 45 PPI and porosities between 75 and 85 % is shown in Figure 3.11-A. Obviously, both models overestimate the geometrical surface. One important reason is the assumption of struts with a constant thickness and a cross-section without accumulation of solid. However, in real ceramic sponges, solid material is accumulated in the area of the vortices, where the struts are connected. Furthermore, some pores in real sponges are closed since the ceramic slip can form bubbles in the cells during coating of the polymer matrix. Lacroix et al. [6] also observed the non-homogeneous deposition of matter upon re-infiltration of SiC sponges. The authors ascribed this fact as the reason for the considerable deviations between their calculated (eq. (3.15)) and measured strut diameters at lower porosities. These facts lead to a lower strut surface in real sponges as compared to an ideal network of cubes or tetrakaidecahedra. Not only are the absolute values of the surface areas overestimated, but also the influence of the void fraction. Although the measured values of S_{geo} decrease slightly with the porosity, the dependence is not as strong as predicted by the models. It is worth noticing that the cubic cell model results in a stronger overprediction of the surface area than the tetrakaidecahedron model, as clearly recognizable in Figure 3.11-A. Since the tetrakaidecahedron model displays the most efficient space filling regular network of unit cells, having the lowest geometric surface per volume [1], it is still most probably the best idealized representation of the sponge geometry.

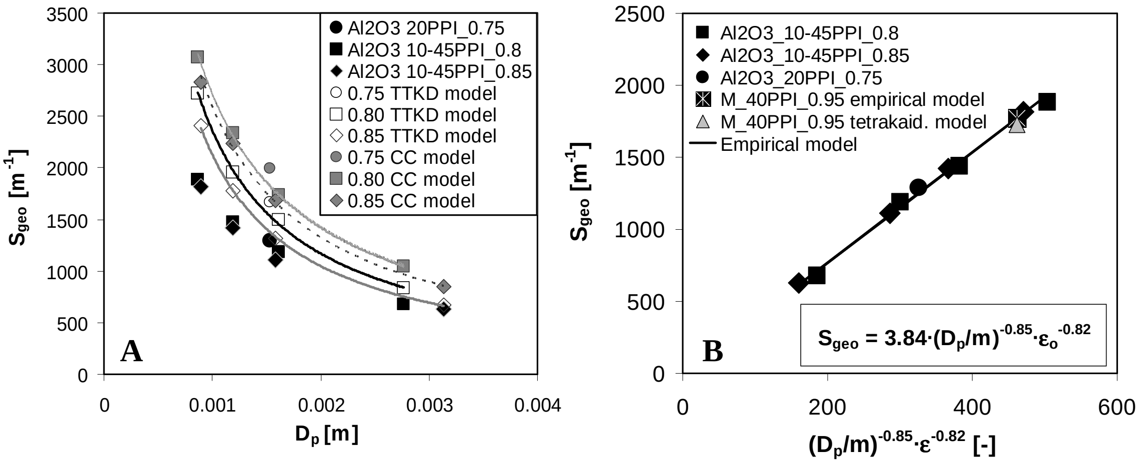

Figure 3.11: A: Comparison between $S_{geo,MRI}$ (black symbols), $S_{geo,TTKD}$ (hollow symbols) and $S_{geo,CC}$ (grey symbols) for all analyzed sponges. B: Correlation between measured values for $S_{geo,MRI}$, D_p and ε_h of ceramic sponges.

The dependency of the measured goemetric surface areas on the mean pore diameter is somewhat lower than $1/D_p$. An empirical model between the geometrical surfaces $S_{geo,MRI}$ and the measured pore diameters D_p and outer porosities ε_h was developed by a simple parameter fitting to the experimental values, resulting in a good correlation of the geometric features of the sponges (Figure 3.11-B).

$$S_{geo} = 3.84\cdot\left(\frac{D_p}{m}\right)^{-0.85}\cdot\varepsilon_h^{-0.82} \tag{3.16}$$

The metallic sponge M_40PPI_0.95 could not be investigated by means of MRI due to the magnetic nature of its material. The geometric surface area of this structure was calculated from the TTKD-model and from the empirical model proposed in eq. (3.16) with the experimental values for D_p and ε_h. As can be observed in Figure 3.11-B, the difference between both models is negligible. Since the porosity of metal sponges is high (usually > 90 %) in comparison to ceramic sponges, the struts have lower concavity and accumulation of solid at the vortices, leading to a strut structure closer to the ideal morphology of a tetrakaidecahedron. This is most probably the reason for the good agreement between both models when applied to the metallic carrier.

3.3.3 Outer- and total densities and porosities from mercury porosimetry

Table 3.4 shows exemplarily the average values of the measured outer and total densities of 20- and 45- PPI ceramic sponges. The value for the solid density remains practically unchanged since the ceramic material used is the same. The outer density ρ_o is also similar for all sponge types, with a maximum variation of 5.4 %. The porosity of the strut network ε_{strut} of all ceramic sponges used herein is approx. 22 %, calculated from eq. (3.17).

$$\varepsilon_{strut} = \frac{\rho_s - \rho_o}{\rho_s} = 1 - \frac{V_s}{V_s + V_{void,strut}} = \frac{V_{void,strut}}{V_s + V_{void,strut}} \tag{3.17}$$

The considerable difference between outer and total porosities of the analyzed structures (Table 3.2) results from the strut porosity and lies in the range of 5 % (ε_t = 85 %) - 7.5 % (ε_t = 75 %).

Table 3.4: Bulk density and porosity variations of 20- and 45-PPI ceramic sponges.

Sponge	axial position	**ρ_B [g/cm^3]**	ρ_o [g/cm^3]	ρ_s [g/cm^3]	**ε_h [-] (outer)**	ε_t [-] (total)
20PPI_0.8	end	**0.780**	3.081	3.934	**0.747**	0.802
20PPI_0.8	end	**0.870**	3.177	3.976	**0.726**	0.781
20PPI_0.8	middle	**0.733**	3.066	3.945	**0.761**	0.814
20PPI_0.8	middle	**0.740**	3.111	3.970	**0.762**	0.814
20PPI_0.85	end	**0.607**	3.055	3.933	**0.801**	0.846
20PPI_0.85	middle	**0.538**	3.010	3.925	**0.821**	0.863
45PPI_0.85	end	**0.710**	3.053	3.989	**0.767**	0.822
45PPI_0.85	middle	**0.447**	2.941	3.976	**0.848**	0.888

While the average porosities of the cylindrical sponges with 50 mm length as supplied by the manufacturer have usually the total porosity as specified, significant deviations from these porosities were observed along different axial locations of the cylindrical pieces after cutting off the edges. The variations arise from the anisotropic bulk density along the sponge that results during removal of excess ceramic slurry in the manufacturing process, leading to higher densities (lower porosities) in the edges of the cylinders and lower densities in the middle part. Between a 15 mm piece from the edge and one from the middle of a 50 mm sponge as delivered, the maximum bulk density variation observed was as high as 45 %, leading to an absolute porosity variation of 10 %. The inhomogeneity of the cylindrical sponges commonly increased with increasing pore count. Typical results of these variations are shown in Table 3.4. For this reason, the evaluation of the bulk densities of 6 - 8 different sponge pieces per sponge type was necessary in order to get representative averages for the void fractions of these structures. The mean values for the outer and total porosities of the analyzed sponges are presented in Table 3.2.

3.4 Summary and conclusions

The extensive morphological characterization of the sponges used in this work allowed for the insight of important features of these structures. Mean values for the inner pore- and strut diameters were obtained from the statistical evaluation of the image analysis on the sponges. The mean pore diameter, defined as the sum of average inner pore- and strut diameters, was chosen as the characteristic length. Image analysis of the sponges revealed not only the expected increase in pore- and strut diameters with decreasing pore density, but also a systematic increase in pore and cell elongation. Magnetic resonance imaging of the sponges gave insight to an important feature, the geometric surface area. The experimentally analyzed surface areas of the sponges used herein are somewhat lower than the ones predicted from morphological models of regular packings of tetrakaidecahedra and of cubes, since these models do not account for the significant accumulation of solid material in the strut connections. The dependence of the measured surface areas on the mean pore diameter is slightly lower than $1/D_p$. The dependence on the porosity is low within the range of void fractions analyzed (75 – 85 %). Mercury intrusion porosimetry allowed the measurement of outer- and total porosities of the sponges. All ceramic sponges analyzed have a porous strut network with a void space of approx. 22 %, resulting in considerable differences of 5 – 7 % between their total- and outer porosities.

An extremely important conclusion gained from the characterization of density and porosity in ceramic sponges is the fact that large deviations in the bulk density can arise along the axial direction of the sponge cylinders. The difference in bulk density between an edge and the middle part of a sample can be as high as 45 %, leading to porosity variations up to 10 %. This represents a critical issue in the implementation of sponges for industrial purposes, since variations in porosity along a sponge packing are extremely detrimental when used in a large reactor due to the strong dependence of permeability on the sponge density. An optimization of the manufacturing process of sponges regarding this point is completely necessary.

The morphology of reticulated sponges is rather difficult to characterize due to their irregular and tortuous nature. The herein used techniques allowing for the insight of surface area and porosity of sponges are rather sophisticated. For the practical use of sponges, it is hence of extreme importance to develop simple models for the reliable prediction of these features from the mean pore and/or strut diameters which are easier to analyze. Cell (or pore) anisotropy has considerable influence in the transport properties of sponges (chapter 4). Its evaluation is laborious since the sample has to be analyzed in 3D, destroying a great amount of specimens for a representative analysis. For this reason, a model for the prediction of cell elongation from the pore diameter in one plane would be advantageous. However, to this point, it can not be judged whether cell anisotropy remains unchanged or changes radically, depending on the manufacturer or the ceramic or metallic material used. This issue should be evaluated in future works.

References

[1] L. J. Gibson, M. F. Ashby, *Cellular solids. Structure and Properties*, Pergamon Press, Oxford, UK, 1988.

[2] D. P. Haughey, G. S. G. Beveridge, *Structural properties of packed beds – A review*, Can. J. Chem. Eng. 47 (1969) 130 – 140.

[3] A. Cybulski, J.A. Moulijn, *Monoliths in heterogeneous catalysis*, Catal. Rev.-Sci. Eng. 36 (1994) 179 – 270.

[4] T. J. Lu, H. A. Stone, M. F. Ashby, *Heat transfer in open-cell metal foams*, Acta Mater. 46 (1998) 3619 – 3635.

[5] L. Giani, G. Groppi, E. Tronconi, *Mass-transfer characterization of metallic foams as supports for structured catalysts*, Ind. Eng. Chem. Res. 44 (2005) 4993-5002.

[6] M. Lacroix, P. Nguyen, D. Schweich, C. P. Huu, S. Savin-Poncet, D. Edouard, *Pressure drop measurements and modelling on SiC foams*, Chem. Eng. Sci. 62 (2007) 3259 – 3267.

[7] V. V. Calmidi, R. L. Mahajan, *The effective thermal conductivity of high porosity fibrous metal foams*, ASME J. Heat Transfer 121 (1999) 466 – 470.

[8] Y. W. Kwon, R. E. Cooke, C. Park, *Representative unit-cell models for open-cell metal foams with or without elastic filter*, Mater. Sci. Eng. A 343 (2003) 63 – 70.

[9] J. Vicente, F. Topin, J.-V. Daurelle, *Open celled material structural properties measurement: From morphology to transport properties*, Mater. Trans. 49 (2006) 2195 – 2202.

[10] J. Große, B. Dietrich, H. Martin, M. Kind, J. Vicente, E. H. Hardy, *Volume image analysis of ceramic sponges*, Chem. Eng. Technol. 31 (2008) 307 – 314.

[11] E. H. Hardy, *Magnetic Resonance Imaging in Chemical Engineering: Basics and Practical Aspects*, Chem. Eng. Technol. 29 (2006) 785 – 795.

[12] J. T. Richardson, Y. Peng, D. Remue, *Properties of ceramic foam catalyst supports: pressure drop*, Appl. Catal. A: General 204 (2000) 19-32.

[13] E. W. Washburn, *The dynamics of capillary flow*, Phys. Rev. 17 (1921) 273 – 283.

[14] J. Ohser, F. Mücklich, *Statistical analysis of microstructures in materials science*, Wiley, Chichester, Weinheim, 2000.

[15] F. C. Buciuman, B. Kraushaar-Czarnetzki, *Ceramic foam monoliths as catalyst carriers. 1. Adjustment and description of morphology.* Ind. Eng. Chem. Res. 42 (2003) 1863 – 1869.

4 Mass and momentum transfer phenomena upon flow through open-cell sponges

4.1 Introduction

It has been stated in the first chapter that sponge structures have a great potential in industrial applications involving gas-solid catalytic processes at short contact times and high reaction rates, often controlled by diffusion limitations. Despite of a few published studies on the mass transfer characteristics of these structures [1,2], no consistent evaluation of the influence of sponge morphology on mass transfer has been reported, yet. For engineering purposes, the correlation of momentum and mass transfer to morphologic properties of sponges is essential. The analysis of geometric characteristics of sponges with four different pore sizes and three porosities is reported in chapter 3. With knowledge of mean pore and strut diameters as well as porosities and geometric surface areas of the used sponges, the influence of sponge geometry on mass transfer and pressure drop can be evaluated.

The present chapter focuses on the measurement of mass transfer coefficients and pressure drops of sponges with different pore densities and porosities over a wide hydrodynamic range. For validation of the experimental method and for comparison of the performance of different geometric structures, mass transfer coefficients and pressure drop of well studied structures such as fixed beds of spheres [3] and honeycombs [4] are also analyzed. Here, a trade-off index between the volumetric mass transfer and the pressure drop as defined by Giani et al. [5] is used to allow a quantitative comparison of the different carriers.

The main objective is to yield a general dimensionless correlation for the prediction of mass transfer coefficients of sponges from hydrodynamic or pressure drop data in a wide variety of pore densities and porosities.

4.2 Theory

4.2.1 Mass transfer

The term “mass transfer” refers to the motion of molecules or fluid elements caused by any form of driving force, including not only molecular diffusion but also transport by convection. Steady state molecular diffusion is described by means of the first Fick’s law (one dimension):

$$J_A = -D_{AB} \cdot \frac{dC_A}{dy} = -\tilde{\rho}_{\mathrm{m}} \cdot D_{AB} \cdot \frac{dY_A}{dy} \tag{4.1}$$

with

J_A	:	diffusive flux density of component A	[mol/(m^2·s)],
D_{AB}	:	diffusion coefficient or “diffusivity”	[m^2/s],
C_A	:	concentration of component A in B	[mol/m^3],
$\tilde{\rho}_{\mathrm{m}}$	:	molar density	[mol/m^3],
Y_A	:	molar fraction	[-].

The diffusion coefficient, originally derived from the kinetic theory of ideal gases, is a property of the binary gas mixture and independent of concentration (at low densities). A widely accepted relation for diffusion coefficients in gases was suggested by Fuller [6] (Appendix E).

Mass transfer at a phase boundary

When transport to or from a phase boundary is merely by molecular diffusion and the flow field is known as if the flow would be laminar, rate equations relating the variables affecting the diffusive process can be developed. In most processes, however, the flow is turbulent to some degree and the flow field is not well specified. For this situation, different mathematical models have been developed [7].

The stagnant-film model was proposed in the beginning of the century by Nernst [8] and has been widely applied to both, heat- and mass transfer. The model is based on the fact that the local velocity approaches zero at the surface when a fluid flows over a phase boundary. Resistances to mass (and heat transfer) are usually confined to a region quite close to the phase boundary, suggesting the idea of a stagnant film through which transport is solely by molecular diffusion. The stagnant film is of a thickness y_0 as to explain the experimentally observed magnitude of the mass transfer resistance. Though the model oversimplifies the actual conditions near the phase boundary, it has been shown to be useful in several applications, giving reliable predictions for mass- and heat transfer rates in laminar and turbulent flow [7,9]. Figure 4.1 illustrates the situation of mass transfer of a fluid A in a binary mixture to the surface of a solid catalyst with an activity high enough, so that the concentration of the reacting component A is zero at the surface. The real overall resistance to mass transfer is described by the model within the film of effective thickness y_0, where the concentration drops from the bulk concentration at the $y = y_0$ to zero at $y = 0$. The unbroken curve displays the true concentration profile, and the broken profile is predicted by the film model.

The linear slope shown in the figure can only be taken in the case of equal-molar counter diffusion where $N_A = -N_B$, or in dilute gas systems, where the additional convective transport of molecules of A in direction of J_A is negligible.

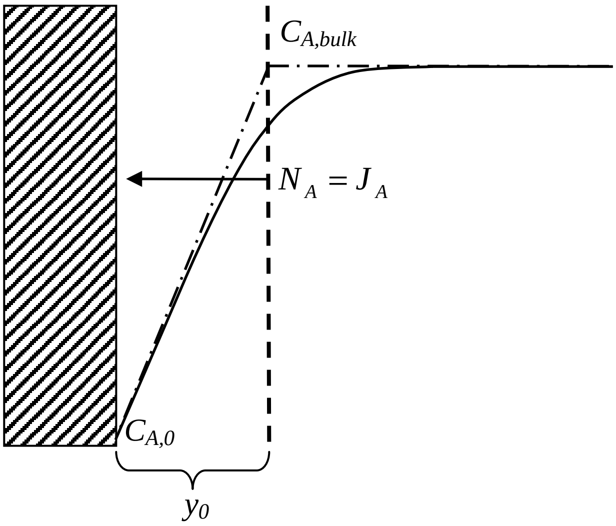

Figure 4.1: The film model profile (broken) and the true profile (unbroken) of the concentration of A in the case of mass transfer from the bulk fluid to the solid surface of a catalyst.

The correlations of mass-transfer data which employ dimensionless groups stem from the film theory. The physical meaning of y_0 is that this film thickness depends strongly on the flow conditions and the properties of the fluid. If the velocity is increased or the viscosity is decreased, the film will become thinner, thereby enhancing the net mass transfer.

The mass transfer coefficient is defined by Sherwood as the ratio of the net molar flux N_A to the driving force for diffusion ΔC_A, giving after integration of eq. (4.1):

$$k_m = \frac{N_A}{(C_{A,y_0} - C_{A,0})} = \frac{D_{AB}}{y_0} \tag{4.2}$$

In engineering processes, the flow is extremely complex due to tortuous geometric arrangements where the use of y_0 is unsuitable, since local conditions vary over a large area of the phase boundary. The film thickness can be replaced by a system specific length dimension to develop a convenient dimensionless group for the general description of the physical phenomenon studied. Analogue to the film thickness, the dimensionless mass transfer coefficient will depend on the hydrodynamic conditions and fluid properties of the system, which can be termed in dimensionless form as well:

$\frac{k_m \cdot L_{char}}{D_{AB}} = f(Re, Sc) = Sh$, referred to as the Sherwood number, with (4.3)

$$Re = \frac{U_0 \cdot L_{char}}{\nu}\text{, the Reynolds number and} \tag{4.4}$$

$$Sc = \frac{\nu}{D_{AB}}\text{, the Schmidt number,} \tag{4.5}$$

U_0	:	superficial velocity	[m/s],
L_{char}	:	characteristic length	[m],
$\nu = \eta/\rho$	:	kinematic viscosity	[m^2/s].

Numerous correlations for the flow around spheres, plates, cylinders, through pipes and packed beds in a broad range of flow conditions have employed the dimensionless form given in eq. (4.3), which arises from dimensional analysis of the specific system, as will be discussed in Chapter 4.2.3. The same procedure can be applied for the evaluation of mass transfer in cellular structures, if the geometric features are properly characterized.

4.2.2 Pressure drop

The pressure loss accompanying the flow of fluids around spheres, through pipes, packed columns or any kind of porous structure has been subject of intense investigation since it plays an important economic role in most engineering processes involving flow. The main objective is to get a relationship between the volumetric flow rate and the pressure drop. If velocity and pressure distributions of the system are known, the relationship may be obtained from the solution of the Navier-Stokes equation for momentum [9] as is the case of laminar flow through pipes (Hagen-Poiseuille flow).

The same problem arises here as in the case of mass transfer, where the flow is complex in porous and tortuous structures, and velocity and pressure profiles can not be easily calculated like for instance in packed beds. For this type of systems, correlations of dimensionless influencing variables are developed from experimental data for the estimation of the flow behaviour in geometrically similar systems. This method is, again, based on dimensional analysis. The dimensionless pressure drop is generally defined as the friction factor f (or ξ), which represents the energy loss due to frictional and/or drag forces divided by the kinetic energy of the fluid per unit volume:

$$f = \frac{1}{4}\frac{L_{char}}{L_{bed}}\frac{\Delta p}{(1/2)\cdot \rho \cdot U^2} = f(Re) \tag{4.6}$$

The relation between the friction factor (or pressure loss) and the Reynolds number is well studied and correlated for the flow in tubes (only friction) and around spheres (drag and friction) among other arrangements [10].

Pressure drop in packed beds

One complex system of great interest in chemical engineering is the packed column, widely used for separation processes and industrial catalytic reactions. In the randomly arranged packings of spheres or bodies of other geometries, it appears convenient to simulate the real complex structure with a simple basic structure. Two models have been proposed: the flow over a single particle or sphere, and the flow through a tube or capillary [9,11]. The tube model has shown to be more successful for the description of the pressure drop, and most correlations given in the literature are based on it. For this idealized system, the characteristic length L_{char} is the hydraulic diameter of the "tube", and the friction factor can be defined with eq. (4.6). The hydraulic diameter D_h is defined as the ratio of the cross section available for flow to the solid perimeter of the structure. For a bed of spheres, it can be calculated as follows:

$$D_h = \frac{4 \cdot A_F}{P_S} = \frac{4 \cdot V_F}{A_S} = \frac{4 \cdot \frac{V_F}{V}}{\frac{A_S}{V}} = \frac{4 \cdot \varepsilon}{S_{geo}} = \frac{4 \cdot \varepsilon}{(1-\varepsilon) \cdot \frac{6}{D_p}} = \frac{2}{3} \cdot \frac{\varepsilon}{(1-\varepsilon)} \cdot D_p \tag{4.7}$$

with

A_F	:	void cross section area	[m^2],
P_s	:	wetted solid perimeter	[m],
V_F	:	void volume	[m^3],
A_S	:	geometric solid surface area	[m^2],
ε	:	porosity	[-],
S_{geo}	:	geometric surface per bed volume	[m^2/m^3],
D_p	:	sphere diameter	[m].

From eqs. (4.6) and (4.7), the friction fraction can be determined from experimental data, leading to the Ergun equation [12]:

$$\frac{\Delta p}{L_{bed}} = 150 \cdot \frac{(1-\varepsilon)^2}{\varepsilon^3} \cdot \frac{\eta}{D_p^2} \cdot U_0 + 1.75 \cdot \frac{(1-\varepsilon)}{\varepsilon^3} \cdot \frac{\rho}{D_p} \cdot U_0^2 \tag{4.8}$$

The dependence to the porosity in the equation arises from the definition of the hydraulic diameter for the packed bed (eq. (4.7)) and from the use of the interstitial velocity of the fluid as the characteristic velocity magnitude: $U = U_0/\varepsilon$. This mathematical relation was found to correlate satisfactorily the pressure drop of granular solids of different size and shape with bed porosities near 40 % over a wide hydrodynamic range. The Ergun equation has also been the basis of the evaluation of pressure drop data for ceramic and metallic sponges published in recent years [13-15]. Nevertheless, it seems more reasonable in this case to use the generalized equation for flow through porous media denoted as the Forchheimer equation [11]:

$$\frac{\Delta p}{L_{bed}} = \frac{\eta}{k_1} \cdot U_0 + \frac{\rho}{k_2} \cdot U_0^2, \tag{4.9}$$

where k_1 and k_2 are the permeability parameters of the structure dependent on the porosity and the characteristic length of the structure. The dependence of the k-values on the structure of a sponge is not necessarily the same as in the Ergun equation, since their morphologies differ considerably from those of packed beds. The values of both permeability parameters and their dependence on porosity and pore size can be obtained from experimental pressure drop measurements and, if possible, correlated to give an overall relation for sponges with different geometric features.

4.2.3 Dimensional analysis and analogies

Every physical phenomenon is determined by a series of influencing variables. The relations of the characteristic parameters to the phenomenon are represented as functional equations, usually differential equations. As described in the previous chapter, it is often not possible to solve the problem by analysis and calculation since the mathematical difficulties are too great when the physical problem is very complex. In such cases, the investigation of the problem has to begin with finding out the important physical properties and developing mathematical relations which govern the phenomenon. This approach can be realized by dimensional analysis and similarity theory [16]. In the study of problems depending on a large number of parameters, dimensional analysis is especially valuable in reducing the number of independent variables by defining dimensionless relations between influencing parameters and determining which of the variables are not significant. The evaluation and comparison of experimental data of the complex geometries analyzed in this work will be therefore based on dimensional analysis, which will be explained briefly.

Functional relations between physical quantities: The Π-Theorem

The fundamental units of measurement in engineering are length, time, mass, temperature, electric current and light intensity. The units of measurement (or dimensions) of all other quantities are obtained from the fundamental units. The functional relations characterizing the physical problem established theoretically or from experiments represent physical laws, and the numerical values of these dimensional physical quantities depend completely on the choice of a system of units of measurement, which has actually no connection with the nature of the phenomenon. Functional relations expressing physical facts in a general way, independent of units, must have a dimensionless form. This is the basis of the Π-Theorem, or Buckingham-Theorem, that asserts that any dimensional physical relation can be represented as one substituting between a set of dimensionless independent products (Π-products) of the measures of the influencing quantities (Appendix F) [17]. The applicability of the Π-Theorem will be approached to briefly by a relevant case of mass transfer directly related with this contribution.

Mass transfer in a packed column

In a first necessary analysis, all influencing arguments have to be specified. In a packed bed of ideal spheres, if the ratios D_{tube}/D_p and L_{bed}/D_p are infinite, the only characteristic geometric parameters for the problem are D_p and the bed porosity ε. The data would consist of

- fluid properties	:	η, ρ, D_{ij},
- geometry	:	D_p, ε (ideal infinite bed),
- boundary conditions:	:	$U_{0,z}$ (or $U_{0,z}/\varepsilon$) (one dimension).

The analyzed property is the net mass transfer coefficient k_m (eq. (4.2)) from the bulk of the fluid to the solid surface of the particles in the column:

$$k_m = f(\eta,\rho,D_{ij},D_p,\varepsilon,U_0) \tag{4.10}$$

One solution from dimensional analysis is:

$$\frac{k_m \cdot D_p}{D_{ij}} = F_1\left(\frac{U_0 \cdot D_p \cdot \rho}{\eta},\frac{\eta}{\rho \cdot D_{ij}},\varepsilon\right) = F_1(Re,Sc,\varepsilon)\ (= Sh) \tag{4.11}$$

Another possible dimensionless solution also referred to as the Stanton number is the ratio between mass transfer coefficient and velocity:

$$\frac{k_m}{U_0} = F_2(Re,Sc,\varepsilon)\ (= St) \tag{4.12}$$

The number of arguments in F_i is hereby reduced to three Π-Products. Based on this result of dimensional analysis, the heat and mass transfer in packed beds has been widely investigated experimentally during the past six decades [3,10,11]. The dependence of St and Sh on the fluid properties (Sc) has been found to be well represented by $St \propto Sc^{-2/3}$ and $Sh \propto Sc^{1/3}$ respectively [7,18]. This is readily understood by the definition of both dimensionless mass transfer coefficients:

$$St = \frac{k_m}{U_0} = \frac{k_m \cdot D_p}{D_{ij}} \cdot \frac{\eta}{D_p \cdot U_0 \cdot \rho} \cdot \frac{D_{ij} \cdot \rho}{\eta} = Sh \cdot \frac{1}{Re \cdot Sc} \propto Sc^{-2/3} \tag{4.13}$$

From this dependence stems the definition of the Chilton-Colburn- or j_D-factor:

$$j_D = \frac{k_m}{U_0} \cdot Sc^{2/3} = \frac{Sh}{\mathrm{Re} \cdot Sc^{1/3}} = F_3(Re,\varepsilon) \tag{4.14}$$

The dependence of the j_D-factor (or Sh) on Reynolds number and porosity has been extensively evaluated [3,7]. The agreement is not always satisfactory since the experimental methods, the hydrodynamic conditions and the form of the particles (L_{char}) varied considerably. Nevertheless, correlations with acceptable agreement of results have been proposed. The most widely accepted general solution of the physical problem is the one proposed by Dwivedi and Upadhyay [3], who evaluated several hundred data points from different authors (eq. (4.15)).

$$j_D = 0.4548 \cdot \frac{Re^{-0.407}}{\varepsilon} \quad \underline{\text{or}} \quad Sh = 0.4548 \cdot Sc^{1/3} \cdot \frac{Re^{0.593}}{\varepsilon} \quad (10 < Re < 15000) \tag{4.15}$$

Analogies between mass, heat and momentum transfer

The close similarity of the phenomenon of mass, heat and momentum transfer in fluids is suggested by the fact that the basic equations describing the fluxes have the same form, making it possible to apply an analysis of one of the phenomena to the other two, when geometry and boundary conditions are equivalent:

$$J_A = -D_{AB} \cdot \frac{dC_A}{dy} \text{; Fick} \tag{4.1}$$

$$q = -\lambda \cdot \frac{dT}{dy} \text{; Fourier} \tag{4.16}$$

$$\tau = -\eta \cdot \frac{dU_x}{dy} \text{; Newton} \tag{4.17}$$

with

q	:	heat flux density	[W/m^2],
λ	:	thermal conductivity	[W/(m·K)],
τ	:	shear stress	[N/m^2].

A method for applying the analogy of transport phenomena was proposed by Chilton and Colburn, based on the "modified Reynolds-Analogy" between heat (and mass) transfer and fluid friction [18]:

$$j_H = \frac{h}{c_p \cdot \rho \cdot U_0} \cdot Pr^{2/3} = \frac{f}{2} = F(Re) \tag{4.18}$$

where

h : heat transfer coefficient $[\mathrm{W/(m^2 \cdot K)}]$,

c_p : heat capacity $[\mathrm{J/(g \cdot K)}]$,

f : "skin" friction factor [-],

Pr : Prandtl number = $\frac{\eta \cdot c_p}{\lambda}$ [-].

The "modified Reynolds analogy" holds for fully turbulent flow in tubes and parallel to plane surfaces, but doesn't apply for flow across tubes or other geometries, where form drag becomes decisive at higher *Re*. From the evaluation and testing of well-substantiated correlations for heat transfer on mass transfer data, the authors suggested that, due to the close relation between the nature of thermal and molecular diffusion, "the heat transfer factor j_H could also be used for estimating coefficients for transfer of material by diffusion". The Chilton-Colburn heat and mass transfer factors show equivalency ($j_D = j_H$) over the whole Reynolds range for very different types of flow:

$$j = \frac{k_m}{U_0} \cdot Sc^{2/3} = \frac{h}{c_p \cdot \rho \cdot U_0} \cdot Pr^{2/3} = F(Re) \tag{4.19}$$

or written in the Sherwood-Nusselt equivalent relation:

$$\frac{\mathrm{Sh}}{\mathrm{Re} \cdot \mathrm{Sc}^{1/3}} = \frac{\mathrm{Nu}}{\mathrm{Re} \cdot \mathrm{Pr}^{1/3}} \tag{4.19)-b}$$

The Chilton-Colburn equation is the most accepted quantitative description of the discussed analogy and has proven to be useful for the prediction of heat- from mass transfer or vice versa upon flow through packed beds, around cylinders and in tubes [9]. The analogy between mass and heat transfer is valid when the influence of radiation is negligible.

In recent years, a new type of analogy between momentum transfer due to friction and form drag (or pressure drop) and mass (or heat) transfer has been proposed by Martin [19]. It may be used for external (around cylinders) and internal (through tube bundles) flow. The analogy is based on the theoretically derived heat transfer equation of Lévêque for a developing thermal boundary layer in a fully developed laminar flow in tubes:

$$Nu = 1.615 \cdot (Re \cdot Pr \cdot D_t/L)^{1/3} \tag{4.20}$$

The equation can be generalized for the case of turbulent flow as long as the boundary layer remains within the viscous sublayer. Substituting *Re* from the Hagen-Poiseuille law for fully developed laminar tube flow, $Re = 16/f$ (or Re = Hg/32), yields the so termed "generalized Lévêque equation" [20].

$$Nu = 0.404 \cdot (2 \cdot \mathrm{x_f} \cdot Hg \cdot Pr \cdot D_h/L)^{1/3} \tag{4.21}$$

with

x_f	:	fraction of the total pressure drop due to friction	[-],
Hg	:	Hagen number $= 2 \cdot f \cdot Re^2 \neq F(Re)$	[-],
D_h	:	hydraulic diameter	[m],
L	:	empirical length	[m].

The equation has been slightly modified in the choice of D_h and L, depending on the phenomena studied [19,20]. The frictional fraction of total pressure drop x_f contributing to heat or mass transfer according to the Lévêque analogy was found to be constant over a wide Reynolds range, but can vary from 0.2 to 0.5 depending on the geometry used. Martin [19] recommends $x_f = 0.5$ for practical applications.

Even though the Lévêque-equation was defined for the entry region of a tube, this analogy has been proven to apply for the qualitative prediction of heat and mass transfer coefficients from pressure drop data in the cross corrugated channels of heat exchangers, in packed beds, in crossed rod matrices and other spacewise periodic arrangements. The applicability most probably arises from the fact that, in complex geometric arrangements, the thermal and viscous boundary layers are repeatedly developing and interrupted during flow through or around the structure. From this perspective, it can be anticipated that the Lévêque analogy holds for cellular structures as well.

4.3 Experimental

The selection of sponges and structures used for comparison was presented in the previous chapter together with the geometric features of these carriers.

4.3.1 Mass transfer properties of ceramic sponges, beads and honeycombs

A suitable method for measuring external mass transfer properties from the bulk of the gas phase to the solid surface of a geometric structure is to quantify the effective rate of a chemical reaction catalyzed by the solid surface under conditions where mass transfer is the slowest and, therefore, rate limiting step of the process. The reaction chosen was the oxidation of carbon monoxide in air. The catalytic system Pt/SnO_2, here used as a washcoat on the sponge surface, is highly active in the CO oxidation and allows for mass transfer control at moderate temperatures. Preliminary kinetic experiments at different temperatures (chapter 2) showed that at 220 °C mass transfer control is reached for all sponges at the highest Reynolds numbers. In case of the honeycomb, external diffusion control was reached already at 170 °C, whereas the 1.5 mm beads required temperatures up to 250 °C to reach complete mass transfer limitation.

After finding out the optimum conditions (15.5 MPa; 80 °C) for supercritical deposition of Pt on SnO_2, all used structures were loaded with tin dioxide and subsequently with platinum following the method developed in chapter 2.

4.3.1.1 Process system, reactor packing and system balance

Mass transfer rates through Pt/SnO_2 coated sponges were measured in a differential plug flow reactor with external recycling. A detailed description of the experimental apparatus, the reactor packing of sponges and the system balance is given in chapters 2.2.6 and 2.2.7. The reactor loading of spherical beads was performed by homogeneously packing a 30 cm bed of blank ceramic spheres until the middle of the reactor, between the glass joints for the thermocouples, carefully placing the catalytic beads (same geometry) on the blank beads preventing their accumulation on the reactor wall, and subsequently placing a second 30 cm bed of blank spheres to ensure characteristic flow through the whole bed. In the case of the 400-CPSI honeycomb carrier, extreme care had to be taken to ensure the perfect continuity of the channels in order to avoid turbulences at the entrance region of the catalytic middle piece, substantially influencing the hydrodynamic- and with it, the mass transfer phenomena through the bed [21].

The CO inlet concentration was varied between 1000 and 2000 vol.-ppm. At a constant system gas hourly space velocity (GHSV) of approx. 300,000 h^{-1}, the hydrodynamic conditions along the catalyst bed could be varied by altering the frequency of the pump and hence, the recycle flow rate (5 – 200 l/min), measured with M&W low-Δp mass flow meter. The kinetic coefficients of the CO oxidation in the mass transfer controlled regime were measured at superficial velocities between 0.2 and 12 m/s, at reactor conditions (220°C).

To correctly calculate the rate coefficients of mass transfer, depending only on the hydrodynamic behaviour of the gas flow through the sponges, a mass balance has to be made over the whole recycle system. A detailed description of the equations describing the process system is given in chapter 2.2.7. The rate coefficient as a function of the measured quantities reads:

$$k_v = \frac{(1+R)}{\tau} \cdot \ln\left(\frac{1+R \cdot (1-X_{CO})}{(1+R) \cdot (1-X_{CO})} \right) \tag{2.7}$$

with

R : recycle ratio: $\dot{V}_{recycle} / \dot{V}_0$ [-],

X_{CO} : system CO conversion [-],

τ : residence time: $V_B / \dot{V}_0$ [s].

When analyzing the mass transfer coefficients at different hydrodynamic conditions, the recycled flow rate and with it, the deviations of the real system from CSTR are varied. The deviations from CSTR can be easily calculated by dividing the real rate coefficient k_v by the coefficient at ideal CSTR conditions $k_{v,CSTR}$:

$$k_{v,CSTR} = \frac{1}{\tau} \cdot \frac{X_{CO}}{1 - X_{CO}} \tag{4.22}$$

giving:

$$\frac{k_v}{k_{v,CSTR}} = \frac{(1+R) \cdot (1 - X_{CO})}{X_{CO}} \cdot \ln\left(\frac{1 + R \cdot (1 - X_{CO})}{(1+R) \cdot (1 - X_{CO})} \right) \tag{4.23}$$

At recycle flow rates below 25 and/or conversions above 80 %, the deviations from CSTR are considerable (>10 %) [22]. For this reason eq. (2.7) was taken for calculating the rate coefficients, independently of the flow regime being analyzed.

4.3.2 Pressure drop through sponges, beads and honeycombs

The pressure drop was measured using the same apparatus. For this purpose, the upper and lower ends of a cylindrical sponge piece of 50 mm were removed, since these showed increased blockage of pores due to the manufacturing process. The sponge was then wrapped in glass fabric and pressed into a glass reactor with two lateral glass tubes placed 12 mm above and below the packed sponge (Figure 4.2). The assembly of the reactor was the same as described in chapter 2. The pressure drop was measured with a water manometer at superficial velocities up to 15 m/s. The gas temperature was kept constant at 220 °C in order to achieve the same hydrodynamic conditions as in the mass transfer experiments for a better comparison of both properties. The packing of the honeycomb was performed with the same procedure. For measuring pressure drop through packed spheres, a 70 mm bed of blank beads was packed in the middle of the tube between sponge pieces of low pore density for mechanical hold.

In contrast to the mass transfer experiments, the recycle system was opened to atmospheric pressure, i.e. the intake- and pressure side of the recycle pump were opened to atmosphere, leaving as the experimental setup merely a packed, heated tube with a controlled gas flow and a water manometer. Previous measurements revealed that leaving the closed recycle system lead to considerable deviations in the pressure drop values of a given sponge piece due to under-atmospheric pressures in the effluent region of the reactor, prior to the entrance of the pump.

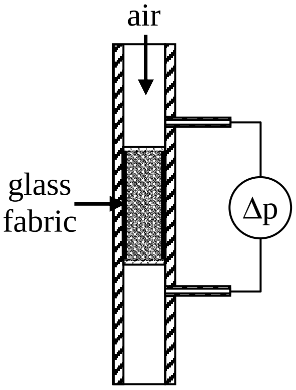

Figure 4.2: Packed glass tube for pressure drop measurements.

4.3.2.1 Practical considerations

The first attempt for measuring the pressure drop of the sponges was to use the same packed catalytic bed after the mass transfer experiments by simply replacing the thermocouples with the water manometer. Comparison with results from the literature and lack of reproducibility gave a first impression of the unsuitability of the method for reliable values of the pressure drop. A new glass tube had to be constructed, with lateral glass tubes being further away from each other (60 mm). Measuring the pressure drop directly at the axial position were the sponge packing was placed lead to considerable higher pressure drop values than the actual pressure drop per bed length. The holes made in the glass fabric along the sponge bed in order to measure the pressure drop most probably caused a bypass flow from the measuring axial positions to the positions at the entrance and outlet of the wrapped sponge pieces, somewhat over and under the lateral glass tubes, respectively. If this is the case, the length used for the calculation of the pressure drop per bed length was shorter than the actual length where the static pressures are being measured, leading to erroneous values for the pressure drop. First experiments using the same sponge piece with different packing methods and experimental procedures regarding the recycle finally gave insight to the correct measuring method and confirmed the suppositions presented above. Therefore, great attention should be paid to the experimental procedure regarding the analysis of the pressure drop, since even though the principle is quite simple, many influencing factors can significantly hinder the correct evaluation of this important property.

4.4 Results and discussion

The mean SnO_2- and Pt-contents of the structures used are presented in Table 4.1. The tin dioxide content of the sponges increases with increasing geometric surface or pore density, respectively, as would be expected from a SnO_2 layer of constant thickness. The ratio of Pt to SnO_2 remains nearly constant at about 10 %, suggesting that platinum adsorbs exclusively on the tin dioxide washcoat. Image analysis of the sponges, beads and honeycomb before and after wash coating showed negligible variation (< 2 %). A variation of the mean pore diameter D_p of the sponges upon coating could not be detected, and the reduction in porosity was lower than 3 %. The rather high SnO_2 coverage of the beads was necessary to obtain a homogeneous washcoat on the geometric surface area since the alumina matrix, from which these structures were made, was not sufficiently sintered by the manufacturer (BET – surface area = 9 m^2/g).

Table 4.1: SnO_2 and Pt loadings of the structures used.

Catalyst	**SnO_2** [wt.-%]	**Pt** [wt.-%]	**Pt/SnO_2** [%]
10PPI_0.8	3.8	0.52	13.7
20PPI_0.8	4.3	0.43	10.0
30PPI_0.8	5.3	0.51	9.7
45PPI_0.8	7.3	0.71	9.7
10PPI_0.85	3.3	0.38	11.3
20PPI_0.85	6.4	0.54	8.5
30PPI_0.85	7.1	0.60	8.5
45PPI_0.85	8.9	0.86	9.7
20PPI_0.75	4.5	0.43	9.6
M-40PPI_0.95	6.3	0.52	8.3
HC 400-CPSI	9.5	0.94	9.9
Beads 3.3 mm	19.9	1.92	9.65
Beads 1.5 mm	19.4	2.12	10.93

The relevant geometric features and porosities of the structures under investigation are presented in Tables 3.1 and 3.2 of the previous chapter.

4.4.1 Mass transfer coefficients

4.4.1.1 Mass transfer coefficients of ceramic sponges

Figure 4.3 displays the volumetric mass transfer coefficients of the sponges with pore densities between 10 and 45 PPI and a total porosity of 85 % as a function of the superficial gas velocity. Different shadings of one symbol type denote different catalytic pieces of the same type. Due to the irregular nature of these structures, deviations between samples were expected. The deviations are small but increase with increasing pore count from ± 3 % (10-PPI) to ± 7 % (45-PPI) in parallel with the inhomogeneities of the bulk density observed on the sponge bodies provided by the manufacturer (chapter 3). For this reason, three to four different sponge samples of every sponge type were measured in order to gain representative values for their mass transfer properties.

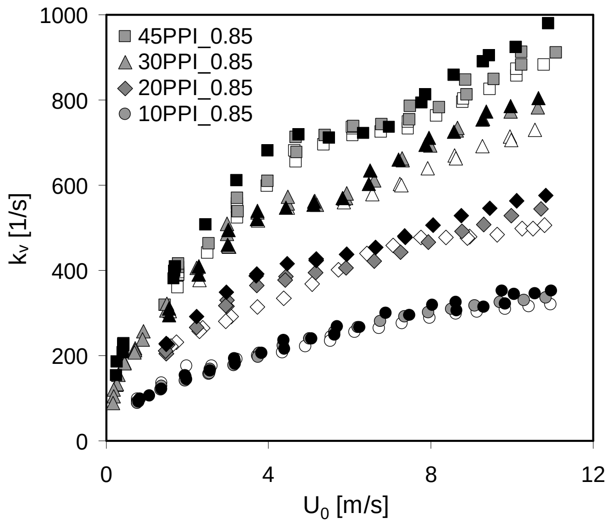

Figure 4.3: *Volumetric mass transfer coefficients k_v of sponges (ε =0.85) versus superficial gas velocity.*

As expected from the external mass transfer control, the rate coefficients increase with increasing superficial velocity: $k_v \sim U_0^{(0.4\ -\ 0.52)}$. The values of the volumetric coefficients increase with decreasing pore size since the geometrical surface area per bulk volume increases as well (Table 3.2). A higher amount of CO can be converted in the same volume of a 45 PPI sponge than in a 10 PPI sponge. The sponges with lower porosity showed the same tendency and very similar values to the sponges with 85 % porosity.

With the geometrical surfaces S_{geo} from MRI-analyses, the mass transfer coefficients (k_m) could be calculated from volumetric coefficients with eq. (4.24):

$$k_m = \frac{k_v}{S_{geo}} \tag{4.24}$$

The ceramic sponges exhibit similar mass transfer coefficients over the whole velocity range even though the surface areas differ considerably, as is exemplarily shown in Figure 4.4. The dependence of the mass transfer coefficients on the superficial velocity is slightly higher for sponges with larger pores (10- and 20-PPI) than for the other two pore densities. The same tendency was observed by Schlegel et al. [23] when measuring heat transfer coefficients on cordierite sponges with pore counts very similar to those used in our work. The authors found similar heat transfer coefficients for all sponges in a range of 0.5 – 14 m/s, as well as increasing U_0-exponents with increasing pore size.

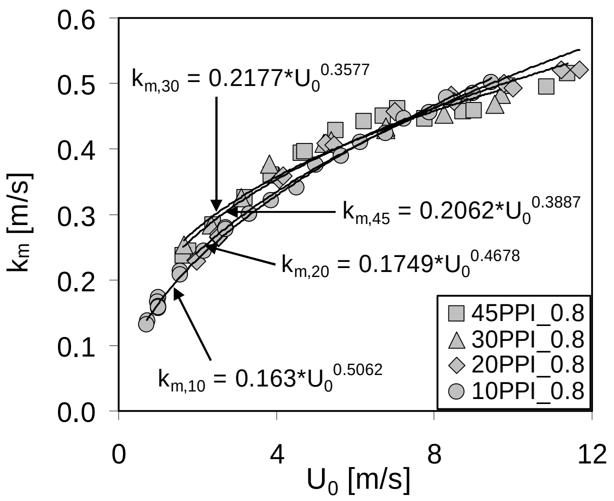

Figure 4.4: Mass transfer coefficients k_m of sponges with 80 % porosity versus superficial gas velocity.

The influence of the porosity is rather weak within the analyzed range. The mass transfer coefficients of the 20-PPI sponges increase slightly with the porosity at a constant interstitial velocity. Figure 4.5 depicts the average k_m-slopes of 20-PPI sponges with three different porosities versus the interstitial velocity U_0/ε_h. Nevertheless, in singular cases (a specific sample) the values for k_m were slightly higher at a lower porosity. The small differences of the slopes shown in the figure just give the observed tendency. No definitive conclusion regarding the influence of the porosity can be made from these results.

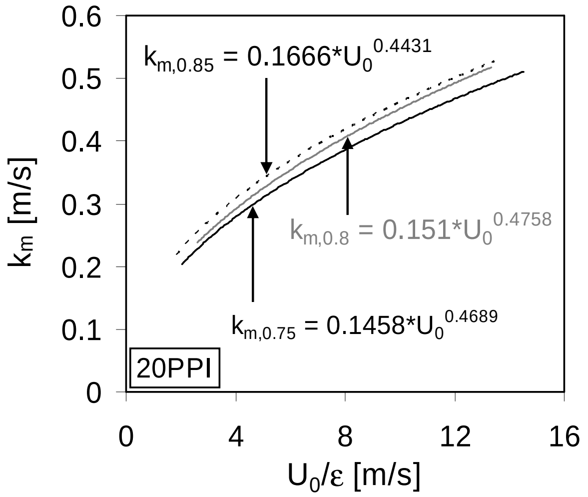

Figure 4.5: Mass transfer coefficients k_m of 20-PPI sponges with 75, 80 and 85 % porosity over the interstitial gas velocity.

Excluding the dependence of the mass transfer properties of sponges on reactor diameter and length of catalyst bed is essential for the applicability of the results given in this work. For this reason, different sponge-sample diameters and lengths were chosen for the sponges of types 20-PPI_0.8 and 30-PPI_0.8. Two reactor diameters as well as three bed lengths were chosen: 15 and 25 mm, and 14, 25 and 50 mm, respectively. The influence of both parameters turned out to be negligible as can be seen exemplarily in Figure 4.6. The volumetric mass transfer coefficients show similar values. The deviations are smaller than 10 %, within the deviations found upon measurements of different sponge samples of the same type. Therefore, it can be concluded that, within the evaluated range, the characteristic flow of the analyzed sponges is fully developed, and the mass transfer properties are not dependent on the reactor geometry.

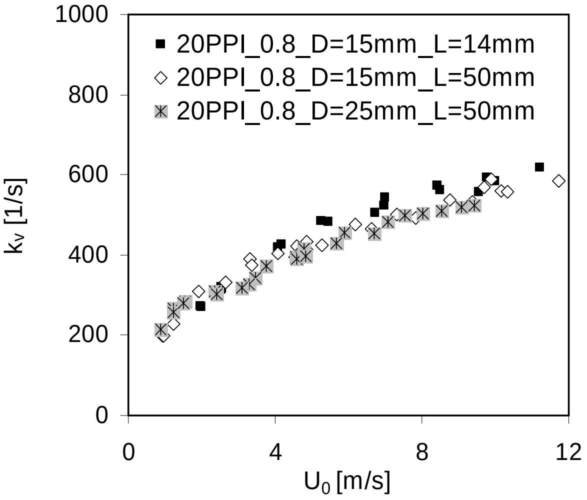

Figure 4.6: Volumetric mass transfer coefficients of 20 PPI_0.8 sponges with different dimensions.

4.4.1.2 Structure comparison

The mass transfer coefficients of the analyzed beads and honeycombs are plotted in Figure 4.7 together with data of three sponges having, as far as possible, similar geometric surface areas. When evaluating the different structures with the highest surfaces areas, namely the 1.5 mm beads, the 400-CPSI honeycomb and the 45-PPI sponge, a definite trend is recognizable in the values of the mass transfer coefficients, namely: beads > sponge > honeycomb. Even though the honeycomb has the highest geometric surface area of all analyzed structures, it actually displays the poorest mass transfer performance (per bed volume and per surface area) among all carriers. The mass transfer coefficients of the 20-PPI sponges (different porosities show similar values) and the 3.3 beads are very similar at nearly equal S_{geo}. The volumetric rate coefficients of sphere packings increase in a stronger manner with increasing S_{geo} as compared to the sponges. This can be better understood, when comparing the mass transfer coefficients k_m of sponges and beads. While the mass transfer coefficients of sponges in a wide range of S_{geo} remain nearly constant, the mass transfer coefficient of a sphere (single or in a packing) increases with increasing S_{geo} (or decreasing diameter), as can be seen in the right plot of Figure 4.7.

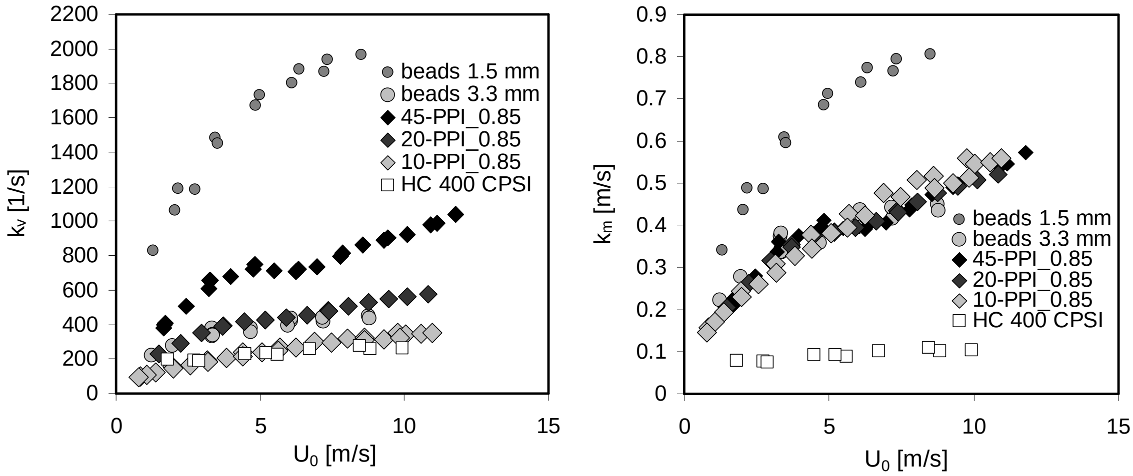

Figure 4.7: Volumetric (left)- and surface area-related (right) mass transfer coefficients as a function of the superficial gas velocity over different carrier structures.

A dimensional analysis provides a more significant description of the mass transfer properties since it includes all parameters influencing the phenomenon.

4.4.1.3 Dimensional analysis: dimensionless evaluation of the results

The relevant physical magnitudes for a dimensional analysis of the mass transfer through a packed bed of spheres were defined in chapter 4.2.3. From the data describing the phenomenon, the fluid properties and boundary conditions are the same in the case of sponges and honeycombs. The geometry and the porosity are the varying parameters when comparing these structures. The choice of characteristic length is arbitrary to some extent for each geometry. None the less, when comparing different geometries in the non dimensional form, the same geometric feature should be taken for definition of Reynolds- and Sherwood numbers (cf. chapter 4.2.1). The most adequate choice of length is $(S_{geo})^{-1}$. Sherwood then represents the rate of mass transfer per geometric surface area of a given structure.

Analog to eq. (4.11), Sherwood- and Reynolds numbers can be defined for the three structures, beads, sponges and honeycombs:

$$Sh^* = \frac{k_m}{D_{ij} \cdot S_{geo}} = F^*\left(\frac{U_0 \cdot \rho}{\eta \cdot S_{geo}}, \frac{\eta}{\rho \cdot D_{ij}}, \varepsilon\right) = F^*\left(Re^*, Sc, \varepsilon\right) \tag{4.25}$$

The mass transfer performance per surface area (Sh^*) over Re^* of the carriers, representing the surface area-based hydrodynamic conditions, are displayed in the left plot of Figure 4.8. The 400-CPSI honeycomb shows by far the poorest mass transfer performance at constant hydrodynamic conditions and surface area. The mass transfer properties of spheres and sphere packings can be described with a single characteristic length, the particle diameter. In contrast, the slopes of the three different sponges used in the figure show a systematic difference in both plots. The mass transfer coefficients per surface area increase with increasing cell size. While the 20- and 45-PPI sponges have slightly lower Sh^* values than the beads, the slope of 10-PPI sponge is slightly above the Sh^*-Re^*-slope of the beads. The mass transfer performance of sponges is in the range of that of packed spheres.

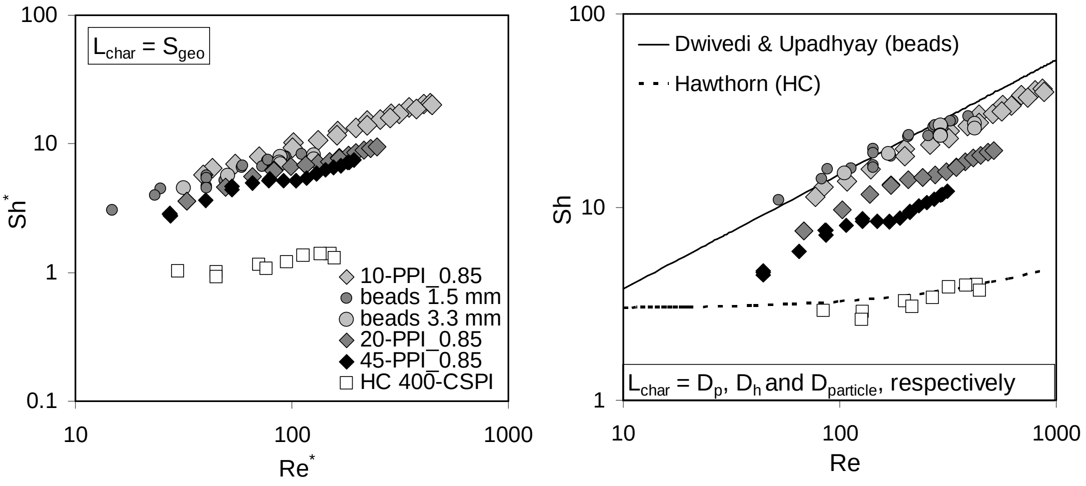

Figure 4.8: Left: mass transfer versus hydrodynamic properties (Sh^*-Re^*) of the bead packings, the honeycomb and the three sponges based on their respective geometric surface area. Right: same data using the pore diameter (D_p), the hydraulic diameter (D_h) and the particle diameter ($D_{particle}$), respectively, as the characteristic length for dimensional analysis: lines represent literature relations for honeycombs [4] and bead packings [3].

To ascertain the quality of the experiments and to validate the correctness of the mass transfer coefficients, the data obtained from honeycomb and beads are plotted together with literature correlations for *Sh* in these fixed beds in the right diagram of Figure 4.8. There, the characteristic lengths were defined as usual in the literature, namely as the particle diameter for the spheres, the hydraulic diameter for the honeycombs and the pore diameter for the sponges. The trend remains the same as in the left plot, since these three last features are strongly related to the surface area of the structure. There is a very good fit between the data and the correlation of Dwivedi & Upadhyay for particle beds (eq. (4.15)) [3]. The agreement between the experimental data of the honeycomb and the theoretical relation developed by Hawthorn [4] (eq. (4.26)) is also satisfactory.

$$Sh = 2.976 \cdot \left(1 + 0.078 \cdot Re \cdot Sc \cdot \frac{D_h}{L}\right)^{0.45} \tag{4.26}$$

In this relation, L, the length of the monolith, is a second influencing geometric parameter that has to be included in the dimensional analysis to correctly describe this structure. For long catalytic honeycombs, the mass transfer coefficients are independent of the hydrodynamic conditions, leading to the asymptotic value of approx. 3. In this work, however, the honeycomb monolith had a length of 35 mm, leading to the slightly increasing slope of the correlation at higher *Re* (Figure 4.8 (right)).

The dimensionless mass transfer data (*Sh*) of all ceramic sponges used in this work with the pore diameter D_p as the characteristic length (eq. (4.28)) can be expressed in terms of the hydrodynamic properties, or *Re* (eq. (4.29)) as:

$$Sh = A \cdot Re^{B} \cdot Sc^{1/3} \tag{4.27}$$

$$Sh = \frac{k_m \cdot D_p}{D_{AB}} \tag{4.28}$$

$$Re = \frac{U_0 \cdot D_p}{\nu} \tag{4.29}$$

The diffusion coefficient of CO in air, $D_{AB} = D_{CO,air}$, amounts to 4.1 – 4.5 × 10^{-5} m^2/s at system gas temperature, depending on the variations in pressure. Figure 4.9 shows exemplarily one set of experimental *Sh*-*Re* data for each sponge type. Since the fluid properties were kept constant, the *Sc*-number is not included in the figure. The minimum superficial velocity in the operation modus with external recycle was 1.2 m/s. For this reason, two sponges (30PPI_0.85 and 45PPI_0.85) were tested in a plug flow without recycle to extend the velocity range towards lower values. The conversion data in this case were transformed into kinetic rate constants by using the PFR reactor model:

$$k_{v,PFR} = -\frac{1}{\tau} \cdot \ln(1 - X_{CO}) \,. \tag{4.30}$$

The minimum superficial velocity was 0.2 m/s since the CO conversions were higher than 90 % at lower velocities (higher residence time).

The Sherwood numbers of the sponges increase with the size of the pores. The values for the constants A and B (eq. (4.27)) found for each sponge type (3 data sets for every sponge type) are listed in Table 4.2. As discussed above, the mass transfer properties of sponges can not be uniquely described with hydrodynamic and fluid properties alone.

From dimensional analysis it becomes clear that an additional, not yet considered geometric influence has to be searched for and included in the evaluation of the data.

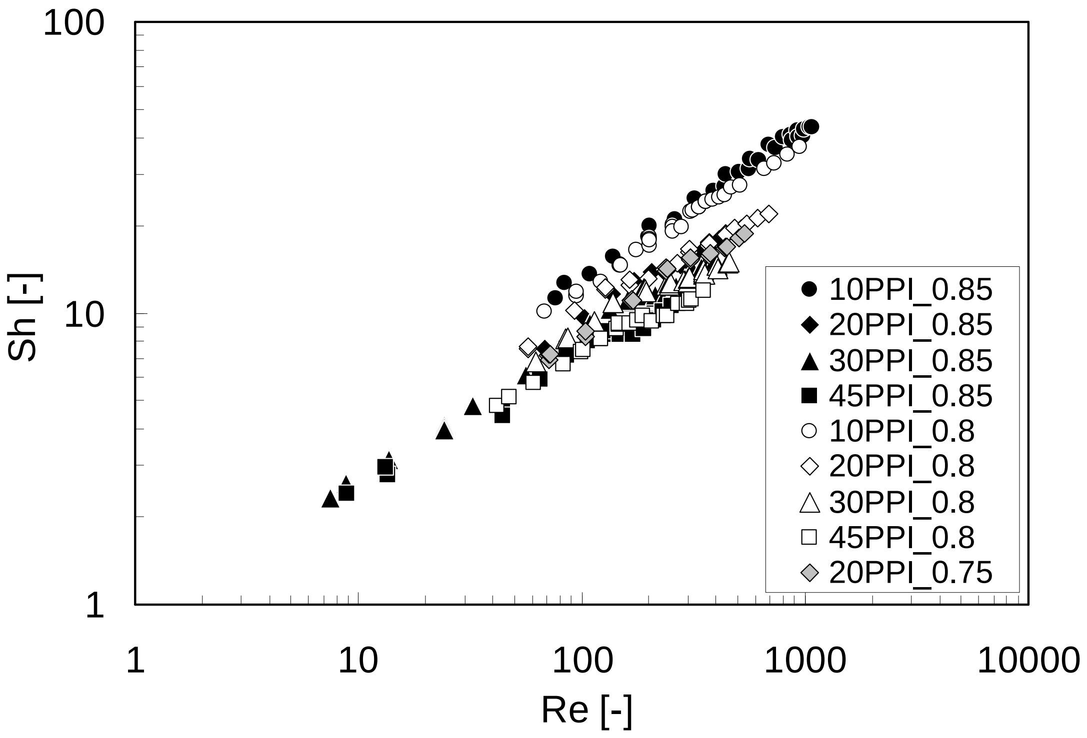

Figure 4.9: Experimental Sh-numbers as a function of the Re-numbers of nine different sponge types; circles: 10PPI, diamonds: 20PPI, triangles: 30 PPI and squares: 45 PPI. Different shadings represent different porosities.

Table 4.2: Values for A and B in eq. (4.27) derived from the Sh vs. Re plots of the sponges.

Sponge type	*A*	*B*	*Re*-range
10PPI_0.85	1.60 ± 0.16	0.48 ± 0.02	77 - 1103
20PPI_0.85	1.26 ± 0.16	0.45 ±0.02	62 - 661
30PPI_0.85	1.15 ± 0.14	0.45 ± 0.03	7.5 - 395
45PPI_0.85	1.04 ± 0.11	0.43 ± 0.02	8.9 - 325
10PPI_0.8	1.34 ± 0.09	0.50 ± 0.01	66 – 946
20PPI_0.8	1.65 ± 0.14	0.41 ± 0.01	58 – 695
30PPI_0.8	1.21 ± 0.18	0.43 ± 0.03	54 – 507
45PPI_0.8	0.97 ± 0.13	0.44 ± 0.03	36 – 352
20PPI_0.75	1.17 ± 0.22	0.46 ± 0.03	68 - 620

4.4.1.4 Comparison with literature correlations: heat and mass transfer

When comparing with literature data for mass or heat transfer, the geometrical and material properties of the structures from the literature have to be known as precisely as possible. The geometric specifications of the authors are often insufficient, and models for calculating the geometric surface of sponges differ considerably, making a comparison difficult. For this reason, before comparing the data from this work with other publications, the information provided by the authors is considered and listed in Table 4.3. The two most representative publications with similar geometric sponge features as compared to this work were taken for comparison. Groppi et al. [2] proposed a generalized correlation for mass transfer in metallic and ceramic sponges. Four different sponges were taken there into account: three metallic sponges (Fe-Cr-alloy) from a previous publication [5], and one ceramic sponge (α-Al_2O_3) with a pore count of 8.2 PPI (Table 4.3). The correlation proposed used the strut diameter as the characteristic length and the maximum interstitial velocity between struts for Re-definition:

$$Sh = 0.91 \cdot Re_{max}^{0.43} \cdot Sc^{1/3} \tag{4.31}$$

with

$$Sh = \frac{k_m \cdot d_t}{D_{CO,air}}, \tag{4.32}$$

$$Re_{max} = \frac{U_{max} \cdot d_t}{\nu}, \tag{4.33}$$

$$U_{\max} = \frac{U_0}{\left[1 - \frac{2}{\sqrt{3\pi}} \sqrt{1-\varepsilon}\right]^2}. \tag{4.34}$$

To compare the data from Groppi et al. with own data, the correlation (eq. (4.31)) has to be redefined with the pore diameter of the cubic cell and the superficial velocity in *Sh* and *Re*. The correlation of Groppi et al. is in good agreement with the mean *Sh*-values of the 10-PPI sponges applied in this work (Figure 4.10) since those authors used mainly sponges with large pore sizes (8 – 15 PPI). Although the geometric features of the system, such as the sponge diameter and length (Table 4.3) as well as the procedure of reactor loading differed considerably, the obtained values of *Sh* match satisfactorily. The *Sh*-*Re* slopes from this work displayed for comparison in Figure 4.10, result from the mean values of the constants *A* and *B* for each sponge type.

Table 4.3: Geometric properties of sponges analyzed in the quoted literature.

mat.	**[PPI]**	**Porosity** ε_t **[-]**	$D_{p,h}$ [a] **[mm]**	d_t **[mm]**	S_{geo} **[m^{-1}]**	***Re*-exponent**	**(D_s/L_s)** [d] **[mm]/[mm]**
Groppi et al. [2] **mass transfer (*Sh*)**							
Al_2O_3	8.2	0.84	3.1 (D_p)	0.84	802 [b]	0.43	9/6-25
FeCr	5.9	0.95	4.3	0.73	336 [b]	0.43	9/6-25
FeCr	12.5	0.94	2.0	0.29	761 [b]	0.43	9/6-25
FeCr	15.3	0.93	1.7	0.23	962 [b]	0.43	9/6-25
Schlegel et al. [23] **heat transfer (*Nu*)**							
Cord.	10	0.858	5.2 (D_h)	-	667 [c]	0.47	76/150
Cord.	20	0.867	2.6	-	1334 [c]	0.43	76/165
Cord.	30	0.863	1.73	-	2001 [c]	0.42	76/153
Cord.	50	0.854	1.02	-	3335 [c]	0.27	76/150

[a] *p*: pore; *h*: hydraulic

[b] calculated from the cubic cell model

[c] manufacturer specifications (Selee) idem

[d] refers to the diameter of the sponge piece divided by its length

Schlegel et al. [23] analyzed the convective heat transfer and the pressure drop in ceramic sponges made of cordierite having similar pore densities and porosities as the sponges analyzed in this work. Since the heat transfer measurements were performed at 160 °C, radiation is negligible. So, the analogy between heat and mass transfer or the Chilton-Colburn-analogy [18] can be applied for data comparison. Despite of completely different experimental methods and ceramic materials, the authors also observed an increase in heat transfer (*Nu*) with decreasing pore count as can be seen in Figure 4.10. The dependency on Reynolds (*Re*-exponent) also increases with the size of the pores from 0.27 to 0.47 between 10- and 50-PPI indicating a higher degree of turbulence in larger pores. The *Nu*-values by Schlegel et al. are qualitatively in good agreement with the experimental *Sh*-numbers from this work. The slope of the *Sh*-plot in case of the 10-PPI sponge is similar in all cases, even though the size of the sample varies extremely from a diameter of 9 mm (Groppi) to 76 mm (Schlegel). The deviations at higher pore densities between the *Nu*-numbers reported by Schlegel et al. and the *Sh*-numbers measured herein can not be overlooked. The differences are most probably due to the different geometrical surfaces used. The authors did not specify the origin of the values for S_{geo}, but at a constant pore count, their calculated surfaces are considerably higher than the ones measured herein, as can be seen upon comparison between Table 3.2 and Table 4.3. The higher S_{geo} values result in apparently lower heat transfer coefficients and thus, lower Nu-numbers. Furthermore, the authors did not measure the actual pore diameter D_p. They defined Nu and Re via the hydraulic diameter $D_h = 4*\varepsilon/S_{geo}$, which prevents a more quantitative comparison between Sh-numbers from this work and their experimental Nu-numbers.

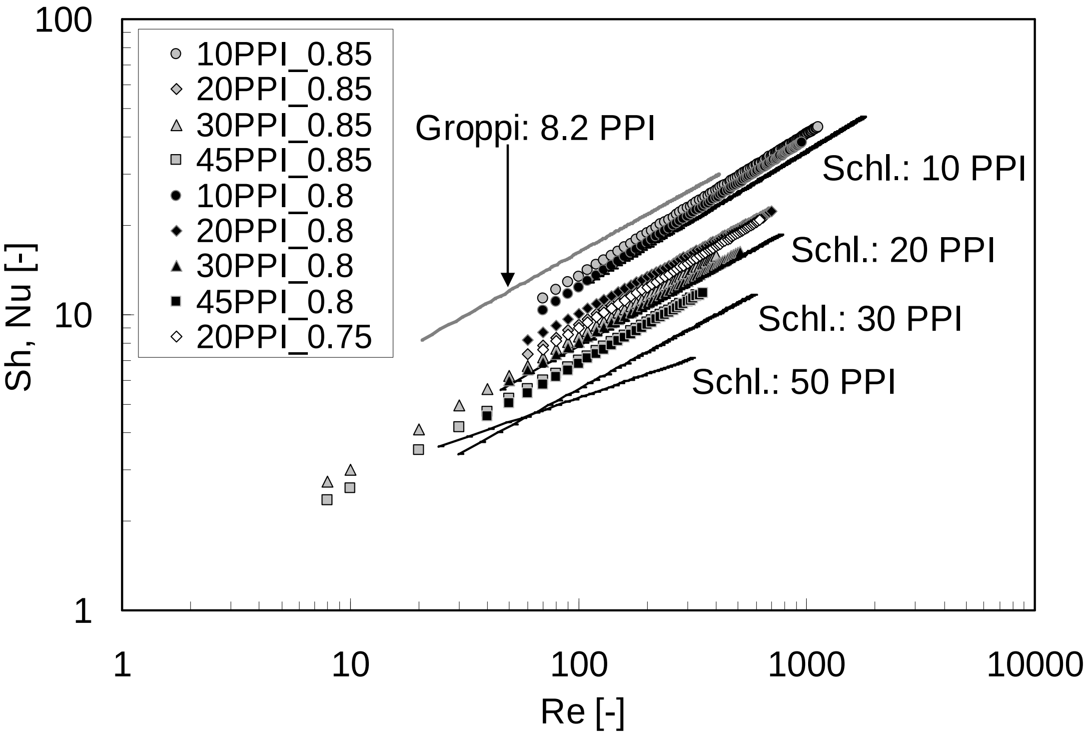

Figure 4.10: Comparison between mass and heat transfer data: this work (Sh), Groppi (Sh) [2] and Schlegel (Nu) [23].

4.4.1.5 Relation between mass transfer and hydrodynamic properties of sponges

In an attempt to find a correlation describing all sponges consistently, the additional geometric influence has to be studied.

If the sponges used here would be geometric perfectly similar structures, i.e. every dimension of the sponges would enlarge or contract by exactly the same factor, the dimensionless representation of mass transfer in sponges could be generally described with $Sh = f(Re,Sc)$. All geometric features characterized earlier were tested for correlating the mass transfer properties of the sponges: d_t, d_p, D_p and $(S_{geo})^{-1}$. The first one tested was the strut diameter, based on the good correlation achieved by Groppi et al. [2]. However, with the sponges under investigation in this work, no general description was possible based on the strut diameter as the characteristic length in Sh

and *Re*. Due to the nearly constant ratio between all these “characteristic” lengths, the use of any of them yielded the same tendency, namely different *Sh*-*Re* slopes for different sponge types, as shown in Figure 4.8, Figure 4.9 and Figure 4.10. The pore diameter perpendicular to the direction of flow was chosen as the characteristic length, since it is experimentally accessible and represents in our opinion a combination of two characteristic geometric features for the void- and solid fractions in sponges ($d_p + d_t$). In order to describe these geometrically not perfectly similar cellular materials in a more general way, an additional geometric influencing factor, defined here as F_g, has to be included in eq. (4.27):

$$Sh = A \cdot Re^{B} \cdot Sc^{1/3} \cdot F_g \tag{4.35}$$

With the firstly characterized geometric features of the sponges (Table 3.2), the anisotropy not yet included, various definitions for F_g were chosen and evaluated by parameter fitting, as will be described below.

4.4.1.6 Mathematical modelling

Fitting of the model parameters was achieved using the Matlab software. The flowchart of the parameter evaluation routine is shown in Figure 4.11. A large number of different geometric functions F_g were defined, containing different combinations of the four geometric features mentioned above and the fit parameters (m, n) as exponents. Further fit parameters were *A* and *B* from eq. (4.27). The starting values for the parameters were varied from zero to unity, showing no changes in the end values. The nonlinear minimization was done with the function “lsqnonlin”. The algorithm in this function is a trust region method based on the interior-reflective Newton method, described in [24]. With this algorithm, the confidence interval limits as well as the correlation of the estimated parameters, using the Jacobian matrix, can be calculated.

Introducing F_g simply as the ratio of the characterized lengths resulted merely in a further constant, as described above, with insignificant influence and therefore not unifying mass transfer data. The best empirically found function F_g, yielding the lowest absolute variance (0.76) and the best correlation for all sponges, was found to be:

$$F_g = \left(\frac{D_p[\mathrm{m}]}{0.001\mathrm{m}} \right)^{\mathbf{m}} \cdot \left(\varepsilon_h \right)^{\mathbf{n}} \tag{4.36}$$

The estimated parameters and their confidence intervals are listed in Table 4.4. The parameter errors were estimated by a 95 % confidence limit.

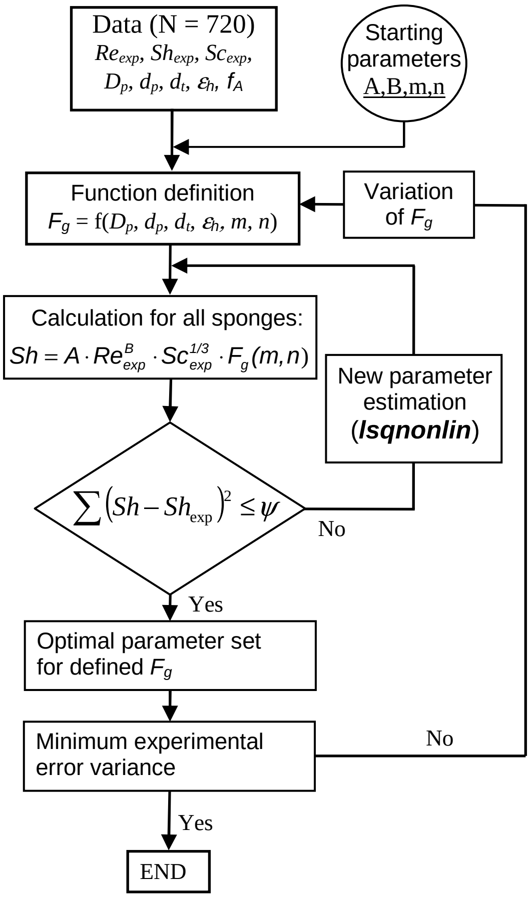

Figure 4.11: Flowchart of parameter estimation and evaluation of the geometric function. ***N*** *is the number of experimental points,* ψ *is the tolerance.*

Table 4.4: Estimated parameters for the mass transfer correlation of ceramic sponges.

Parameter	Value	Confidence interval (95 %)
A	**1.00**	± 0.05
B	**0.47**	± 0.01
m	**0.58**	± 0.01
n	**0.44**	± 0.11

It is important to know how the parameters are correlated to each other. This can be quantified by the variance-covariance matrix V obtained from the Jacobian matrix J (N × 4) and the experimental error variance Var as: $V = Var \cdot (J^T \cdot J)^{-1}$. This 4 × 4 matrix allows the calculation of the relative correlation of the parameters by dividing every element of the matrix by the square root of the product of the variances of the parameters (eq. (4.37)) i and j being the indices of different parameters.

$$C_{ij} = \frac{cov_{ij}}{\sqrt{var_i \cdot var_j}} \tag{4.37}$$

with

C_{ij}	:	element of the correlation matrix C	[-],
cov_{ij}	:	covariance between parameters i and j	[-],
var_i	:	variance of a given parameter i	[-].

Table 4.5 displays the relative correlation matrix C of the estimated parameters to each other. The diagonal elements are one, since the covariance of one parameter to itself is equal to its variance. If an element of the matrix (C_{ij}) is close to unity, the parameters i and j are strongly correlated. If the element is close to zero, the correlation of the parameters to each other is weak. Parameters A and B are strongly correlated, since for an optimum representation of the data an increase in A would result in a decrease in B in order to keep the deviation between the correlation in the data points as low as possible. The same logical relation applies for the correlation between the remaining parameters, whereas the influence of their correlation is not determining for the quality of the data representation.

Table 4.5: Symmetric correlation matrix C of the 4 estimated parameters.

	A	B	m	n
A	1	-0.770	0.020	0.643
B	-	1	-0.489	-0.035
m	-	-	1	-0.385
n	-	-	-	1

4.4.1.7 Empirical mass transfer correlation for ceramic sponges

A major attempt of this work is to find a correlation for the prediction of mass transfer properties in sponges with different geometric features, of which the user can take advantage in the simplest way possible. The introduction of (D_p/0.001m) in F_g is not physically founded, but unifies the mass transfer data collected in this work, yielding a correlation with a minimum of geometric parameters needed. This is most advantageous for the user, who would otherwise need to analyze cuts through sponge samples in all directions (3D), thereby destructing many specimen.

The following empirical correlation holds for all ceramic sponges irrespective of their porosities or pore counts, or more precisely for sponges with pore sizes D_p between 0.87 and 3.13 mm (10 to 45-PPI) and total porosities between 75 and 85 % in the Reynolds range $7 < Re < 1100$:

$$Sh = 1.00 \cdot Re^{0.47} \cdot Sc^{1/3} \cdot \left(\frac{D_p}{0.001\mathrm{m}} \right)^{0.58} \cdot \varepsilon_h^{0.44} \qquad (4.38)$$

The mass transfer data of all sponges according to this correlation are depicted in Figure 4.12 , showing no significant systematic deviations for a specific sponge type.

In order to check whether the empirical correlation for ceramic sponges can be also used to predict mass transfer coefficients of metallic sponges, the mass transfer properties of the stainless steel sponge M-40PPI_0.95 were also analyzed. The geometrical surface based on the tetrakaidecahedron model was used to calculate the experimental k_m-values of the metal sponge from the volumetric mass transfer coefficients k_v, since MRI-characterization of the ferro-magnetic material is not possible (Figure 3.11-B, chapter 3).

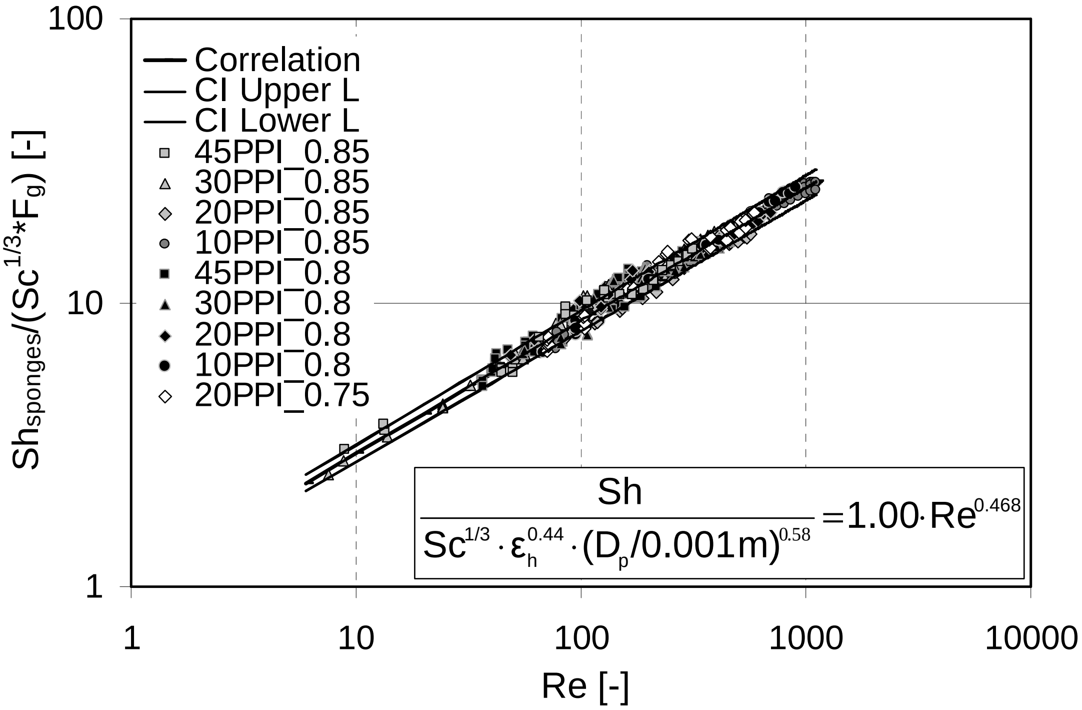

Figure 4.12: Empirical correlation for the prediction of mass transfer coefficients in ceramic sponges.

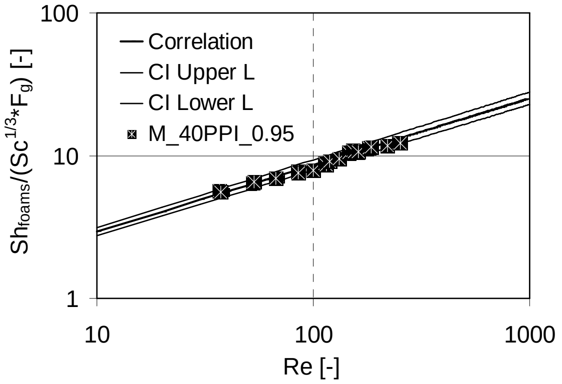

Figure 4.13: Comparison between experimental Sh-values of metal sponge M_40PPI_0.95 and the empirical correlation.

The experimental *Sh*-data of the metal sponge were taken and plotted for comparison together with the established correlation (no data fitting) in Figure 4.13. The agreement between the slopes is within 6 %. As can be seen, there is no systematic error and the experimental points fall pretty well within the confidence interval of 95 %. It can hence be concluded, that the correlation (eq. (4.38)) established for ceramic sponges can be used as well for metallic sponges for a first estimation of mass transport in spite of somewhat higher void fractions.

4.4.1.8 General dimensionless description taking pore anisotropy into account

Even though the empirical correlation is most useful for predicting mass transfer properties of sponges in a wide hydrodynamic range, a lack of knowledge regarding the geometry of these irregular structures made a physically well based solution by dimensional analysis most difficult. Pore and cell anisotropy and variation of cell orientation of different sponge geometries were optically recognized. An additional and extremely laborious (and representative) characterization of pore diameters in the *x*-*z* and *y*-*z* plane is needed for every sponge type in order to quantify the anisotropy and preferential orientation of the pores in space (chapter 3). With this, influencing dimensionless geometric ratio(s) for this phenomenon have been found and included, suitable to describe these geometrically not perfectly similar cellular materials in a more general way.

As explained in chapter 3, the most convenient way of quantifying the pore anisotropy of the sponges used herein is with the ratio between the longest pore length divided by the two shorter ones, $a^2/(b \cdot c)$, since this feature is independent on the spatial orientation of the cells or pores. Following the fitting approach described in subchapter 4.4.1.6, a new geometric function $F_{g,A}$ was defined including the pore anisotropy ratio and the porosity:

$$F_{g,A} = \left(\frac{a^2}{b \cdot c} \right)^{\mathrm{p}} \cdot (\varepsilon_h)^{\mathrm{q}} . \tag{4.39}$$

The resulting, physically well-based general description of the mass transfer properties of ceramic sponges including fit parameters giving the lowest variance (0.78) is given below:

$$Sh = 0.81 \cdot Re^{0.47} \cdot Sc^{1/3} \cdot \left(\frac{a^2}{b \cdot c} \right)^{0.84} \cdot \varepsilon_h^{0.43} \tag{4.40}$$

Figure 4.14 displays the general correlation proposed in eq. (4.40) together with the mass transfer data of the ceramic sponges and the confidence intervals of the correlation.

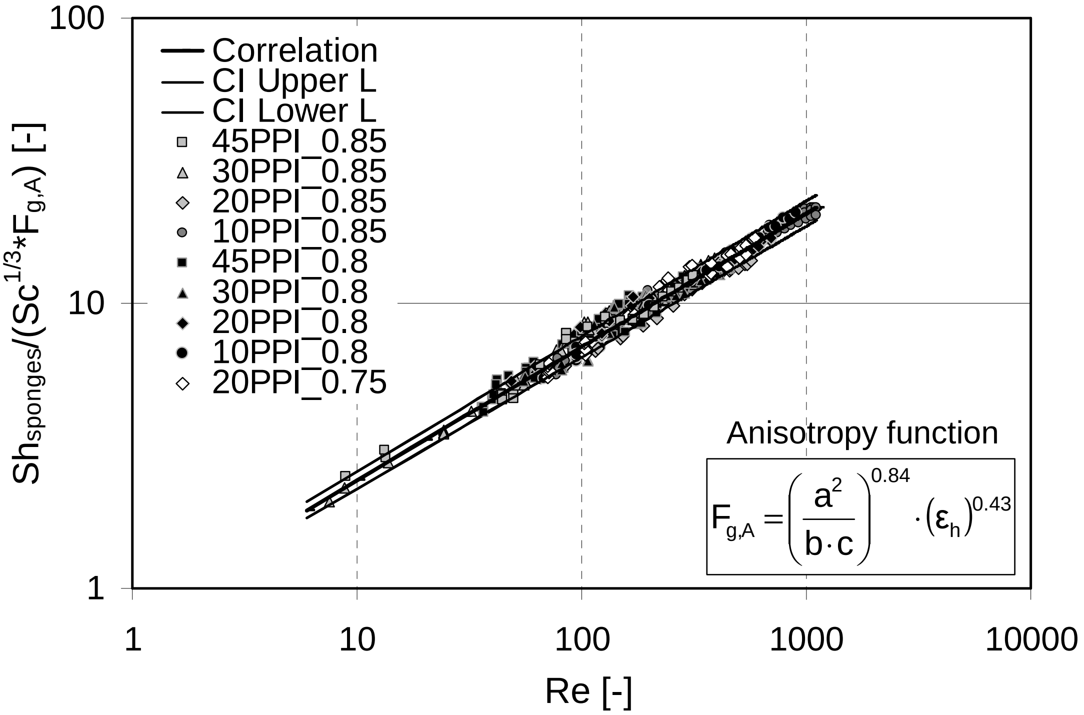

Figure 4.14: General correlation between the mass transfer, hydrodynamics and geometric properties of ceramic sponges from this work, yielded from dimensional analysis of these structures.

The correlation of the fitted parameters to each other and the confidence intervals are in the same range as in the empirical correlation (Appendix G).

Even though this general relation including anisotropy effects is physically better based than the empirical correlation, it must be pointed out that the amount of analyzed pores in the radial plane (D_p) was much higher and, thus, more representative than the amount of axial pore lengths necessary for the calculation of the anisotropy ratio. A more detailed discussion of this issue was presented in chapter 3. Moreover, the empirical correlation, eq. (4.38), is as accurate as the general relation, (eq. (4.40)), but requires less input information from the geometric structure (merely D_p) and much less sponge pieces need to be destroyed for the analysis.

4.4.2 Pressure drop

4.4.2.1 Pressure drop through ceramic sponges

The pressure drop measurements were reproducible on the same sponge sample within 1 %. The influence of the 3 – 8 wt. % SnO_2-washcoat on the pressure drop of a sponge sample was evaluated and found to be negligible (< 4 %). Due to variations between different samples of the same type, 3 – 5 different sponge samples had to be measured of every sponge type. Figure 4.15 shows the data of 30PPI_0.8 (four different samples). Since the deviations upon all measured sponges were up to ± 15 %, the bulk density of every analyzed sponge piece was evaluated in order to find out if the deviations were connected to variations in the bulk density of the pieces. As clearly displayed in the figure, the deviations can not be correlated to variations in density. The reason for the discrepancy is most probably the irregular structure of the pores. For instance, some pores in the sponge pieces are closed, leading to a higher drag coefficient c_D. The extent of irregularities or number of closed pores is not the same in different samples and has a much stronger effect on the pressure drop than it has on the mass transfer properties. Other authors have reported similar observations in the context of their pressure drop data [13]. For this reason, the pressure drop behaviour is a good tool to check for the presence of closed pores inside a sponge.

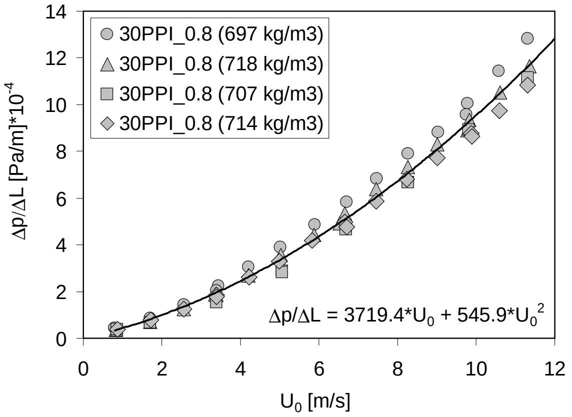

Figure 4.15: Pressure drop versus superficial velocity of the 30PPI_0.8 sponge (220 °C).

As stated at the beginning of this chapter, the pressure drop of a fluid upon flow through porous structures can be described with the Forchheimer equation:

$$\frac{\Delta p}{L_{bed}} = f_1 \cdot U_0 + f_2 \cdot U_0^2 \quad \text{or} \quad \frac{\Delta p}{L_{bed}} = \frac{\eta}{k_1} \cdot U_0 + \frac{\rho}{k_2} \cdot U_0^2 \tag{4.9}$$

f_1 and f_2 are the (fluid property dependent) pressure drop constants of one sponge type at constant hydrodynamic conditions. k_1 and k_2 are the permeability constants of the structure, which are dependent only on its geometry. The mean values for the constants from all samples measured were taken for the description of the average pressure drop of a given sponge geometry. The values f_1 and f_2 of the 30-PPI_0.8 sponge are given in Figure 4.15 (bottom).

Typical pressure drop values of the sponges with 80 % porosity are shown in Figure 4.16. As expected, the pressure drop increases as the pore size decreases since the geometric surface increases with the pore count. Nevertheless, it is important to note that the 30- and 45-PPI sponges used in this work have similar pressure drop slopes. In singular cases, the pressure drop over a 30-PPI sample was even higher than over a 45-PPI sponge.

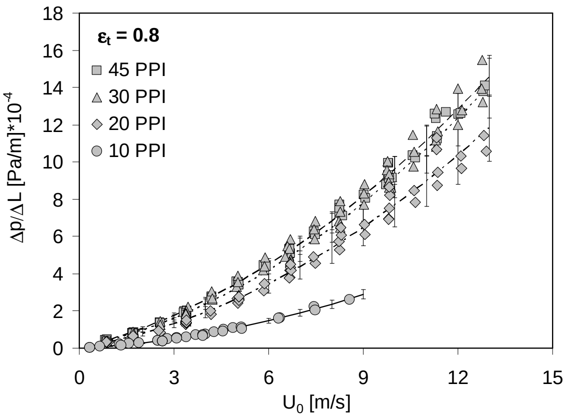

Figure 4.16: Pressure drop data of 10 – 45 PPI sponges with 80% porosity.

The influence of the porosity on the pressure drop of the 20-PPI sponges is exemplarily displayed in Figure 4.17. The pressure drop evidently increases with decreasing void fraction. The deviation between different samples also increases strongly at lower porosities, as can be observed in the figure. This fact supports the argument that the deviations arise from imperfections caused during the manufacturing process, for instance, when the ceramic slurry is removed.

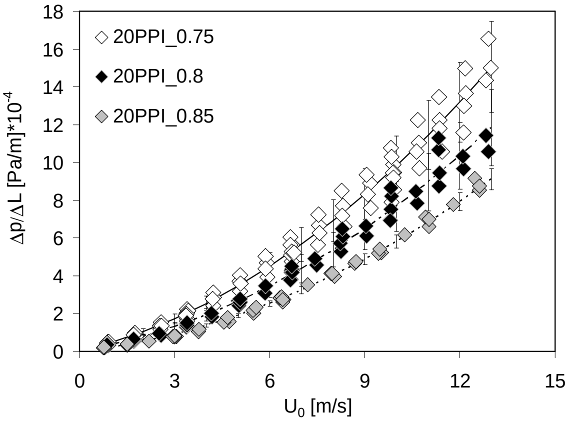

Figure 4.17: Influence of porosity on pressure drop of the 20-PPI sponges.

The viscous and inertial constants f_1 and f_2 obtained from the sponges and their confidence limits are listed in Table 4.6. Since these constants are dependent on the fluid properties, the representative constants for a sponge geometry, independently of η and ρ, are represented by the viscous and inertial permeability parameters k_1 and k_2; these are also listed in the table.

Table 4.6: Viscous and inertial constants and permeabilities of the analyzed sponges.

Sponge type	f_1 [Pa·s/m^2]	f_2 [Pa·s^2/m^3]	$k_1 \cdot 10^9$ [m^2]	$k_2 \cdot 10^3$ [m]
10PPI_0.8	941 ± 66	252 ± 11	28.59	3.13
20PPI_0.8	2933 ± 313	474 ± 32	9.17	1.67
30PPI_0.8	3719 ± 204	546 ± 21	7.23	1.45
45PPI_0.8	4315 ± 211	529 ± 21	6.23	1.49
10PPI_0.85	681 ± 65	133 ± 11	39.5	5.94
20PPI_0.85	1835 ± 124	398 ± 11	14.66	1.98
30PPI_0.85	2430 ± 298	419 ± 31	11.07	1.89
45PPI_0.85	2704 ± 240	432 ± 25	9.95	1.83
20PPI_0.75	3993 ± 398	583 ± 40	6.74	1.36
M_40PPI	*2108 ±105*	*215 ±6*	*12.76*	*3.67*

4.4.2.2 Comparison with results and correlations from the literature

To compare with literature results, only data from sponges with features similar to those of our samples were taken into account. Schlegel et al. [23] measured the pressure drop of sponges with 85 % porosity. Although the sizes of their samples were significantly different (Table 4.3), the authors observed similar pressure drop values in the case of 20- and 30-PPI sponges (Figure 4.18). Moreira et al. [14] measured the resistance to flow of three SiC-Al_2O_3 sponges in water and air. The features of the sponges from the literature not yet displayed in Table 4.3 are listed in Table 4.7. Whereas the pressure drop slopes of their 8- and 20-PPI sponges are qualitatively in agreement with the data from this work, the pressure drop of the 45-PPI is significantly higher, as displayed in Figure 4.18. The reason is the differing porosity of the sponges used by Moreira et al. While the 8-PPI sponge has a porosity of 94 %, the void fraction of the 45-PPI is merely 76 %. This decrease in porosity can be explained by the increasing difficulty for ceramic slip removal during manufacturing, which leads not only to a higher density, but also to a higher amount of closed pores. The pressure drop of 10-, 30- and 45-PPI Al_2O_3-sponges measured by Richardson et al. [13] is also plotted in Figure 4.18. The authors found considerably higher values for the pressure drop of the 30- and 45-PPI sponges as compared to this work. Since the material was Al_2O_3 and the dimensions were similar, the deviations arise most probably from a different origin and quality of the structures. The amount of closed pores in a sponge sample can differ significantly, leading to considerable variations between pressure drop values of different authors. Another possible reason is the systematic difference in pore diameter for sponges having apparently the same pore count. The pore diameters reported by these last authors are smaller than those determined in this work, as can be observed upon comparison of Table 3.2 and Table 4.7.

Table 4.7: Features of the sponges analyzed in the literature on pressure drop.

[PPI]	D_p [mm]	ε_t [-]	S_{geo} [m^{-1}]
Richardson et al. [13]			
10	1.68	0.88	2064
30	0.826	0.88	4032
45	0.619	0.80	5100
Moreira et al. [14]			
8	2.3	0.94	1098
20	0.8	0.88	2304
45	0.36	0.76	5616

Most of the literature describes the pressure drop of sponges with the Ergun equation [13-15] although this equation was derived for granular beds (eq. (4.7)). Richardson et al. [13] used the model of parallel cylinders for calculating the geometric surface area, introducing an additional influence on porosity, but leaving the original dependence on porosity in the Ergun equation. Since their data was still not well represented by the equation (because the model is not correct), the authors determine new constants of the Ergun equation by an empirical fit. Thereby, they introduce yet another dependence on the porosity and the pore diameter. Moreira et al. [14] applied the general Forchheimer equation with the dependence on porosity of the Ergun equation. The dependence of pressure drop on pore diameter was empirically fitted to their data.

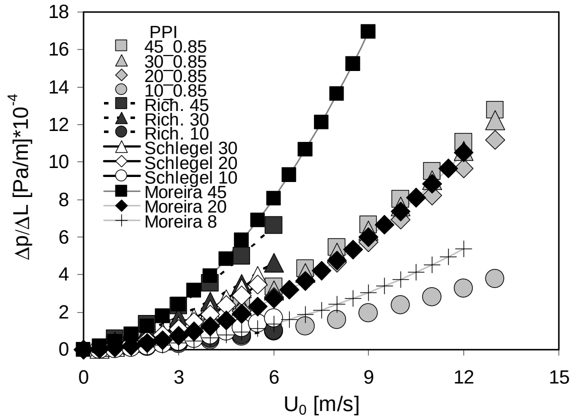

Figure 4.18: Comparison between pressure drop data of this work with literature data. Different shadings represent different references; circles: 10PPI, diamonds: 20PPI, triangles: 30 PPI and squares: 45 PPI.

Lacroix et al. [15] applied the unchanged Ergun equation (4.8) and substituted the strut diameter derived from the cubic cell (CC) model for the particle diameter. This substitution is based on the comparison of sponges and particles with the same specific surface area per unit volume and the same porosity

$$S_{geo,CC} = \frac{4}{d_t} \cdot (1-\varepsilon) = S_{geo,beads} = \frac{6}{D_{particle}} \cdot (1-\varepsilon) \tag{4.41}$$

leading to

$$D_{particle} = 1.5 \cdot d_t\,, \tag{4.42}$$

with

$S_{geo,CC}$: geometric surface area of a cubic cell with cylindrical struts

and

$S_{geo,beads}$: geometric surface area of a packed bed of spheres.

Hence, the modified Ergun equation proposed by Lacroix et al. represents a combination of two different geometric models, the hydraulic diameter model, from which the dependence of the Ergun equation on the porosity and particle diameter arises, and the cubic cell model. The authors conclude honestly in their publication: "Although no physical reason can be invoked in principle to explain the extension of the Ergun equation, the model is in good agreement with experimental data…."

The correlations from the literature were evaluated with own experimental pressure drop data. The predictions by all literature correlations were not satisfying.

With the experimental values for permeability (k_1, k_2) and geometric (ε_h, D_p) parameters of the sponges, an empirical relation was found to describe the permeability constants (eqs. (4.43) and (4.44)).

$$k_1 = 1.42 \cdot 10^{-4} m^2 \cdot \left(\frac{D_p}{m} \right)^{1.18} \cdot \varepsilon_h^{7.00} \tag{4.43}$$

$$k_2 = 0.89 m \cdot \left(\frac{D_p}{m} \right)^{0.77} \cdot \varepsilon_h^{4.42} \tag{4.44}$$

The empirically fitted permeability parameters were compared to the model of Lacroix et al., since it displayed the closest representation of the pressure drop data in this work among all literature correlations. Figure 4.19 shows that the data obtained from 20 PPI sponges with two different porosities, as an example, are not well represented by the modified Lacroix-Ergun equation. The experimental strut diameters from this work in the relation proposed by Lacroix resulted in a stronger overprediction of the pressure drop than displayed in the figure. Therefore, the strut diameter d_t was calculated from the model for the cubic cell (eq. (3.15); chapter 3) as a function of the experimental pore diameter D_p. The reason for the better representation of the experimental pressure drop as well as the specific surface area data (cf. chapter 3.3.2) upon using eq. (3.15) for calculating the strut diameter is closely related to the fact that, due to the manufacturing process, the strut diameter does not increase proportionally to the nod size as porosity decreases. The ceramic precursor is deposited preferentially at the intersections rather than along the struts. This was also observed by Lacroix et al. Hence, taking merely the experimental strut diameter does not account for the solid deposited in the intersections. This approach predicts a far too high geometric surface and, consequently, a higher pressure drop of the structure. The same conclusion can be drawn from the dependence of pressure drop on pore diameter, which is as well strongly overrated by the Lacroix-Ergun equation when applied to the ceramic sponges used in this research project.

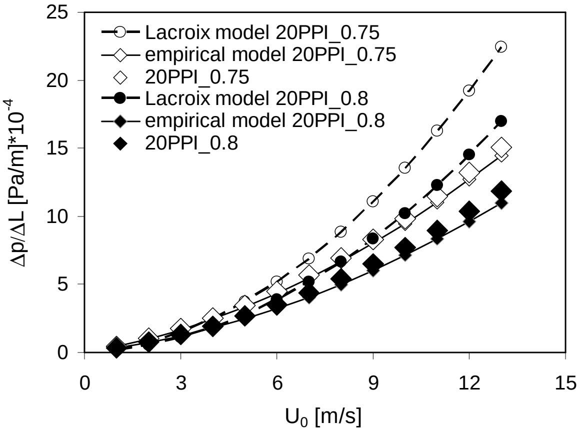

Figure 4.19: Comparison of the Ergun-based equation by Lacroix et al. [15] with experimental pressure drop data and the empirical relation from this work.

Since none of the correlations published is able to predict pressure drop values in a general way, there is no reason to favour any of these semi-empirical Ergun-based models over the Forchheimer equation for flow through porous structures. The parameters given in equations (4.43) and (4.44) give a good representation of the influence of porosity and pore diameter on pressure drop.

Due to the inevitable irregularities of the sponge samples, extensively discussed along this chapter, the difference between the values of experimental permeability parameters $k_{i,exp}$ and the relations given above can be up to 25 %. Hence, these equations should be used only for a first estimation of the pressure drop in sponges. Nevertheless, 3-5 different pieces of the same sponge type were assessed, yielding quite representative average values of the pressure drop for each sponge type. In contrast, existing literature correlations are based on a rather small selection of specific sponge samples.

The most important conclusion from the evaluation and comparison of pressure drop data of sponges from different authors is that no general relation for the prediction of permeability in sponges can be yet achieved. The resulting morphology and quality of sponges from different manufacturers vary considerably despite of using the same (replication) method. Manufacture process optimization is needed for the reproducible production of sponges with a constant pore density and similar permeabilities. More attention should be given to the amount of closed pores which substantially affect pressure drop. A volume imaging method like MRI could quantify closed pores in a sample. If the real structure of this sample could be reconstructed in a CFD grid, pressure drop could be simulated with local resolution.

4.4.3 Verification of the Lévêque analogy between mass (and heat) transfer and pressure drop

It has been of great scientific interest to develop well substantiated relations for the prediction of mass transfer from the similar processes of fluid friction and heat transfer, where there is no available data. An analogy between pressure drop and heat (or mass) transfer in various heat exchanger types found by Martin [20] based on the generalized Lévêque equation (4.21) was presented in subchapter 4.2.3. One of the goals of this research project was to verify, if this analogy would be applicable to irregular cellular structures like sponges.

The pressure drop can be expressed in the dimensionless form by the Hagen-number [19]:

$$Hg = 2 \cdot f \cdot Re^2 = \frac{\Delta p}{\Delta L} \cdot \frac{D_p^3}{\rho \cdot \nu^2} \quad \neq \mathrm{f}(Re) \tag{4.45}$$

Figure 4.20, left, shows the experimental values of *Sh* vs. *Hg* obtained from the ceramic sponges. The mass transfer coefficients of sponges are proportional to the cubic root of the pressure gradient. It can, therefore, be concluded that the generalized Lévêque-equation represents qualitatively the hydrodynamic mass transfer behaviour of sponges. In order to control if, by directly applying the analogy to the sponges, a good correlation would be obtained, the *Sh*-values were also plotted over the cubic root of the Lévêque-number (*Lq*), defined as:

$$Lq = 2 \cdot x_f \cdot Hg \cdot Pr \cdot D_h/L \quad \text{(cf. eq. (4.21))} \tag{4.46}$$

In the case of sponges, the semi-empirical length *L* has not been yet defined in the literature. This length is supposed to represent the average distance between two eddy delaminations, or the length of a flow path, since the applicability of the Lévêque-analogy arises from the periodical interruption of thermal (or diffusive) boundary layers upon flow through a given structure. For packed beds of spheres and other periodic geometries, relations for *L* as a function of porosity and characteristic length are proposed [19,20]. For sponges, the following relations leading to a physically founded approach of this length are given. If the flow path is commonly interrupted after a strut or vortex, then the ratio between the average length of a flow path and the inner pore diameter could be approximated by:

$$\frac{L}{d_p} \cong \left(\frac{V_{tot}}{V_{void}}\right)^{1/3} = \left(\frac{1}{\varepsilon}\right)^{1/3}, \tag{4.47}$$

V_{tot} and V_{void} being the total- and void volumes of one hypothetical representative unit cell, respectively. Combining eq. (4.47) and the definition of the hydraulic diameter (eq. (4.7)) yields:

$$\frac{D_h}{L} = \frac{4 \cdot \varepsilon}{S_{geo}} \cdot \frac{\varepsilon^{1/3}}{d_p}. \tag{4.48}$$

Combination of equations (4.46) and (4.48) leads to experimental values for the *Lq*-numbers of the sponges. As can be observed in the right plot of Figure 4.20, the direct application of the analogy as proposed in the literature is not able to uniquely predict mass transfer coefficients from the pressure drop across sponge geometries. In fact, there is no better correlation of the mass transfer coefficients to the pressure drop when using the Lévêque-analogy than in the case of the raw *Sh*- and *Hg*-values.

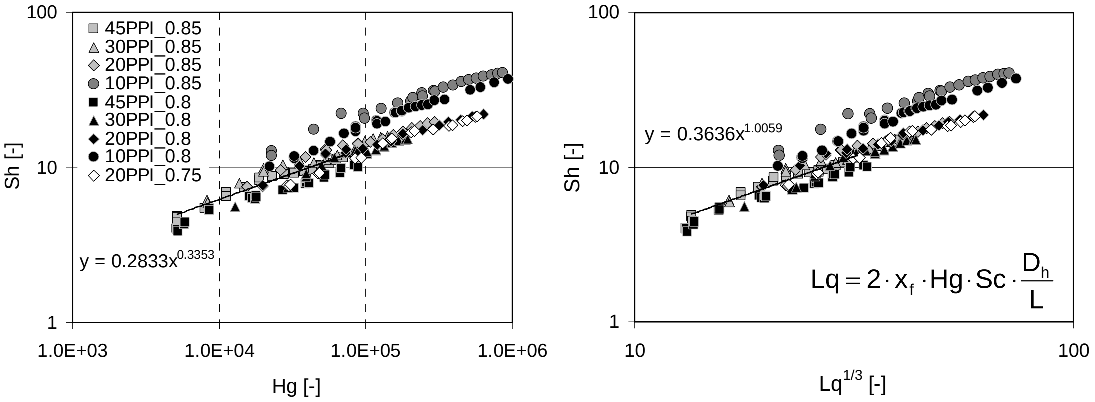

Figure 4.20: Mass transfer (Sh) versus pressure drop (Hg or Lq) properties of ceramic sponges. Left: raw data; right: verification of the unmodified Lévêque-analogy.

The trend in the *Sh*-values of different sponges at constant *Hg* (or *Lq*) is qualitatively the same as at constant *Re*, namely increasing with the pore size, pointing out the similarity in the physical phenomena of mass and momentum transfer and their direct dependence on the hydrodynamic conditions of flow. Here again, irregularities and changes in anisotropy require an additional evaluation of the geometry as was needed previously in the correlation of mass transfer to hydrodynamics (*Sh* to *Re*). Following the same procedure as in the parameter fitting of the empirical and general *Sh*-*Re* correlations described before, geometric functions were defined as in the case of eq. (4.35), for the expansion of the modified Lévêque equation:

$$Sh = A^* \cdot Hg^{B^*} \cdot Sc^{1/3} \cdot F_g \tag{4.49}$$

The term D_h/L in the generalized Lévêque equation was left out in the following analysis since it remains nearly constant among the analyzed sponges. This is the reason for the nearly equal slopes displayed in both diagrams of Figure 4.20. Moreover, it makes no sense to leave this term in the equation, since its influence can not be evaluated and has not been yet analyzed for sponges. Due to the observed similarity between the dependence of the *Sh*- to the *Re*- and *Hg*-values of sponges, it seems reasonable to use the same geometric functions, i.e. the empirical function F_g (eq. (4.36)) and the anisotropic function $F_{g,A}$ (eq. (4.39)), to correlate the mass transfer to the pressure drop of these structures.

As expected, this is a suitable means to derive an acceptable correlation of mass transfer to pressure drop data of the ceramic sponges. The accuracy was ±20 % (confidence interval 95 %). Furthermore, the empirical and the general correlation of *Sh* to *Hg*-values are equivalent with respect to accuracy as indicated in Figure 4.21. Again, it should be noticed that the empirical correlation based on the mean pore diameter D_p and outer porosity as geometric input information is of more practical use than the general relation, which requires analyses in 3D.

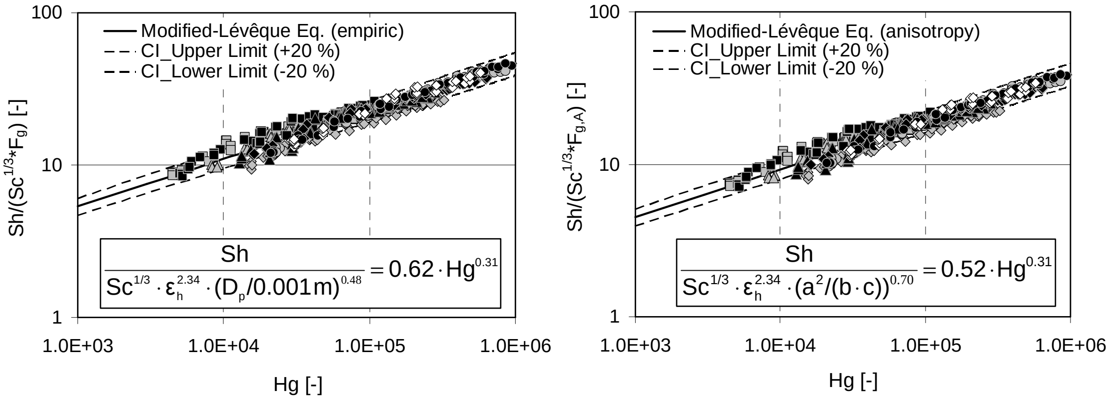

Figure 4.21: Correlations for the prediction of mass transfer coefficients from pressure drop data of ceramic sponges. Left: empirical correlation. Right: general correlation taking anisotropy into account. Same data as displayed in Figure 4.20.

The accuracy of the *Sh-Hg* relations is considerably lower than the *Sh-Re* correlations (merely ± 9 %). Since there were considerable deviations in pressure drop of a given sponge type due to quality differences among different samples, it can be understood that the prediction of mass transfer from pressure drop data will not be very satisfying. Even though the applicability of the (modified) Lévêque-analogy to sponges was confirmed, it should be taken only as a first estimate. For a more reliable prediction of mass transfer coefficients from hydrodynamic conditions, equations (4.38) and (4.40) should be used.

4.4.4 Overall performance of sponges, honeycombs and beads

As discussed previously, the mass transfer performance of sponges is between bead packings and honeycombs, the former displaying the best and the latter the worst mass transfer coefficients at comparable geometric surface areas. The pressure drop data of the different carriers with comparable geometric surface areas per bed volume is exemplarily displayed in Figure 4.22, together with well established relations for the estimation of the pressure drop of beads and honeycombs, the Ergun equation (4.8) [12] and the Poiseuille equation (4.50) [4,25], respectively. The agreement between the data from this work and the literature relations is satisfactory, confirming the suitability of the experimental method used.

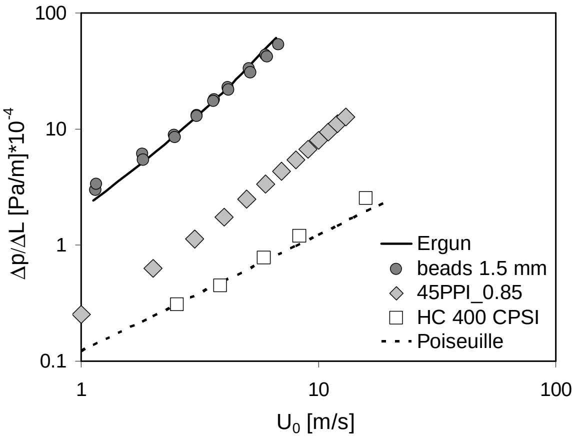

Figure 4.22: Pressure drop over superficial velocity of a packing of spheres, a sponge and a honeycomb with comparable geometric surface areas per bed volume (1800 – 2500 m^2/m^3).

$$\frac{\Delta p}{L_{bed}} = \frac{32 \cdot \eta}{D_h^2 \cdot \varepsilon} \cdot U_0 \tag{4.50}$$

As in the case of mass transfer, the pressure drop of sponges is between that of beads and honeycombs. The honeycomb has by far the lowest pressure drop of all structures due to the uninterrupted laminar flow through the straight channels in this carrier. The beads have, as expected, the highest pressure drop because the porosities of packed beads are low (between 39 and 44 %), and the flow path is tortuous.

4.4.4.1 Assessment of the carrier performances as a catalytic packing

In catalytic packings for environmental applications, high conversions under mass transfer limitation are mandatory to obtain the necessary emission abatement while keeping the pressure drop as low as possible. Since the permeability and mass transfer capability of the analyzed structures are of opposite tendency, it is not easy to decide which of these carriers is more advantageous from the viewpoint of maximum mass transfer at a minimal pressure drop. Here, a combined performance parameter based on a “dimensionless trade-off index *I*” defined by Giani et al. [5] is used for this purpose:

$$I = \frac{k_m \cdot S_{geo} \big/ U_0}{\dfrac{\Delta p}{\Delta L} \Big/ \rho \cdot U_0^2} = \frac{Sh \cdot Re \cdot L_{char} \cdot S_{geo}}{Hg \cdot Sc} \tag{4.51}$$

This index reflects the overall performance of a support, independently of characteristic length or the bed length used. It actually expresses how much conversion (mass transfer limited reaction) can be achieved in a packed bed volume related to the energy loss caused by drag and friction forces during flow through the structure. Evidently, high values of the index imply a good performance of a support. The calculated values of the trade-off index on the basis of the experimental data for all carriers used in this work are shown in Figure 4.23. The honeycomb is apparently the structure with optimum performance of conversion per energy loss, followed by the sponges and the packed beads, the latter displaying the worst performance due to their high pressure drop. The sponges perform substantially better than the packed beds of spheres in the complete hydrodynamic range under investigation.

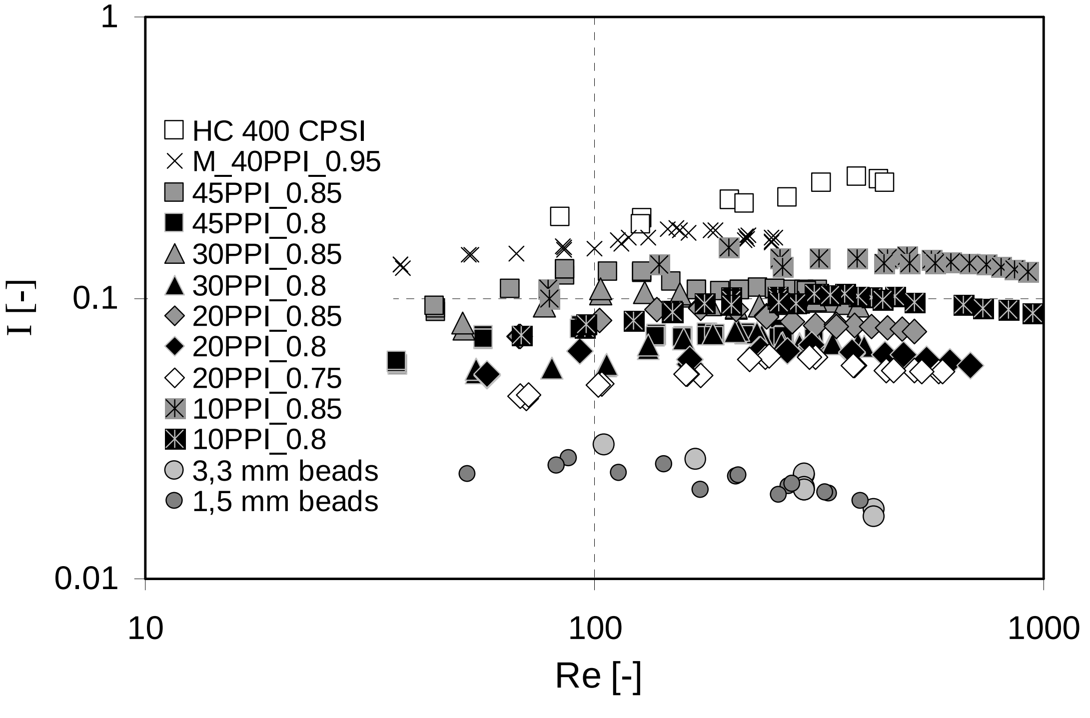

Figure 4.23: Comparison of structure performance with the proposed trade-off index I (eq. (4.51)) over the analyzed hydrodynamic range (Re) for sphere packings, sponges and honeycombs.

A considerable influence of the porosity can be recognized from the slopes of the plot. Since, in contrast to the pressure drop, the mass transfer of sponges does not depend strongly on the porosity, the trade-off index of the sponges increases noticeably with increasing porosity. For this reason, the metallic sponge with an extremely high void fraction of 95 % has the best performance of all sponges. Even though the 10-PPI pore density seems to be the optimum geometry from the perspective of catalytic efficiency, no systematic tendency can be recognized from the remaining sponge geometries. Hence, no precise conclusion regarding the optimum pore density can be derived. The choice of the specific geometry will depend on the paramount phenomenon, mass transfer or pressure drop, in the process of application. Moreover, important aspects to be considered are the operating temperature and the heat transfer within the bed. Many environmental applications involve high temperatures, making the use of metallic supports impossible due to the considerably higher thermal expansion of metals as compared to ceramics. Furthermore, the mechanical strength of metals decreases much stronger with temperature in comparison to that of a ceramic material. In such cases, ceramic sponges should be preferred, although the trade-off between mass transfer and pressure drop performance is not as good as that of highly porous metallic sponges. The heat transport (convective and conductive) within the packing is another aspect of importance. Most reactions that are performed at short contact times, where the magnitude of mass transfer is most important for the overall kinetics, are also highly exothermic. The temperature distribution along and across the catalytic bed can play a decisive role in the control of product selectivity and catalyst lifetime as for instance in partial oxidations. Due to their higher tortuousity and the hereto related enhancement of radial mixing and turbulence in the flowing fluid, beads and sponges clearly outrun the honeycomb. The total lack of radial mixing upon flow through the channels of a honeycomb leads to high temperature increases of up to 25 K within a length of 20 mm along the packed support (in this work). At comparable conversions (heat production) the highest measured temperature increase was 10 K and 17 K in the case of sponges and beads, respectively. A detailed evaluation of the influence of heat transport was neither within the scope of this research nor within the experimental possibilities of the apparatus designed for the measurement of mass transfer phenomena. Nevertheless, the transport of heat to or from sponge geometries packed in a reactor has been recently studied and is still subject of interest, since it constitutes an extremely important characteristic that is decisive for the industrial implementation of these morphologically peculiar structures. Most of these studies confirm enhanced heat transport and smoother temperature distributions in sponge packings as compared to honeycombs or beds of granules [26 - 29].

Finally, it can be concluded that sponges seem to offer the best trade-off between high mass transfer, permeability and heat transport among the analyzed supports.

References

[1] J. T. Richardson, D. Remue, J. K. Hung, *Properties of ceramic foam catalyst supports: mass and heat transfer,* Appl. Catal. A: General 250 (2003) 319-329.

[2] G. Groppi, L. Giani, E. Tronconi, *Generalized correlation for gas/solid mass-transfer coefficients in metallic and ceramic foams*, Ind. Eng. Chem. Res. 46 (2007) 3955 – 3958.

[3] P.N. Dwivedi, S.N. Upadhyay, *Particle-fluid mass transfer in fixed and fluidized beds*, Ind. Eng. Chem., Process Des. Dev. 16 (1977) 157-165.

[4] A. Cybulski, J.A. Moulijn, *Monoliths in heterogeneous catalysis*, Catal. Rev.-Sci. Eng. 36 (1994) 179 – 270.

[5] L. Giani, G. Groppi, E. Tronconi, *Mass-transfer characterization of metallic foams as supports for structured catalysts*, Ind. Eng. Chem. Res. 44 (2005) 4993-5002.

[6] E. N. Fuller, P. D. Schettler, J. C. Giddings, *A new method for prediction of binary gas-phase diffusion coefficients*, Ind. Eng. Chem. 58 (1966) 19 – 27.

[7] T. K. Sherwood, R. L. Pigford, C. R. Wilke, *Mass transfer*, McGraw-Hill, Düsseldorf, 1975.

[8] W. Nernst, *Theorie der Reaktionsgeschwindigkeit in heterogenen Systemen*, Z. f. physik. Ch. 47 (1904) 52 – 55.

[9] R.B. Bird, W.E. Stewart, E.N. Lightfoot, *Transport phenomena*, Wiley, Weinheim, 2002.

[10] VDI-Wärmeatlas, *Berechnungsblätter für den Wärmeübergang*, VDI-Verlag, Düsseldorf, 1991.

[11] E. Tsotsas, *Über die Wärme- und Stoffübertragung in durchströmten Festbetten. Experimente, Modelle, Theorien*, Fortschrittberichte VDI Nr. 223, VDI-Verlag, Düsseldorf, 1990.

[12] S. Ergun, *Fluid flow through packed columns*, Chem. Eng. Prog. 48 (1952) 89 – 94.

[13] J. T. Richardson, Y. Peng, D. Remue, *Properties of ceramic foam catalyst supports: pressure drop,* Appl. Catal. A: General, 204 (2000) 19 – 32.

[14] E. A. Moreira, M. D. M. Innocentini, J. R. Coury, *Permeability of ceramic foams to compressible and incompressible flow,* J. Eur. Ceram. Soc. 24 (2004) 3209 – 3218.

[15] M. Lacroix, P. Nguyen, D. Schweich, C. P. Huu, S. Savin-Poncet, D. Edouard, *Pressure drop measurements and modelling on SiC foams*, Chem. Eng. Sci. 62 (2007) 3259 – 3267.

[16] L. I. Sedov, *Similarity and dimensional methods in mechanics*, Adademic Press, New York, 1959.

[17] W.J. Duncan, *Physical similarity and dimensional analysis: An elementary Treatise*, Edward Arnold & Co., London, 1953.

[18] T. H. Chilton, A. P. Colburn, *Mass Transfer (Absorption) Coefficients: Prediction from Data on Heat Transfer and Fluid Friction*, Ind. Eng. Chem. 26 (1934) 1183 – 1187.

[19] H. Martin, *The generalized Lévêque equation and its practical use for the prediction of heat and mass transfer rates from pressure drop*, Chem. Eng. Sci. 57 (2002) 3217 – 3223.

[20] H. Martin, *The lévêque-analogy or how to predict heat and mass transfer from fluid friction*, 4th. International conference on heat transfer, fluid mechanics and thermodynamics HEFAT 2005 Cairo, Egypt.

[21] G. Eigenberger, V. Kottke, T. Daszkowski, G. Gaiser, H.-J. Kern, *Regelmäßige Katalysatorformkörper für technische Synthesen*; Fortschrittberichte VDI, Reihe 15: Umwelttechnik, Nr. 112, VDI-Verlag Düsseldorf, 1993.

[22] G. Reisener, M. Schreier, R. Adler, *Korrektur reaktionskinetischer Daten des realen Differential-Kreislaufreaktors*, Chemie Ingenieur Technik, 72 (2000) 1192 – 1195.

[23] A. Schlegel, P. Benz, S. Buser, *Wärmeübertragung und Druckabfall in keramischen Schaumstrukturen bei erzwungener Strömung*, Wärme- und Stoffübertragung 28 (1993) 259 – 266.

[24] T. F. Coleman, Y. Li, *An interior trust region approach for non linear minimization subject to bounds*, SIAM J. Opt. 6 (1996) 418 – 445.

[25] G. Desmet, J. De Greef, H. Verelst, G. V. Baron, *Performance limits of isothermal packed bed and perforated monolithic bed reactors operated under laminar flow conditions. I. General optimization analysis*, Chem. Eng. Sci. 58 (2003) 3187 – 3202.

[26] A. Reitzmann, F. C. Patcas, B. Kraushaar-Czarnetzki, *Keramische Schwämme-Anwendungspotential monolitischer Netzstrukturen als katalytische Packungen*, CIT 78 (2006) 885 – 898.

[27] A. Reitzmann, A. Bareiss, B. Kraushaar-Czarnetzki, *Simulation of a reactor for the partial oxidation of o-Xylene to Phthalic Anhydride packed with ceramic foam monoliths*, Oil Gas Europ. Mag. 2 (2006) 0179-3187/06/II.

[28] D. A. Hickman, L. D. Schmidt, *Synthesis gas formation by direct oxidation of methane over Pt monoliths*, J. Catal. 138 (1992) 267 – 282.

[29] T. Fend, B. Hoffschmidt, R. Pitz-Paal, O. Reutter, P. Rietbrock, *Porous materials as open volumetric solar receivers: Experimental determination of thermophysical and heat transfer properties*, Energy 29 (2004) 823 – 833.

5 Summary and general conclusions

The present research was devoted to the investigation of mass- and momentum transfer phenomena upon flow through ceramic sponges, and to the correlation of these properties to the hydrodynamic behaviour and the geometric features of the structures. To reach this goal, the CO oxidation over Pt/SnO_2-coated sponges was chosen as a diagnostic tool for the measurement of the overall kinetics in the temperature regime where mass transfer is the rate limiting mechanism. The precise temperature range, in which these conditions are met, depends on the catalyst type. In this work, the system Pt/SnO_2 has been chosen. This catalyst is active in the CO oxidation at low temperatures, already, due to a bifunctional mechanism between the noble metal and the metal oxide at the phase boundary line of both components. Hence, the first necessary step was the development of a suitable preparation method for the deposition of highly dispersed platinum nanoparticles with a narrow size distribution on SnO_2-coated sponges. It was shown that deposition of an organometallic Pt-complex from a supercritical solution in CO_2 with subsequent reduction of the organic ligands is a convenient method to reach this goal. On tortuous and irregular surfaces like ceramic sponges, the supercritical deposition results in substantially higher activities of the catalyst towards CO oxidation than the conventional deposition of Pt on SnO_2 by means of impregnation from aqueous solutions. A preliminary thermodynamic analysis of the supercritical mixture gave insight into the optimum conditions for deposition (p,T) in terms of solubility and phase behaviour. It is important that the solubility of the organometallic in carbon dioxide is high enough to reach considerable metal loadings after adsorption. Furthermore, the melting point of the precursor should not be reached at the high pressures applied to avoid the detrimental effect of surface tension on the Pt-dispersion. All analyzed structures, sponges, beads and a honeycomb, were first washcoated with a thin layer of SnO_2 and then furnished with Pt nanoparticles by means of supercritical deposition, leaving the geometric features of the supports unchanged.

A second prerequisite was the sound characterization of the morphology and porosity of the studied structures. Image analysis revealed the average inner pore- and strut diameters of the sponges as well as the pore and cell elongation (anisotropy), which increases with the pore size and has considerable influence on the transport properties of sponges. The mean pore diameter defined as the sum of inner pore and strut diameter was chosen as the characteristic length for dimensional analysis. Magnetic resonance imaging also revealed one of the most important features of a sponge, the geometric surface area (S_{geo}). The magnitude of this property can not be determined accurately from morphological models due to the irregular structure of the strut network of sponges. The surface areas measured are somewhat lower than those predicted from the tetrakaidecahedron model, which is still the best idealization of a sponge. In real sponges, accumulation of solid in the intersections of the strut network give rise to a lower geometric surface as compared to an ideal sponge with the same pore size and porosity having struts with constant diameter. From the manufacturing process, pores and voids are left in the solid struts, which have no relevance for the hydrodynamics of the sponges. Mercury intrusion porosimetry revealed both, the total and the hydrodynamically relevant (outer) porosities of all sponges. All sponges exhibited a strut voidage of about 22 %, resulting in considerable differences between total and outer porosities. Large deviations of up to 45 % in the bulk density along the axial direction of a cylindrical piece of sponge were observed in some of the samples, especially at higher pore densities, since the removal of the ceramic slip from the polymeric sponge during manufacturing is more difficult in the case of smaller pores. This finding emphasizes the necessity of an improvement of the manufacturing procedure for sponges, should they be implemented in industrial processes.

The mass transfer properties of catalytically coated sponges, beads and honeycomb were evaluated at 220 °C, at which temperature mass transfer was shown to control the rate of CO oxidation at the highest superficial velocity of 12 m/s. As expected, volumetric rate coefficients increase with increasing fluid velocity: $k_v \sim U_0^{(0.4\text{ -}0.5)}$. Due to the enlarged geometric surface area available in the same bulk volume at higher pore density, the volumetric rate coefficients of sponges increase in the order: 10- < 20- < 30- < 45-PPI. Although their geometric surface areas differ considerably, all sponges exhibit similar mass transfer coefficients ($k_m = k_v / S_{geo}$) over the whole velocity range. At constant pore density and interstitial velocity, mass transfer coefficients increase slightly with porosity in the analyzed porosity range of 75 – 85 %. The dimensionless mass transfer coefficients of sponges (Sherwood-numbers) increase with decreasing pore count at constant hydrodynamic conditions (Reynolds-numbers). These results are in agreement with heat transfer data of sponges from the literature, showing the same tendency in the case of dimensionless heat transfer data (Nusselt-numbers). A structure comparison showed that the mass transfer performance of sponges is between that of particle packings and honeycombs at comparable geometric surface areas, the former displaying the highest and the latter by far the lowest dimensionless mass transfer coefficients (*Sh*). In contrast to packed beds of particles, the mass transfer properties of sponges can not be completely described with the hydrodynamic and fluid properties of the system (Reynolds and Schmidt numbers) as the only influencing parameters. The reason is that sponges with different pore densities and porosities are not geometrically perfectly similar, i.e., every spatial dimension of the structure is not enlarged or contracted by the same factor. The additional influence of geometric parameters such as pore (and strut) diameter, geometrical surface, porosity and pore anisotropy on the mass transfer coefficients was evaluated by means of dimensional analysis. Two geometric functions, an empirical one including an additional influence of the pore diameter and porosity and one including the influence of pore anisotropy and porosity, were included in the dimensionless description (*Sh-Re-Sc*) of the mass transfer phenomena, yielding relations for the prediction of mass transfer coefficients of sponges with different pore sizes and void fractions in a wide range of Reynolds between 7 and 1100 with an accuracy of ± 9 %. The general correlation, which includes the influence of anisotropy, is physically well founded and represents the correct solution to a sound dimensional analysis. However, its application requires an extremely laborious characterization of pore diameters in all three spatial directions to quantify the anisotropy and the preferential orientation of pores in space. In the empirical correlation, the geometric function includes an empirical “dimensionless” mean pore diameter, which has no physical meaning, but it allows for a unification of the mass transfer data with the same accuracy as the general relation. The correlation including the empirical mean pore diameter requires a minimum of input parameters and is most advantageous for the user, who would otherwise need to do a complex geometric characterization of the analyzed structure before using the correlation to predict the mass- or heat transfer coefficients. A metallic sponge (40 PPI) with a porosity of 95 % was also analyzed for comparison. The experimental *Sh*-values are in excellent agreement with the values predicted by the empirical correlation for this sponge. Thus, the correlation also seems to be useful for the prediction of mass transfer coefficients of sponges with higher porosities and different materials. An important prerequisite for the use of the correlations is not only the quantitative characterization of the pore and strut dimensions, but also the knowledge of the hydrodynamically relevant void fraction of the structure, available from pycnometry methods with a non wetting fluid.

The pressure drop of sponges increases with increasing pore count and decreasing porosity. The samples exhibit closed pores to a certain, not quantifiable extent. This is a further, typical result of the non-optimized manufacturing process of sponges. More or less closed pores lead to considerable deviations in the pressure drop values of different samples from the same sponge type, especially at high superficial velocities. The pressure drop versus velocity data follows, as expected, the Forchheimer equation. Empirical relationships were found for the permeability parameters, showing a strong influence of the void fraction.

Based on the analogy between mass (or heat) transfer and pressure drop (Lévêque-analogy), the mass transfer data (*Sh*-values) could be correlated to the experimental pressure drop of the structures (Hagen-values) by using the same geometric functions as in the case of the *Sh*-*Re* relations, confirming the possibility to use this analogy for a first estimation (within ± 20 %) of mass transfer coefficients from pressure drop data.

The pressure drop of sponges, like their mass transfer capability, is between those of honeycomb monoliths and particle packings. A trade-off index was presented, which reflects the overall performance of a support regarding maximum mass transfer (conversion) with minimum pressure drop (energy loss). Sponges perform considerably better than packed beads over the whole hydrodynamic range (higher trade-off index). High porosity sponges are most favourable for an enhanced performance, but mechanical strength can be a limiting factor. The honeycomb displayed the best performance of all analyzed structures due to the extremely low pressure drop in the straight channels of this support. Nevertheless, sponges are clearly superior over honeycombs in terms of heat transport through the packing due to their tortuous structure, enabling transport through radiation at elevated temperatures and enhancing the radial convection. In contrast, the total lack of radial mixing in the channels of a honeycomb lead to considerable higher temperature increases at comparable packed lengths and conversions, this fact constituting a critical issue regarding its use in strongly exothermic or endothermic reactions, where inhomogeneous temperature distributions strongly affect product selectivity and catalyst lifetime.

The beneficial trade-off between enhanced mass transfer, moderate pressure drop and excellent heat transport offered by sponges render these irregular and tortuous cellular materials very attractive as an alternative to conventional catalytic supports in applications such as off-gas treatment, on-board hydrogen production and industrial chemical syntheses.

6 Zusammenfassung und Fazit

Feste Schwämme aus Keramik werden im Hüttenwesen als Gießfilter für Metallschmelzen eingesetzt. In jüngerer Zeit erforscht man aber auch neue Anwendungen in der Verfahrenstechnik. Insbesondere in der Reaktionstechnik könnten monolithische Packungen aus katalytisch beschichteten Keramik- oder Metallschwämme eine interessante Alternative zu herkömmlichen Festbetten sein. Vieles deutet darauf hin, dass Schwammpackungen bei geringem Druckverlust hervorragende Wärme- und Stofftransporteigenschaften aufweisen. Die bisherigen Studien erfolgten jedoch nicht systematisch, sondern punktuell an speziellen Schwammproben, so dass die Übertragbarkeit der Ergebnisse auf andere Schwamm-Materialien, Porendichten oder Porositäten -sofern diese Eigenschaften überhaupt charakterisiert wurden- zweifelhaft ist. Bei der quantitativen Einordnung der Transporteigenschaften von verschiedenen Schwammpackungen und beim Vergleich mit herkömmlichen Festbetten wie beispielsweise Partikelschüttungen oder Wabenkörpern stellt sich außerdem die Frage nach einer sinnvollen geometrischen Bezugsgröße. Allein schon die Festlegung einer charakteristischen Länge oder Fläche stellt im Fall von Schwämmen eine große Herausforderung dar, denn diese Strukturen sind nicht nur regellos, sondern -wie die vorliegende Arbeit zeigt- auch anisotrop.

Das Ziel der vorliegenden Arbeit war es, Stoff- und Impulsübertragung in durchströmten Schwämmen zu untersuchen und durch universelle, d.h. für alle Schwamm-Morphologien brauchbare Korrelationen zu beschreiben. Für die Bestimmung der Stofftransporteigenschaften wurde als Methode die Oxidation von Kohlenmonoxid an Pt/SnO_2-beschichteten Schwämmen angewandt. Bei geeigneter Reaktionsführung im stoffübergangskontrolliertem Bereich lassen sich Stoffübertragungskoeffizienten aus den Reaktionsgeschwindigkeiten ermitteln. Das katalytische System Pt/SnO_2 ist bereits bei moderaten Temperaturen in der CO Oxidation aktiv wegen eines Synergieeffektes zwischen dem Edelmetall und dem Metalloxid an der Phasengrenzlinie der beiden Komponenten. Aus diesem Grund musste in der ersten Phase des Projektes eine geeignete Herstellungsmethode für die Abscheidung hochdisperser Pt-Nanopartikeln mit enger Partikelgrößenverteilung auf SnO_2-beschichteten Schwämmen entwickelt werden. Es wurde gezeigt, dass dafür die Abscheidung eines organischen Pt-Komplexes aus einer überkritischen Lösung in CO_2 mit nachgeschalteter Reduktion eine sehr geeignete Methode darstellt. Die überkritische Abscheidung ermöglicht die Erzeugung von gleichmäßig verteilten Pt-Nanoteilchen auf tortuosen und unregelmäßigen Oberflächen wie keramischen Schwämmen, und diese Teilchen weisen aufgrund ihrer geringen Größe eine wesentlich höhere katalytische Aktivitäten in der CO Oxidation auf als die konventionell mittels Imprägnierung aus wässrigen Lösungen hergestellten Katalysatoren. Voruntersuchungen zum thermodynamischen Verhalten der überkritischen Lösung erlaubten die Auswahl von geeigneten Bedingungen (*p,T*) für die überkritische Abscheidung. Einerseits muss die Löslichkeit des organischen Metallkomplexes in Kohlendioxid hoch genug sein, um die gewünschte Metallbeladung nach Adsorption zu erreichen. Anderseits sollte der Schmelzpunkt des Vorläufers unter den herrschenden hohen Drücken nicht erreicht werden, um den nachteiligen Einfluss der dann auftretenden Oberflächenspannung auf die Pt-Dispersion zu vermeiden. Alle untersuchten Strukturen, d.h. Schwämme unterschiedlicher Porendichten und Porositäten und zum Vergleich kugelförmige Partikeln und ein Wabenkörper, wurden zunächst durch Tauchbeschichtung mit einer dünnen Zinndioxid-Schicht beladen. In einem zweiten Schritt wurden auf den SnO_2-beladenen Strukturen mittels überkritischer Abscheidung die Pt-Nanopartikeln aufgebracht. Die geometrischen Eigenschaften aller Strukturen blieben dabei praktisch unverändert.

Der zweite notwendige Schritt war die gewissenhafte Charakterisierung von Morphologie und Porosität der untersuchten Träger. Durch die statistische Analyse von mikroskopischen Aufnahmen wurde die Verteilung von Poren- und Stegdurchmessern der Schwämme bestimmt. Ferner wurde die Anisotropie von Poren und Zellen quantitativ erfasst, welche mit steigender Porengröße zunimmt und einen merklichen Einfluss auf den Transporteigenschaften von Schwämmen hat. Der durchschnittliche Porendurchmesser, definiert als die Summe von innerer Pore und Steg, wurde als charakteristische Länge für die Dimensionsanalyse gewählt.

Die Volumen-bezogene geometrische Oberfläche (S_{geo}, m^{-1}) der Schwämme, eine wichtige Eigenschaft für Transportphänomene, konnte mit Hilfe von bildgebender magnetischer Resonanz (Magnetic Resonance Imaging, MRI) experimentell ermittelt werden. Die geometrische Oberfläche von Schwämmen kann aus morphologischen Modellen aufgrund ihrer unregelmäßigen Natur nicht genau berechnet werden. Die experimentell durch MRI ermittelten Werte für S_{geo} sind niedriger als diejenigen, die aus dem Modell einer regelmäßigen Packung aus Tetrakaidekahedra vorhergesagt werden. In realen Schwämmen ist die geometrische Oberfläche aufgrund der Akkumulation von Feststoff in den Knotenpunkten der Stege niedriger als die eines idealen Schwamms derselben Porendichte und Porosität, der Stege mit konstantem Durchmesser hat. Außerdem verbleibt herstellungsbedingt in den Stegen ein Hohlraumanteil, der zwar keinen Einfluss auf das hydrodynamische Verhalten von Schwämmen hat, aber eine Oberflächen- oder Porositätsmessung mittels Gasadsorption stark verfälschen würde. Mit Hilfe der Quecksilberporosimetrie gelang die Unterscheidung und Messung der gesamten und der hydrodynamisch relevanten Porositäten. Alle Schwämme besitzen eine Stegporosität von ca. 22 %, was in merkliche Unterschiede zwischen der gesamten- und der äußeren (hydrodynamisch relevanten) Porosität resultiert. Erhebliche Abweichungen von bis zu 45 % in der Bettdichte (und damit auch in der Porosität) entlang der axialen Richtung eines Schwammzylinders wurden in manchen Proben beobachtet, besonders bei hohen Porendichten. Die Entfernung der keramischen Suspension aus dem Polymerschwamm während der Herstellung ist schwieriger bei kleineren Poren. Diese Erkenntnis betont die Notwendigkeit der Prozessoptimierung bei der Herstellung von Schwämmen bevor diese Strukturen in der Industrie implementiert werden können.

Die Stoffübergangseigenschaften der katalytisch beschichteten Schwämme, der Kugelschüttungen und des Wabenkörpers wurden bei 220 °C untersucht, da bei dieser Temperatur der äußere Stoffübergang die Geschwindigkeit der CO Oxidation über dem gesamten untersuchten hydrodynamischen Bereich kontrolliert. Die Bettvolumen-bezogenen Koeffizienten nehmen, wie erwartet, mit steigender Gasgeschwindigkeit zu: $k_v \sim U_0^{(0.4\ -0.5)}$. Aufgrund der mit steigender Porendichte zunehmender geometrischen Oberfläche im selben Bettvolumen, steigen die Bettvolumen-bezogenen Koeffizienten in der Reihenfolge: 10- < 20- < 30- < 45-PPI. Trotz erheblicher Unterschiedliche im Wert der geometrischen Oberfläche S_{geo} weisen alle Schwämme ähnliche Stoffübergangskoeffizienten ($k_m = k_v / S_{geo}$) auf. Die Stoffübergangskoeffizienten steigen bei konstanter Porendichte leicht mit der Porosität an. Die dimensionslosen Stofftransportkoeffizienten (Sherwood-Zahlen) nehmen mit zunehmender Porengröße bei konstanten hydrodynamischen Bedingungen (Reynolds-Zahlen) zu. Die gleiche Tendenz wurde in der Literatur bei der Evaluierung von Wärmeübergangskoeffizienten in Schwämmen (Nusselt-Zahlen) berichtet. Ein Strukturvergleich zeigte, dass die Stoffübergangsleistung von Schwämmen zwischen denen von Partikelschüttungen und Wabenkörper liegt. Stoffübergang wird in Partikelfestbetten durch die höchsten und in Wabenkörpern mit Abstand durch die niedrigsten Sh-Zahlen charakterisiert. Anders als bei Partikelschüttungen oder Wabenkörpern können aber die Stoffübergangseigenschaften von Schwämmen nicht allein mit den hydrodynamischen und Stofflichen Eigenschaften (Reynolds and Schmidt Zahlen) als einzigen Einflussgrößen einheitlich beschrieben werden. Der Grund dafür ist, dass Schwämme mit unterschiedlichen Porendichten und Porositäten nicht perfekt geometrisch ähnlich sind. Vielmehr weisen die Poren und Zellen herstellungsbedingt eine Verzerrung auf, die mit abnehmender Porendichte (PPI-Zahl) stärker ausgeprägt ist. Der zusätzliche Einfluss morphologischer Parameter wie z.B. der Poren- und Stegdurchmesser, der geometrischen Oberfläche, Porosität und Porenanisotropie auf die Stoffübergangseigenschaften wurde mittels Dimensionsanalyse evaluiert. Das Ergebnis dieser Analyse kann durch zwei alternativ verwendbare Funktionen des Typs $Sh = f(Re, Sc, \varepsilon, F_{geo})$ dargestellt werden. Die eine geometrische Funktion F_{geo} ist empirischer Natur und enthält den mittleren Porendurchmesser als zusätzliche Einflussgröße; dimensionslos wird diese Funktion aber erst durch eine Normlänge im Nenner. Die andere Korrelation ist a priori dimensionslos, da sie eine dimensionslose Anisotropiefunktion enthält. Beide Korrelation ermöglichen die Vorhersage von Stoffübergangskoeffizienten von Schwämmen mit unterschiedlichen Porendichten und Porositäten in einem weiten hydrodynamischen Bereich von $7 < Re < 1100$ mit einer Genauigkeit von ± 9 %. Die Korrelation, welche die Anisotropie mitberücksichtigt, ist physikalisch besser fundiert und stellt die korrekte Lösung des dimensionsanalytischen Problems dar. Jedoch setzt ihre Anwendung eine extrem aufwendige geometrische Charakterisierung von Poren in alle drei Raumrichtungen voraus, um die Anisotropie und Orientierung der Poren in einer repräsentativen Weise quantifizieren zu können. Die empirische Korrelation beinhaltet eine Normlänge, welche keine physikalische Bedeutung hat. Ihre Anwendung erfordert aber viel weniger Informationen über die Morphologie der Schwämme. Dies ist vorteilhafter für den Anwender. Ein metallischer Schwamm (40-PPI) mit einer totalen Porosität von 95 % wurde zum Vergleich ebenfalls untersucht. Die experimentellen Werte für *Sh* sind in sehr guter Übereinstimmung mit den von der Korrelation vorhergesagten *Sh*-Zahlen für diese Struktur. Die empirische Korrelation ist scheinbar auch bei höheren Porositäten und unterschiedlichen Materialien gut brauchbar. Eine wichtige Voraussetzung zur Benutzung der im Rahmen dieser Arbeit vorgeschlagenen Korrelationen ist nicht nur die quantitative Charakterisierung von Poren- und Stegdurchmessern, sondern auch die Kenntnis der hydrodynamisch relevanten Porosität, die aus pyknometrischen Methoden mit einer nicht benetzenden Flüssigkeit erhältlich ist.

Der Druckverlust in Schwämmen steigt mit zunehmender Porendichte und abnehmender Porosität. Die Schwammproben weisen eine nicht konstante Anzahl an verschlossenen Poren auf, was eine weitere Folge des optimierungsdürftigen Herstellungsprozesses darstellt. Die Anzahl an verschlossenen Poren hat einen wesentlichen Einfluss auf den Druckverlust und führt vor allem bei hohen Gasgeschwindigkeiten zu merkliche Abweichungen in den experimentellen Werten für den Druckverlust verschiedener Proben des gleichen Schwammtyps. Das Druckverlustverhalten von Schwämmen lässt sich, wie erwartet, mit der Forchheimer Gleichung beschreiben. Empirische Beziehungen für die Permeabilitätskonstanten als Funktion von Porendurchmesser und Porosität wurden aus den Messwerten definiert und zeigen eine starke Porositätsabhängigkeit.

Basierend auf der Analogie zwischen Stoff- (oder Wärme-) Übertragung und Druckverlust (Lévêque-Analogie), konnten die Stoffübergangskoeffizienten (*Sh*-Zahlen) mit den experimentellen Druckverlusten der Schwämme (Hagen-Zahlen) korreliert werden. Dabei wurden dieselben geometrischen Funktionen verwendet wie bei den *Sh*-*Re* Beziehungen. Die Lévêque-Analogie gilt also auch für Schwämmen und kann demzufolge für eine erste Abschätzung (Genauigkeit: ± 20 %) von Stoffübergangskoeffizienten aus Druckverlustmessungen benutzt werden.

Die Druckverlusteigenschaften von Schwämmen liegen, wie ihre Stofftransporteigenschaften, zwischen denen von Partikelschüttungen und Wabenkörpern. Ein Trade-off Index wurde eingeführt, der die gesamte Effizienz einer Struktur hinsichtlich der Kombination von maximalem Stofftransport (Umsatz) mit minimalem Druckverlust (Energieverluste) wiedergibt. Daran gemessen sind Schwämme im gesamten untersuchten hydrodynamischen Bereich erheblich besser als Partikelschüttungen (höherer Trade-off Index). Erhöhte Porositäten bei Schwämmen verbessern ihre Leistungsmerkmale, aber die mechanische Festigkeit könnte ein limitierender Faktor sein. Der Wabenkörper wies aufgrund der extrem hohen Permeabilität in den geraden Kanälen dieser Struktur den höchsten Trade-off Index aller Träger auf. Berücksichtigt man jedoch auch die Wärmetransporteigenschaften, so sind Schwämme aufgrund ihrer tortuosen Struktur und der damit verbundenen, verbesserten radialen Konvektion sowie der verbesserten Strahlung bei hohen Temperaturen den anderen Packungen klar überlegen. Insbesondere in Wabenkörpern hat der unvermischte Fluss entlang der Kanäle wesentlich stärkere Temperaturgradienten zufolge. Dies ist kritisch bei der Benutzung dieser Strukturen in stark exothermen oder endothermen Prozessen, da inhomogene Temperaturverteilungen die Produktselektivität und die Lebensdauer des Katalysators stark beeinträchtigen können.

Durch die günstige Kombination von verbessertem Stoffübergang, mäßigem Druckverlust und ausgezeichnetem Wärmetransport sind Schwämme eine sehr attraktive Alternative zu konventionellen katalytischen Trägern in technischen Anwendungen wie zum Beispiel die Abgasbehandlung, die on-board Wasserstoffherstellung oder industrielle chemische Synthesen mit starker Wärmetönung.

7 Appendix

A : Axial dispersion

B : H_2-chemisorption

C : CO adsorption capacity

D : Pore and strut size distributions of the sponges

E : Diffusion in gases at moderate pressures

F : The Buckingham-Theorem

G : Correlation matrix and confidence intervals of the general correlation

H : Publications, presentations and related studies

I : Used symbols and abbreviations

A Axial dispersion

Catalyst performance data interpretation presupposes ideal hydrodynamic flow behaviour of the reactor system. The occurrence of axial dispersion must be hence avoided. Axial transport effects within the reactor as a whole are particularly difficult to evaluate and control. A common approach for the minimization of these effects is to adopt the differential reactor, in which low conversions are taken. The alternative of the recycle reactor, used in this work, provides means of operating differentially while maintaining a finite overall conversion. At high recycle flow rates, the influence of dispersion can be usually neglected, since the system is operating close to the conditions of a continuous stirred tank reactor (CSTR). Nevertheless, since the recycle flow rate was varied over a wide range in order to analyze mass transfer coefficients at different hydrodynamic conditions, the influence of axial dispersion has to be evaluated. In comparison to ideal plug flow conditions along the reactor, the mass balance of a differential volume element has to be extended by the dispersion term, having the same form as Fick´s law (one-dimensional), since the dispersion flux is proportional to the concentration gradient:

$$0 = -U_0 \cdot \frac{dC_i}{dz} + \boldsymbol{D_{ax}} \cdot \frac{\boldsymbol{d^2 C_i}}{\boldsymbol{dz^2}} - k_v \cdot C_i \,, \qquad (7.1)$$

where D_{ax} is the axial coefficient of dispersion. The analytical solution to this problem, under assumption of axial dispersion at reactor entrance (lower inlet concentration at $z = 0$) and no reaction at the outlet (no concentration gradients at $z = L$) reads [1,2]:

$$\frac{C_{i,out}}{C_{i,in}} = \frac{4 \cdot a \cdot \exp(Bo/2)}{(1+a)^2 \cdot \exp\left(\frac{a \cdot Bo}{2}\right) - (1-a)^2 \cdot \exp\left(-\frac{a \cdot Bo}{2}\right)} \,, \qquad (7.2)$$

with

$$Bo = \frac{U_0 \cdot L}{D_{ax}} \qquad (7.3)$$

and

$$a = \sqrt{1 + \frac{4 \cdot k_v \cdot \tau}{Bo}} \,. \qquad (7.4)$$

In the case of the plug flow reactor with external recycle (chapter 2), the reactor (not system) inlet concentration $C_{i,in}$ is not readily known, but can be calculated from the mass balance at the mixing point of the recycle as a function of the system CO conversion and the recycle ratio to (i = CO):

$$\frac{C_{CO,out}}{C_{CO,in}} = \frac{(1-X_{CO})\cdot(1+R)}{1+R\cdot(1-X_{CO})} \tag{7.5}$$

Equating eq. (7.2) with eq. (7.5) gives an implicit equation for the volumetric rate coefficient k_v as a function of measurable quantities and the still unknown axial dispersion coefficient D_{ax}. A well accepted correlation for the axial dispersion coefficient of particle packings is given in [3]. Nevertheless, there are, to the knowledge of the author, no correlations for the axial dispersion coefficients upon flow through sponges. The first approach towards this direction was done within a project from the sponge research group FOR 583, on the basis of residence time distribution measurements of 20-, 30- and 45-PPI sponges at low superficial velocities ($Re < 8$). Starting from the same functional dependence on fluid velocity, molecular diffusion coefficient and characteristic length as in the correlation for packed beds of particles, following relation for the calculation of dispersion coefficients in sponges was proposed:

$$D_{ax} = 0.3\cdot D_{AB}(T) + \frac{6.853\cdot 10^{-5}\cdot Re}{1+1.5\cdot 10^{5}\cdot \dfrac{D_{AB}(T)}{Re}} \tag{7.6}$$

In the low Reynolds regime analyzed, the dispersion in ceramic sponges appears to be considerably higher than in particle packings of similar surface area. It can not be confirmed to this point whether the correlation given above can be extrapolated for Reynolds up to 1000. Nevertheless, being this relation the only one available, it was used for a worst case evaluation. At high Reynolds numbers, the effect of axial dispersion is not relevant, since the reactor system is operating at conditions near CSTR. Moreover, eq. (7.6) displays the worst scenario (highest dispersion), since it predicts considerably higher dispersion coefficients than the relation for packed beds. The author also observed lower dispersion in some sponges, not being able to correlate for instance the low dispersion degrees of 20-PPI sponges to the high dispersion degrees predicted from the relation, which was developed from data of 30- and 45-PPI sponges.

With calculated values for D_{ax}, the implicit equation for the volumetric mass transfer coefficient k_v was iterated starting from the coefficient of the ideal PFR with external recycle. The values for Bo are nearly independent of Re, since both D_{ax} and U_0 increase with the superficial velocity. The evaluation was performed on a 20-PPI sponge at two different Bodenstein numbers by varying the sponge bed length from 20 – 100 mm. At Bodenstein numbers of approx. 30 (L = 100 mm), deviations from the ideal PFR-recycle system are merely 2.35 % in the worst case (lowest *Re*). At the lowest analyzed bed length (Bo = 7), the highest deviation of the rate coefficients was 8.7 %, as displayed in Table 7.1.

Table 7.1: Worst case scenarios at two different Bo for the influence of axial dispersion in the 20-PPI sponge with 80 % porosity.

Bo	U_0 [m/s]	D_{ax} [m^2/s]	$k_{v,ideal}$ [s^{-1}]	$k_{v,disp}$ [s^{-1}]	***deviation*** **[%]**
34.2	1.27	0.0037	230.3	235.7	**2.35**
7.3	1.96	0.0062	273.4	297.2	**8.7**

The slopes of the volumetric coefficients over the superficial velocity at the lowest *Bo*, with and without the influence of dispersion included in the reactor system description, are plotted in Figure 7.1. Even in the worst case of dispersion, the difference in the values for k_v is lower than the deviations observed between different samples due to irregularities, as was presented in chapter 4. Finally, it can be observed from the figure that neglecting dispersion represents, in any case, the worst case scenario for the mass transfer coefficients.

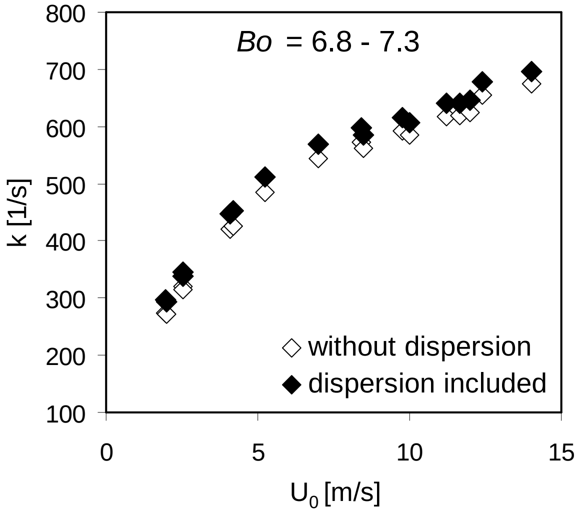

Figure 7.1: Volumetric mass transfer coefficients k_v of a 20-PPI_0.8 versus superficial gas velocity, with and without the influence of dispersion included in the reactor system.

In this work, the most commonly used bed lengths for evaluation of mass transfer coefficients were 60 – 80 mm, resulting in a maximum deviation of approx. 5 %. It can be therefore concluded, that the influence of axial dispersion on the mass transfer data analyzed herein can be neglected.

B H_2-chemisorption

The purpose of the H_2-chemisorption is to determine the content of active platinum and its dispersion on the surface of tin dioxide wash-coated α-Al_2O_3.

H_2-chemisorption is a method based on the determination of the number of probe gas molecules adsorbing on the surface atoms of platinum with, for each probe gas (O_2 or H_2), a specific stoichiometry factor. Determination of stoichiometric factors is, however, a great challenge deeply studied during the last decades. Authors such as O´Rear et al. investigated stoichiometry for the adsorption of oxygen and hydrogen, as well as the titration by molecular hydrogen of adsorbed oxygen on platinum [4]. O´Rear et al. considered the three following steps for the calculation of the stoichiometric factors:

I. Adsorption of oxygen on platinum.

II. Reaction of adsorbed oxygen and hydrogen to build up water.

III. Adsorption of hydrogen on platinum.

Comparing platinum particle sizes calculated by H_2-chemisorption and those measured by x-ray techniques, they obtained the following average number of adsorbed hydrogen atoms (y_H) or oxygen atoms (x_O) per surface platinum atom:

H-Pt: $y_H = 1.10$

O-Pt: $x_O = 0.71$

The value of y_H seems to be well accepted in literature, whereas x_O varies between 0.5 and 0.7. However, even if x_O varied from 0.5 to 1, maximum deviation in calculating dispersion of the metal would not be higher than 20 %. Considering these variations, acceptable stoichiometric factors measured by O´Rear et al. were taken for our calculations. Knowing that two hydrogen atoms react with one oxygen atom adsorbed on platinum and 1.10 hydrogen atoms react with one platinum atom, the number of hydrogen atoms consumed per platinum atom is the following: $2 \cdot 0.71 + 1.10 \cong 2.5$. The value of 2.5 was used in eq. (7.9) to calculate the number of active platinum moles, known the number of consumed hydrogen moles.

For this work, H_2-chemisorption was held in a temperature program apparatus (TPX) attached to a mass spectrometer to analyze the composition of the exiting gas and connected to a PC.

The program defined in the TPX was the following:

- Oxidation with oxygen (preparation gas): 220 ºC, 40 minutes.

- Flowing with argon (carrier gas): 50 ºC, 3 hours, to desorb physically adsorbed oxygen.
- Injection of 1,05 ml loop gas (5% hydrogen in argon): 50 ºC, 60-90 peaks, every 15 minutes.

Samples were placed in a glass reactor, attached to the TPX and carefully isolated to avoid temperature gradients. Program was started from the PC and data was directly stored.

For each sample measured, the dispersion of platinum, defined as the ratio between active platinum and total platinum, both expressed in mass percentages, was calculated according to the following calculation schema:

$$D_{Pt} = \frac{\%Pt_{active}}{\%Pt_{total}} \tag{7.7}$$

$\%Pt_{total}$ is directly measured means x-ray fluorescence and $\%Pt_{active}$ can be calculated as a function of the platinum molecular weight, the number of active platinum moles ($n_{activePt}$) and the mass of the sample to:

$$\%Pt_{active} = \frac{n_{activePt} \cdot \tilde{M}_{Pt}}{m_{sample}} \cdot 100 \tag{7.8}$$

The number of active platinum moles is not directly measured but can be obtained from the number of adsorbed peaks (P_{ads}) and the number of moles of atomic hydrogen present in one injected peak, $n_H / peak$. The following equations were used:

$$n_{activePt} = \frac{P_{ads} \cdot n_H / peak}{2.5} \tag{7.9}$$

$$n_{H2} / peak = \frac{p_{H2} V}{RT} \tag{7.10}$$

$$P_{ads} = P_{total} - P_{rest} = P_{total} - \frac{A_{total}}{A_{peak}} \tag{7.11}$$

where A_{total} represents the total area under the chemisorption curve, and A_{peak} the area of one injected pulse.

Considering the experimental conditions selected for the H_2-chemisorption (T = 50 °C; p = 0.05·101.3 kPa; V = 1.05 ml), the calculated number of hydrogen moles contained in each peak was 1.98 mol H_2 / peak.

Results

Two samples were analyzed with hydrogen chemisorption, one catalyst from aqueous deposition and one from supercritical deposition (SFRD 1 conditions). Three to five measurements were carried out for each sample. For each measurement five different calculation variants were used, by modifying the H_2 baseline. The definitive results, taken as the average values of all calculations, are shown in Table 7.2:

Table 7.2: Platinum dispersion in SFRD 1 wet-impregnated catalysts.

Sample	$\%Pt_{active}$	$\% Pt_{total}$	D_{Pt}
	[g Pt_{active} / g sample]	[g Pt_{total} / g sample]	[$\%Pt_{active}$ / $\%Pt_{total}$]
SFRD 1	0.774	0.487	1.59
Aqueous deposition	0.983	0.388	2.53

First surprising result was to find out that, for both samples, the apparent amount of active platinum was higher than the amount of total platinum, leading to dispersions higher than 1. These contradictory results can be justified by the reduction of a significant part of the tin dioxide, which is catalyzed by platinum [5]. The reduction of tin dioxide implies a hydrogen consumption that cannot be predicted, because the amount of reduced tin dioxide is unknown. Consequently, the H_2-chemisorption method is not appropriate to compare the amount of active platinum and its dispersion in both catalysts, since tin dioxide reduction might occur to a different and not controllable extent in the analyzed catalysts.

Second surprising result is the fact, that apparent dispersion in the wet-impregnated catalyst from aqueous deposition was 1.6 times higher than in the SFRD 1 catalyst, contradicting previous results by SEM/EDX and TEM/EDX analysis, as well as those revealed in the kinetic studies. There are not clear reasons to explain such behaviour, but it seems to be a consequence of the chemisorption method, which does not seem to be appropriate for the chemical system under study. Since the reduction of part of the tin dioxide is not directly measurable and introduces important deviations (up to 40 %) in the values of the dispersion degrees of one sample, H_2-chemisorption method does not seem to be suitable to determine the active platinum content when tin dioxide is present.

C CO adsorption capacity

In a second attempt to characterize the platinum distribution, the CO adsoption capacity of two catalysts from the same deposition methods as in the case of H_2-chemisorption (SFRD 1 and aq. deposition) was evaluated following the method already used by Grass and Lintz on the catalytic system Pt/SnO_2 [6].

The sample to analyze was placed in a tubular reactor, flushed for 1 h in a mixture of 1 % CO in N_2, subsequently swept with pure nitrogen for 20 min and finally flushed with 5 % O_2 in nitrogen. In this last step, the adsorbed carbon monoxide reacts with the oxygen to form carbon dioxide. The experiment is finished, when the amount of exiting CO_2, measured with a non dispersive infrared analyzer (NDIR), equals zero or remains constant for 1 h. The quantity of adsorbed CO is obtained from the measured quantity of evolved CO_2:

$$n_{CO} = n_{CO_2} = \int_{t_0}^{t} \dot{n}_{CO_2,ex} \cdot dt = \dot{V}_0 \int_{t_0}^{t} C_{CO_2,ex} \cdot dt\,, \tag{7.12}$$

where $\dot{V}_0$ is the inlet volume flow rate and $C_{CO2,ex}$ is the time dependent exiting concentration of carbon dioxide.

The CO adsorption capacity is then defined as the total amount of adsorbed CO divided by the mass of the catalyst:

$$\Gamma_{CO} = \frac{n_{CO}}{m_{Kat}} \quad [\text{mol/g}]. \tag{7.13}$$

Supposing that CO adsorbs merely on Pt, the values of Γ_{CO} can be used to calculate the apparent dispersion degree of platinum D_{Pt}:

$$D_{Pt} = \frac{\Gamma_{CO} \cdot 1.2 \cdot \tilde{M}_{Pt}}{w_{Pt}}\,, \tag{7.14}$$

where 1.2 is the average number of adsorbed CO molecules per surface platinum atom [7] and w_{Pt} is the platinum weight fraction of the sample, obtained from x-ray fluorescence analysis.

The experiments were repeated four times for each catalyst at different temperatures to exclude the influence of thermal desorption of the adsorbed CO. The obtained results are summarized in Table 7.3. In catalyst from SFRD 1, desorption effects have no influence in the temperature range investigated. The values for the adsorption capacity and the resulting dispersion degree remain nearly constant. The apparent dispersion degree of Pt in this catalyst is approx. 20 %. The upper plot in Figure 7.2 displays the slopes of the CO_2 outlet concentrations at different temperatures. The peaks appear in shorter time and more pronounced at higher temperatures, as expected from the enhanced surface diffusion of the adsorbed species with increasing temperature.

Table 7.3: Results from CO adsorption capacity measurements of catalysts from two different deposition methods at different temperatures.

Sample	w_{Pt} [%]	T [°C]	n_{CO2} [mol]	Γ_{CO} [mol/g]	D_{Pt} [-]
SFRD 1	0.45	45	$3.97\cdot10^{-06}$	$3.90\cdot10^{-06}$	0.20
SFRD 1	0.45	50	$3.74\cdot10^{-06}$	$3.68\cdot10^{-06}$	0.19
SFRD 1	0.45	55	$4.10\cdot10^{-06}$	$4.03\cdot10^{-06}$	0.21
SFRD 1	0.45	70	$3.81\cdot10^{-06}$	$3.74\cdot10^{-06}$	0.19
Aq. dep.	0.51	55	$1.12\cdot10^{-06}$	$1.79\cdot10^{-06}$	0.08
Aq. dep.	0.51	70	$1.87\cdot10^{-06}$	$2.99\cdot10^{-06}$	0.14
Aq. dep.	0.51	80	$3.23\cdot10^{-06}$	$5.17\cdot10^{-06}$	0.24
Aq. dep.	0.51	105	$4.05\cdot10^{-06}$	$6.48\cdot10^{-06}$	0.30

Very different results were obtained in the case of the sample from aqueous deposition, were the adsorption capacity seems to increase with increasing temperature. The reason for these contradictory results can be found in the slopes of the time dependent exiting CO_2 concentration (Figure 7.2). Whereas the CO_2 concentration decreases to cero after 140 s in the case of the catalyst from supercritical deposition, an extremely pronounced tailing is observed in the low temperature range of the sample from aq. deposition. Even over 300 s after titration, the CO_2 concentration had not yet decreased to cero, but remained at a barely measurable value of 0.1 %. The only reason that could explain these extremely broad slopes is the longer diffusion paths for the CO that is adsorbed on Pt. Since the lowest temperature chosen for the conventional prepared catalyst was 55 °C, where the peak in the case of the sample from SFRD was very pronounced, the only reason can be the larger Pt-crystals present in the catalyst from aq. deposition (confirmed with TEM analysis). It also explains the characteristic plateaus observable at 70 °C and 80 °C. After the CO adsorbed on platinum near the phase boundary line Pt/SnO_2 has migrated to the line and reacted with the adsorbed oxygen, the remaining CO, adsorbed in the central part of a large Pt crystal, needs to migrate to the phase boundary before being able to react again. The larger the particles, the longer the diffusion paths and the broader the plateaus will be. This is most probably the reason for the pronounced plateaus in the conventional catalyst at temperatures where the SFRD catalyst shows a steep peak.

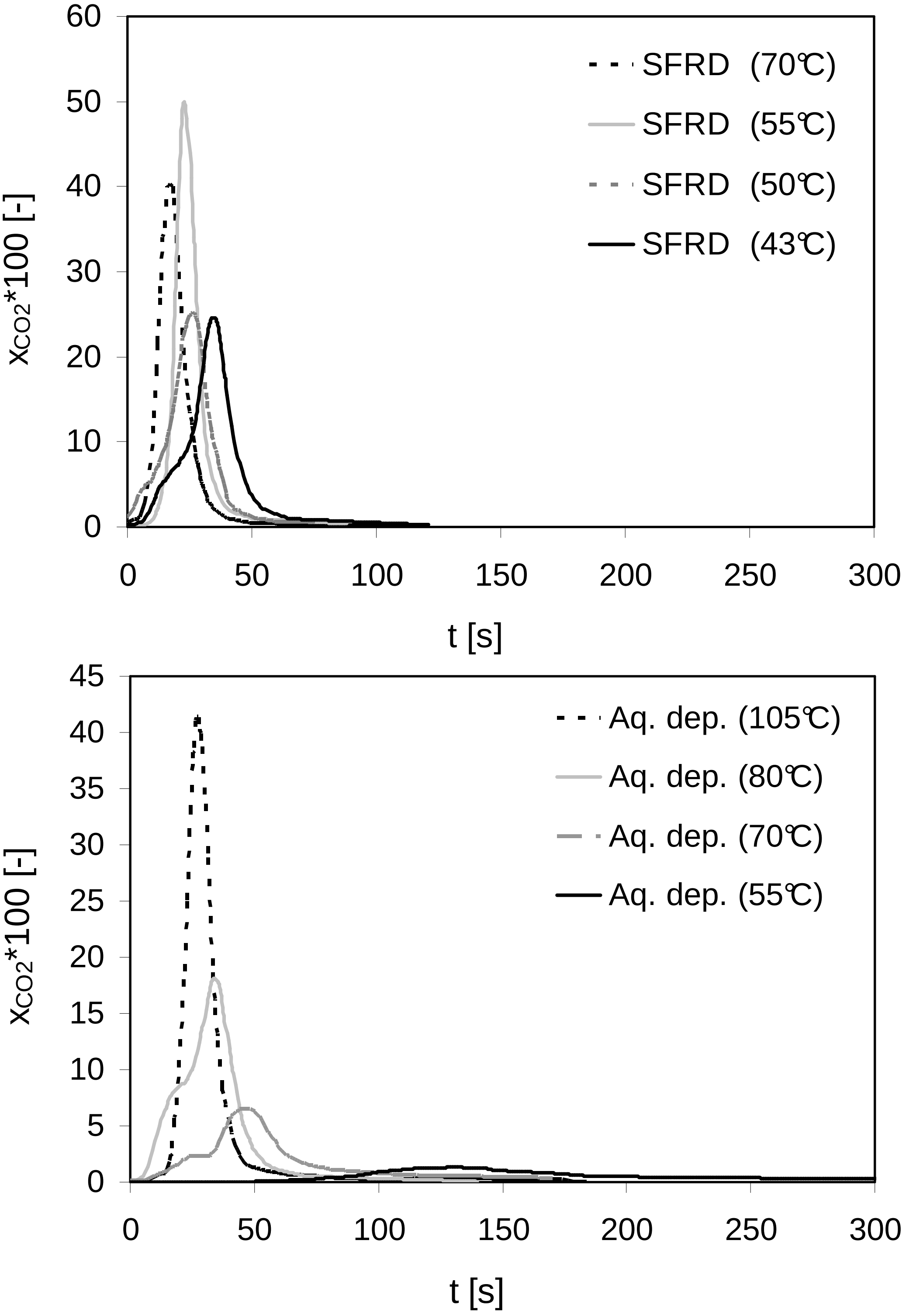

Figure 7.2: *Time dependent CO_2 outlet concentrations in the titration of adsorbed CO by O_2. Upper diagram: sample from SFRD 1; lower diagram: sample from aqueous impregnation.*

Nevertheless, at higher temperatures the measured CO adsorption capacity and apparent dispersion degree of platinum is higher in the case of the catalyst from aq. deposition, in contradiction to the results of the more representative characterization with TEM and SEM. There is no clear explanation for this controversy. A possible explanation is the fact that the adsorption capacity of carbon monoxide should be proportional to the total area available for adsorption, which is not necessarily higher at higher dispersions. The dispersion of Pt increases the phase boundary line between Pt and SnO_2, which can not be easily characterized by any method known to the author. Another possibility is the weaker interaction between CO and highly dispersed platinum in contrast to the strong interaction between CO and crystalline Pt, causing an elevated loss of adsorbed CO during the flushing period with N_2.

Lastly, the slopes of the exiting CO_2 concentrations were, in some cases, not reproducible upon measurement repetition. A more profound and extensive study would reveal all these remaining interrogatives. Nevertheless, the present research was not devoted to the chemical characterization of catalysts and SEM- as well as TEM-analysis gave insight to important information regarding the surface morphology and Pt-distribution of the catalysts under study.

D Pore and strut size distributions of the sponges

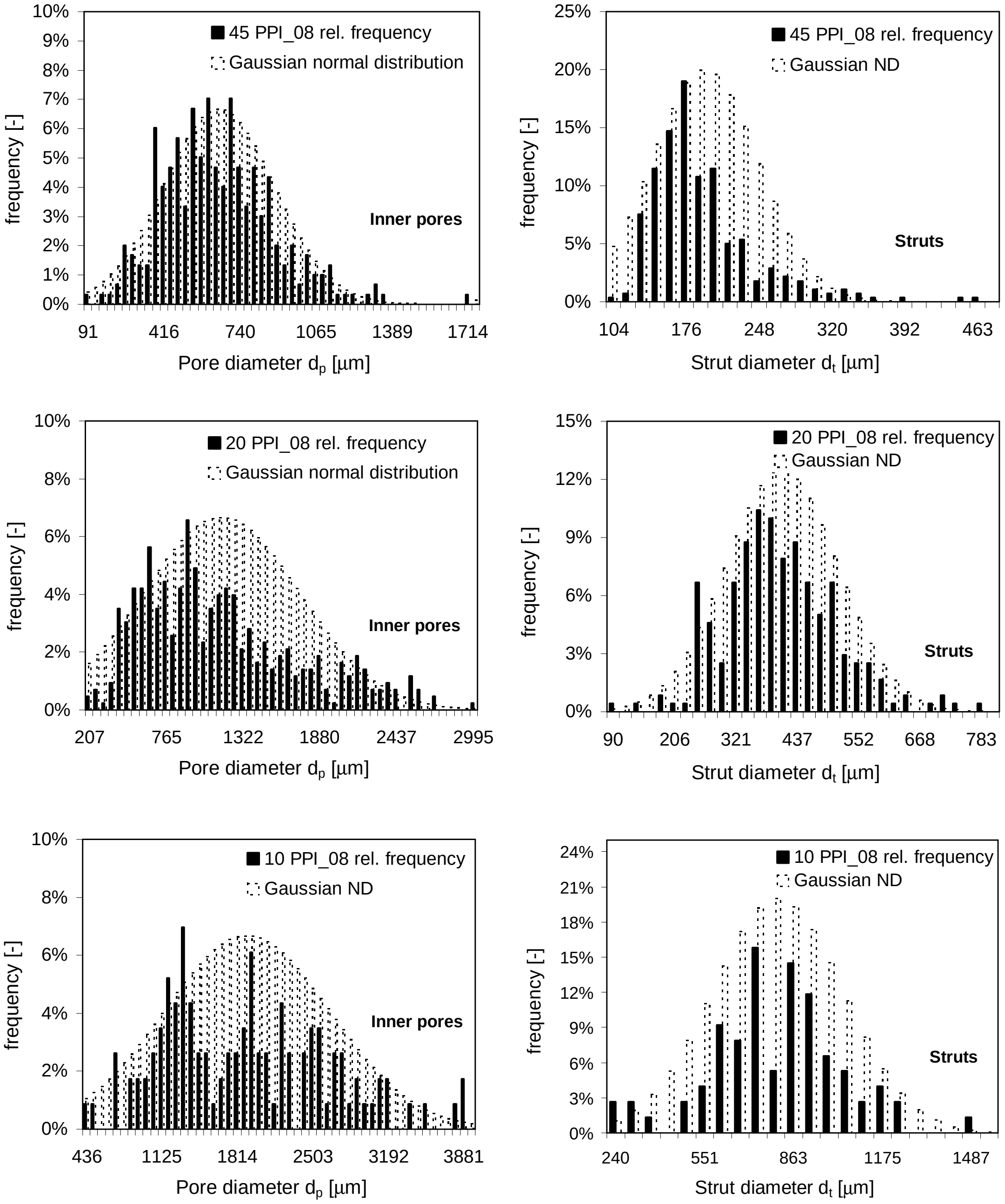

Figure 7.3: *Inner pore- and strut size distribution of ceramic sponges with 80 % porosity. Sponges with 85 % porosity show similar distributions of one order of magnitude (inner pores).*

E Diffusion in gases at moderate pressures

Prediction of diffusion coefficients has been subject of great interest in the last century due to the importance of gaseous diffusion in a wide variety of chemical processes. Fuller et al. [8] proposed a quite reliable method for the prediction of binary gas-phase diffusion coefficients based on the Stefan-Maxwell hard sphere model and the principle of additive atomic volumes. The parameters of the correlation given were obtained from a non linear least square analysis of 153 different binary systems, including 340 actual data points. The equation selected by the authors from the least square analysis reads:

$$D_{AB} = \frac{10^{-3} \cdot T^{1.75} \cdot \left(\frac{1}{\tilde{M}_A} + \frac{1}{\tilde{M}_B} \right)^{1/2}}{p \cdot \left(\upsilon_A^{1/3} + \upsilon_B^{1/3} \right)} \tag{7.15}$$

with

D_{AB}	:	binary gas-phase diffusion coefficient	[m^2/s]
T	:	temperature	[K]
p	:	pressure	[N/m^2]
$\tilde{M}_i$	:	molar mass of component *i* in the mixture	[g/mol]
υ_i	:	diffusion volume	[-]

The 1.75 temperature dependence represents a compromise value giving reasonable agreement for most binary systems. Observed values for the power dependence on temperature lie in the range 1.6 – 1.8. Optimized values for diffusion volumes of simple molecules and atomic diffusion volumes to be applied additively can be found elsewhere [8,9].

F The Buckingham-Theorem

The Π-Theorem, or Buckingham-Theorem asserts that any complete physical relation

$$z = f(X_1,..........,X_n) \tag{7.16}$$

can be represented as one substituting between a set of dimensionless independent products of the measures of the influencing quantities [10]:

$$Z = X_1^{n_1} \cdot X_2^{n_2} \cdot .... \cdot X_k^{n_k} \cdot F(\Pi_1,\Pi_2,.....,\Pi_m) \qquad \text{(and } m = n - k\text{)} \tag{7.17}$$

Where Z is the desired dimensional physical quantity and X_j are the result influencing data. F is a dimensionless function of the independent dimensionless product combinations of the data Π_j. The exponents n_j are real numbers fulfilling the constraint:

$$[X_1^{n_1} \cdot X_2^{n_2} \cdot .... \cdot X_k^{n_k}] \overset{!}{=} [Z] \tag{7.18}$$

Furthermore, another considerable advantage achievable through the use of this theorem is the reduction of the arguments in the dimensionless function F, as displayed in eq. (7.17), which is the case when the first subset (X_1-X_k) of arguments in f (eq. (7.16)) has physical parameters with independent dimensions, i.e. from which no dimensionless Π-product can be defined. The mathematical proof of the fundamental theorem described above can be found elsewhere [10,11].

G Correlation matrix and confidence intervals of the general correlation

Table 7.4 and Table 7.5 show the correlation matrix of the fitted parameters and the values for the parameters with their confidence intervals, respectively. The non linear square optimization of the parameters in the case of the general correlation, that includes the influence of the pore anisotropy, yielded the same accuracy and very similar correlation of the parameters as the empirical correlation.

Table 7.4: Symmetric correlation matrix C of the 4 estimated parameters of the general correlation for the prediction of mass transfer coefficients of ceramic sponges.

	A	*B*	*p*	*q*
A	1	-0.727	0.066	0.675
B	-	1	-0.489	-0.035
p	-	-	1	-0.385
q	-	-	-	1

Table 7.5: Estimated parameters and confidence intervals of the general correlation for the prediction of mass transfer coefficients of ceramic sponges.

Parameter	Value	Confidence interval (95 %)
A	**0.81**	± 0.04
B	**0.47**	± 0.01
p	**0.84**	± 0.02
q	**0.43**	± 0.12

H Publications, presentations and related studies

Publications:

F. C. Patcas, G. Incera Garrido, B. Kraushaar-Czarnetzki, *CO oxidation over structured carriers: A comparison of foams, honeycombs and beads*, Chem. Eng. Sci. 62 (2007) 3984 – 3990.

G. Incera Garrido, F. C. Patcas, G. Upper, M. Türk, S. Yilmaz, B. Kraushaar-Czarnetzki, *Supercritical deposition of Pt on SnO_2-coated Al_2O_3 foams: Phase behaviour and catalytic performance*, Appl. Catal. A 338 (2008) 58 – 65.

G. Incera Garrido, F. C. Patcas, S. Lang, B. Kraushaar-Czarnetzki, *Mass transfer and pressure in ceramic foams: A description for different pore sizes and porosities,* manuscript accepted in Chem. Eng. Sci. (2008).

Presentations in conference proceedings:

Oral presentations

G. Incera Garrido, F. C. Patcas, S. Yilmaz, B. Kraushaar-Czarnetzki, *The CO oxidation over structured catalyst packings: a comparison of foams, honeycombs and beads*, 39th German Conference on Catalysis, March 19-21, 2006, Weimar, Germany.

G. Incera Garrido, F.C. Patcas, G. Upper, M. Türk, B. Kraushaar-Czarnetzki, *Activity, mass transfer and pressure drop of ceramic foams functionalized by supercritical platinum deposition*, 7th International Exhibition-Congress on Chemical Engineering and Biotechnology, Achemasia, May 14 – 18, 2007, Beijing, People’s Republic of China.

G. Incera Garrido, S. Lang, F.C. Patcas, B. Kraushaar-Czarnetzki, *Mass transfer- and pressure drop properties of catalytic sponge structures*, German Conference on Reaction Engineering (Jahrestreffen Reaktionstechnik), May 18 – 20, 2008, Würzburg, Germany.

Poster presentations

G. Incera Garrido, F. C. Patcas, G. Upper, M. Türk, B. Kraushaar-Czarnetzki, *Preparation of Pt/SnO2 catalysts for CO-Oxidation: Comparison between conventional and supercritical Pt deposition*, 40th Annual Conference of German Cataysts, March 14-16, 2007, Weimar, Germany.

Related studies (student works):

Beatriz González Presmanes, *Pt supported catalysts for the CO oxidation at moderate temperatures*, diploma thesis, University of Karlsruhe (TH), 2006.

Heinz Tristan Gund, *Charakterisierung und Stoffübergangseigenschaften von* Al_2O_3*-Schwammstrukturen*, semester work, University of Karlsruhe (TH), 2007.

Sebastian Lang, *Stoffübergangs- und Druckverlusteigenschaften katalytischer Schwammstrukturen*, diploma thesis, University of Karlsruhe (TH), 2007.

I Used symbols and abbreviations

A	empirical solubility constant of a mixture	[-]
A	pre-exponential parameter in dimensionless correlation	[-]
A_i	total are of substance I	[m^2]
B	empirical solubility constant of a mixture	[-]
B	exponent in Reynolds number (Re)	[-]
$\vec{B}_{0,1,z}$	magnetic fields	[T]
C	relative correlation matrix	[-]
C_{ij}	relative covariance element (i,j) in the correlation matrix	[-]
$C_{CO,0}$	system inlet CO concentration	[mol/m^3]
$C_{CO,in}$	reactor inlet CO concentration	[mol/m^3]
$C_{CO,out}$	outlet CO concentration	[mol/m^3]
c_D	drag coefficient	[-]
c_F	friction factor (< c_D), external flow	[-]
c_p	heat capacity	[J/(g·K)]
D, d	diameter	[m]
d_P	inner pore diameter	[m]
d_t	strut diameter	[m]
d_w	wall thickness (honeycomb)	[m]
D_t	tube diameter	[m]
D_p	mean pore diameter	[m]
D_h	hydraulic diameter	[m]
D_{AB}	molecular diffusion coefficient	[m^2/s]
D_{ax}	axial dispersion coefficient	[m^2/s]
D_{Pt}	platinum dispersion degree	[-]
E	deposition degree	[-]
E_a	activation energy	[kJ/mol]
F_g	dimensionless geometrical function	[-]
$F_{g,A}$	dimensionless geometrical function including the anisotropy	[-]
f	friction factor	[-]

f_1	viscous constant	[Pa·s/m^2]
f_2	inertial constant	[Pa·s^2/m^3]
$\vec{G}_i$	magnetic gradient in the direction I	[T/m]
h	heat transfer coefficient	[W/(m^2·K)]
I	trade-off index (mass transfer / pressure drop)	[-]
$\vec{I}$	macroscopic angular momentum	[J·s]
$j_{H,D}$	Chilton-Colburn heat- and mass transfer factors	[-]
J	jacobian matrix	[-]
J_A	diffusive flux density of molecules A	[mol/(m^2·s)]
k_V	volumetric rate coefficient based on the bulk volume	[s^{-1}]
k_m	mass transfer coefficient gas/solid	[m/s]
k_{Pt}	rate coefficient of reaction relative to Pt	[m^3/(g$_{\mathrm{Pt}}$·s)]
k_1	viscous permeability parameter	[m^2]
k_2	inertial permeability parameter	[m]
$\vec{k}$	wave vector	[1/m]
L	length	[m]
m	mass	[kg]
m	parameter in F_g	[-]
$\tilde{M}_i$	molecular weight of substance of substance I	[g/mol]
$\vec{M}$	magnetization	[J/T]
n	parameter in F_g	[-]
$\dot{n}_i$	absolute molar flux of component i	[mol/s]
N	number of experimental points for mathematical modeling	[-]
N_A	Avogadro constant	[mol^{-1}]
p	pressure	[Pa]
Δp	pressure drop	[Pa]
P_s	solid perimeter	[m]
P	hydrogen peaks (H_2 chemisorption)	[-]
p	parameter in $F_{g,A}$	[-]
q	parameter in $F_{g,A}$	[-]

q	heat flux density	[W/m^2]
R	recycle flow rate ratio	[-]
r_v	bulk volume based reaction rate	[mol/(m^3·s)]
S_{geo}	geometric surface area per bed volume	[m^2/m^3(bed)]
S_i	specific surface area of substance *i*	[m^2/g]
T	temperature	[°C]
U_0	superficial velocity	[m/s]
$\dot{V}$	flow rate	[m^3/s]
V	volume	[m^3]
V	variance-covariance matrix	[-]
w_i	weight fraction of component *i*	[-]
X_{CO}	carbon monoxide conversion	[-]
x_f	frictional fraction (c_F/c_D)	[-]
Y_A	molar fraction of substance *A*	[-]
Greek letters		
γ	surface tension	[N/m]
γ	gyromagnetic ratio	[rad/s·T]
Γ_{CO}	CO adsorption capacity	[mol/g]
ε_t	total porosity	[-]
ε_h	outer- or hydrodynamic relevant porosity	[-]
θ	contact angle	[-]
η	dynamic viscosity	[Pa·s]
λ	thermal conductivity	[W/(m·K)]
ν	kinematic viscosity	[m^2/s]
$\vec{\omega}$	angular frequency	[s^{-1}]
ρ	density	[kg/m^3]
σ	root mean square deviation	[m]
τ	shear stress	[N/m^2]
ξ	darcy friction factor	[-]
ψ	tolerance of the parameter fitting	[-]

Dimensionless groups

$Bo = \frac{U_0 \cdot L}{D_{ax}}$	Bodenstein number
$Hg = \frac{\xi}{2} \cdot Re^2 = \frac{\Delta p}{\Delta L} \cdot \frac{D_p^3}{\rho \cdot \nu^2}$	Hagen number
$j_D = \frac{k_m}{U_0} \cdot Sc^{2/3}$	Chilton-Colburn mass transfer factor
$j_H = \frac{h}{c_p \cdot \rho \cdot U_0} \cdot Pr^{2/3}$	Chilton-Colburn heat transfer factor
$Lq = 2 \cdot x_f \cdot Hg \cdot Pr \cdot \frac{D_h}{L}$	Lévêque number
$Nu = \frac{h \cdot D_p}{\lambda}$	Nusselt number
$Pr = \frac{\eta \cdot c_p}{\lambda}$	Prandtl number
$Re = \frac{U_0 \cdot D_p}{\nu}$	Reynolds number
$Sh = \frac{k_m \cdot D_p}{D_{1,2}}$	Sherwood number
$Sc = \frac{\nu}{D_{1,2}}$	Schmidt number
$St = \frac{k_m}{U_0}$	Stanton number

Abbreviations

AARD	absolute average relative deviation
BET	Brunauer-Emmett-Teller
CC	cubic cell
cov	covariance of parameters
COD	cyclooctadien
CPSI	channels per square inch
CSTR	continuous stirred tank reactor

Dev	deviation
EDX	energy dispersive x-ray
GHSV	gas hourly space velocity
MRI	magnetic resonance imaging
NDIR	non dispersive infrared
NMR	nuclear magnetic resonance
PFR	plug flow reactor
PPI	pores per inch
PROX	preferential oxidation
PTFE	polytetrafluoroethylene
RMSD	root mean square deviation
sc	supercritical
SCF	supercritical fluids
SEM	scanning electron microscopy
SFRD	supercritical fluid reactive deposition
STP	standard temperature and pressure
TEM	transmission electron microscopy
TPD	temperature programmed desorption
TTKD	tetrakaidecahedron
Var	experimental error variance
var	variance of the parameter
XRF	x-ray fluorenscence

References

[1] O. Levenspiel, *The chemical reactor omnibook*, Oregon St. Univ. Bookstores, 1993.

[2] J. F. Wehner, R. H. Wilhelm, *Boundary conditions of flow reactor*, Chem. Eng. Sci. 6 (1956) 89 – 93.

[3] C. Y. Wen, L. T. Fan, *Models for flow systems and chemical reactors*, Marcel Dekker, Inc., 1975.

[4] D.J. O´Rear, D. G. Löffler, M. Boudart, *Stoichiometry of the titration by dihydrogen of oxygen adsorbed on platinum*, J. Catal. 121 (1990) 131 – 140.

[5] J. E. Drawdy, G. B. Hoflund, S. D. Gardner, E. Yngvadottir, D. R. Schryer, *Effect of pretreatment on a platinized tin oxide catalyst used for low temperature CO oxidation*, Surf. Interface Anal., 16 (1990) 369 – 374.

[6] K. Grass, H.-G. Lintz, *The kinetics of carbon monoxide on tin(IV) oxide supported platinum catalysts*, J. Catal., 172 (1997) 446-452.

[7] K. Grass, *Synergismus von Platin und Zinndioxid bei der katalytischen Oxidation von Kohlenmonoxid bei Umgebugstemperatur*, Dissertation, University of Karlsruhe (TH), 1996.

[8] E. N. Fuller, P. D. Schettler, J. C. Giddings, *A new method for prediction of binary gas-phase diffusion coefficients*, Ind. Eng.Chem. 58 (1966) 18 – 27.

[9] VDI-Wärmeatlas, *Berechnungsblätter für den Wärmeübergang*, VDI-Verlag, Düsseldorf, 1991.

[10] H. Görtler, *Dimensionsanalyse, Theorie der physikalischen Dimension mit Anwendungen*, Springer-Verlag, Berlin, 1975.

[11] W.J. Duncan, *Physical similarity and dimensional analysis: An elementary Treatise*, Edward Arnold & Co., London, 1953.